2015

A Mechanism for Spatial Orientation Based on Sensory Adaptation in Caenorhabditis Elegans

Johannes Larsch

A MECHANISM FOR SPATIAL ORIENTATION BASED ON SENSORY ADAPTATION IN *CAENORHABDITIS ELEGANS*

A Thesis Presented to the Faculty of

The Rockefeller University

in Partial Fulfillment of the Requirements for

the degree of Doctor of Philosophy

by

Johannes Larsch

June 2015

A MECHANISM FOR SPATIAL ORIENTATION BASED ON SENSORY ADAPTATION IN *CAENORHABDITIS ELEGANS*

Johannes Larsch, Ph.D.

The Rockefeller University 2015

During chemotaxis, animals compute spatial information about odor gradients to make navigational choices for finding or avoiding an odor source. The challenge to the neural circuitry is to interpret and respond to odor concentrations that change over time as animals traverse a gradient. In this thesis, I ask how a nervous system regulates spatial navigation by studying the chemotaxis response of *Caenorhabditis elegans* to diacetyl.

A behavioral analysis demonstrated that AWA sensory neurons drive chemotaxis over several orders of magnitude in odor concentration, providing an entry point for dissecting the mechanistic basis of chemotaxis at the level of neural activity. Precise microfluidic stimulation enabled me to dissociate space from time in the olfactory input to characterize how odor sensing relates to behavior. I systematically measured neuronal responses to odor in the diacetyl chemotaxis circuit, aided by a newly developed imaging system with flexible stimulus delivery and elevated throughput. I found reliable sensory responses to the behaviorally relevant range of odor concentrations. I then followed odor-evoked activity to downstream interneurons that integrate sensory input. Adaptation of neuronal responses to odor yielded a highly sensitive response to small increases in odor concentration at the interneuron level, providing a mechanism for

efficient gradient sensing during klinokinesis. Adaptation dynamics at the sensory level were stimulus-dependent and cell-autonomously altered in several classes of mutant animals.

Behavioral responses to different concentrations of diacetyl resulted from overlapping contributions from multiple sensory neurons. AWA was specifically required for orientation behavior in response to small increases in odor concentration that are encountered in shallow gradients, demonstrating functional specialization amongst sensory neurons for stimulus characteristics. This work sheds light on an algorithm underlying acute behavioral computation and its biological implementation.

The experimental results are presented in two parts:

Chapter 2 describes the development of a microscope for high-throughput imaging of neuronal activity in *Caenorhabditis elegans*. I present a characterization of chemosensory responses to odor and its correlation with behavior. This work has been published (Larsch et al., 2013).

Chapter 3 describes the functional architecture of the AWA chemosensory circuit and the role of adaptation in maintaining sensitivity over a wide range of stimulus intensities. This work is currently being prepared for publication.

This thesis is dedicated to my family

Acknowledgements

I truly wish to thank Cori for her guidance and inspiration throughout my graduate years. Cori has given me incredible freedom to explore and to play, to learn and to think during the adventures of science.

I would like to thank my thesis committee Leslie and Stan and my external committee member Matthieu. Leslie believed in me as an undergraduate visiting student and introduced me to the Rockefeller University. Stan has made me think hard about what aspects of biology I enjoy most to decide what I should work on. Matthieu first introduced me to *C. elegans* chemotaxis during a journal club in Leslie's lab and sparked my interest in animal orientation.

Dirk Albrecht introduced me to the world of microfluidics and it was fantastic to work in such close collaboration to develop wide field imaging and get our paper on the way.

Donovan Ventimiglia is the friend needed to make it through graduate school and to find the right time to get married.

The Bargmann lab is a place of unmatched inspiration to discuss passionately all aspects of science and beyond. It was great learning from all of you!

Thank you for tolerating my weeks of ferocious writing dear family and friends. Hannah and Vincent: I will be with you again now ☺

Table of Contents

List of Figures

Chapter 1 Introduction

Spatial orientation

Spatial orientation is a fundamental problem in biology, because the environment of organisms is rarely uniform. Different regions differ in their value to the organism by providing more nutrients, suitable mating partners, or better shelter from harsh conditions. As a result sophisticated sensory systems have evolved allowing organisms to navigate to favorable conditions. These range from the migration of birds to feeding grounds using the earth's magnetic field to bacterial chemotaxis, by which individual cells swim towards peak levels of nutrients in a gradient.

The robustness of spatial orientation makes it an attractive paradigm to study the neuronal basis of behavior. In this study, we dissect the ability of the nematode *Caenorhabditis elegans* to navigate in a spatial gradient of food-related odors, comprising behavioral strategy, neuronal circuit function, and cellular physiology. These three levels loosely recapitulate the levels of analysis put forth by David Marr as a framework for understanding computation and neural circuitry in the visual system (Marr and Poggio, 1976): to distinguish several 'nearly independent levels of description' that can be summarized as computational, algorithmic and mechanistic (Marr and Poggio, 1976).

The computational level defines the problem to be solved by the system, or, in other words, makes assumptions about the behavioral goal and the available sensory information. In the case of chemotaxis for example, we regard 'find source of attractive odor' as the behaviorally defined computation.

The algorithmic level addresses the circuit level logic that solves the computation and typically, a given computation can be implemented by independent algorithms. For example, conceptually, gradient climbing could be achieved by comparison of two simultaneously sampling sensors or by temporal differentiation of a single sensor to regulate motor activity. (See (Braitenberg, 1986) for a rich description of thought experiments on hypothetical 'vehicles' performing a variety of computations.) It may be useful to consider sub-levels within the algorithmic level to appreciate conceptual hierarchy, by analogy to the levels of computer programming including machine language, assemblers and high level scripting language.

The mechanistic level is concerned with the implementation of a specific algorithm in biological hardware. For example, how is temporal differentiation achieved at the level of molecules or synaptic connections between neurons?

Behavioral strategies for spatial orientation

Categorizing orientation strategies based on the information about the stimulus available to the organism can help to explicitly define the computation involved in a specific behavior, thus constraining how it is implemented at the level of algorithms (Figure 1-1) (Codling et al., 2008; Fraenkel, 1961; Schöne, 1984). Conceptually, two general classes of strategies of orientation are distinguished:

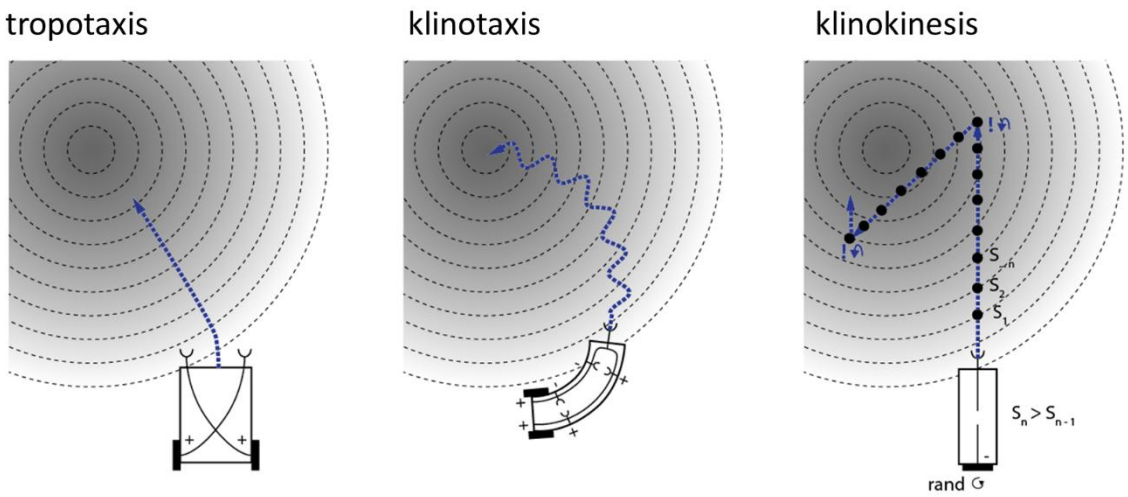

Figure 1-1 **Strategies for spatial orientation.**
During Tropotaxis, two spatially separated sensory organs detect differences in stimulus intensities. During klinotaxis, stimulus sensing at one sensor is coupled to proprioreception to bias motor output. During klinokinesis, stimulus intensity is compared between successive measurements. If attractant levels increase, turning is low. If attractant levels fall, turning is high. Turn orientation is random. Illustration by Hannah Hesse.

Taxis

In direct orientation (**taxis**, from Greek: tassein – “arrange”), the organism detects stimulus direction relative to its own body orientation, allowing deterministic steering. This response is also called directional or oriented. Taxis strategies are subdivided depending on how the organism detects stimulus orientation. Sufficiently large organisms can compare stimulus intensities between spatially separated sensors and orient based in this comparison (tropotaxis from Greek: tropos – “change, turn”). For example, a comparison of the time at which sound arrives at the left versus the right ears is used in vertebrate sound localization (Kandel, 2013). In the alternative strategy of klinotaxis (Greek: klinein – “to bend”), the animal moves its own sensory organs with respect to the stimulus to detect spatial patterns. For example, *Drosophila* larva actively

sweep their head several times before tending to turn towards the side of stronger attractant stimulation (Gomez-Marin and Louis, 2011).

Kinesis

An alternative class of strategies uses indirect orientation (**kinesis**, Greek: “movement”), where the organism samples the stimulus at a single point in space without reference to its own body orientation and uses this measurement to regulate speed (orthokinesis, Greek: orthos – “straight”) or path sinuosity (klinokinesis). Sinuosity is a purely spatial measure to describe the amount of turning associated with a path, regardless of details of movement. Alternatively, if turns are typically sharp and infrequent, researchers use turning frequency to describe the turning events associated with a path. Kinesis can be implemented with absolute or differential stimulus detection (A-kinesis, D-kinesis) meaning that movement is controlled with respect to the absolute stimulus intensity or the change in intensity between steps (Codling et al., 2008). The strategy based on changes in intensity is sometimes called an adaptation-based mechanism.

The terminology used to describe these phenomena is still under refinement and not necessarily pervasive across disciplines. For example, bacterial movement in a chemical gradient has the characteristics of klinokinesis but is typically called chemotaxis (Berg, 2004). We will use the term chemotaxis to refer to any migration towards chemicals, irrespective of the underlying strategy.

The random walk model

A process consisting of successive steps with random orientation can be formalized mathematically as a random walk. Its most basic form is the uncorrelated and unbiased

random walk in which the orientation of each step is random and independent of prior steps; the process has no history. Unbiased random walks exhibit no net drift on a population level. These idealizations are closely met by Brownian motion of microscopic particles and the random walk framework is the basis of most of the theory on diffusive processes (Berg, 1993; Codling et al., 2008).

Random walk models also capture aspects of movement generated by living organisms. One famous example is bacterial chemotaxis which can be interpreted as a correlated biased random walk. It differs in two important characteristics from simple diffusion. First, bacteria (and all other organisms) exhibit a certain level of 'persistence' in their orientation stemming from the fact that biological mechanisms for generating thrust for locomotion typically have a preferred orientation (forwards). This leads to a correlation in orientations during successive time bins. Second, bacteria can bias the frequency of reorientation maneuvers, termed tumbles, in response to external stimuli such as a concentration gradient of a nutritious sugar such that they produce a net drift towards attractants and away from repellents (Berg, 2004).

Change detection can drive kinesis more efficiently than absolute detection

The random walk formalism can be used to assess different orientation strategies for their ability to generate drift in a gradient (Berg, 1993; Codling et al., 2008). Comparisons of absolute and differential kinesis mechanisms show that only differential kinesis can efficiently drive a biased random walk towards stimulus peaks (Benhamou and Bovet, 1989). This becomes intuitively clear by envisioning an organism in a gradient. Using only absolute stimulus levels to control turning, the organism needs to increase turning with increasing stimulus levels in order to spend relatively more time

near the peak than away from the peak. This reduces its diffusivity and thus limits motility by increasing path sinuosity locally. The ‘attraction’ generated by this absolute kinesis is unstable because an organism moving away from the peak will become less and less likely to turn back towards the peak and eventually get lost. If an organism explores a patchy environment, locally reducing mean square diffusion within favorable patches and increasing mean square diffusion between patches is considered an efficient patch use strategy. Therefore, absolute kinesis is sometimes termed a space use mechanism rather than an orientation mechanism.

Using changes in stimulus intensity to control turning for differential kinesis enables the organism to selectively prolong runs in the ‘correct’ orientation i.e. when the change in attractant concentration is positive and or shorten runs in the ‘incorrect’ orientation i.e. when the change in attractant concentration is negative. This will effectively decrease the duration of runs in the incorrect orientation and thus impose directionality on the random walk even though individual turns are randomly oriented. The computational cost of differential kinesis is that it requires constant updating or memory to calculate the difference in stimulus intensities between steps.

Significance of adaptation for the biased random walk

One mechanism to differentiate an input is response adaptation or desensitization. Adaptation converts the initially strong response to a stimulus to a lower steady state level even if the stimulus persists (Figure 1-2). After adaptation diminishes the response, the system may be able to respond to another increase in stimulus intensity. Mechanistically, a response can be transient if stimulation triggers two antagonistic processes that lead to formation and decay of the response with some temporal disparity

(Koshland et al., 1982). Thus, the response exhibits memory because it reports the difference between the intensity of the previous and the current stimulus, rather than absolute stimulus intensity. An adapting cell 'forgets' the stimulus with a time constant determined by the relative rates of formation and decay of the response.

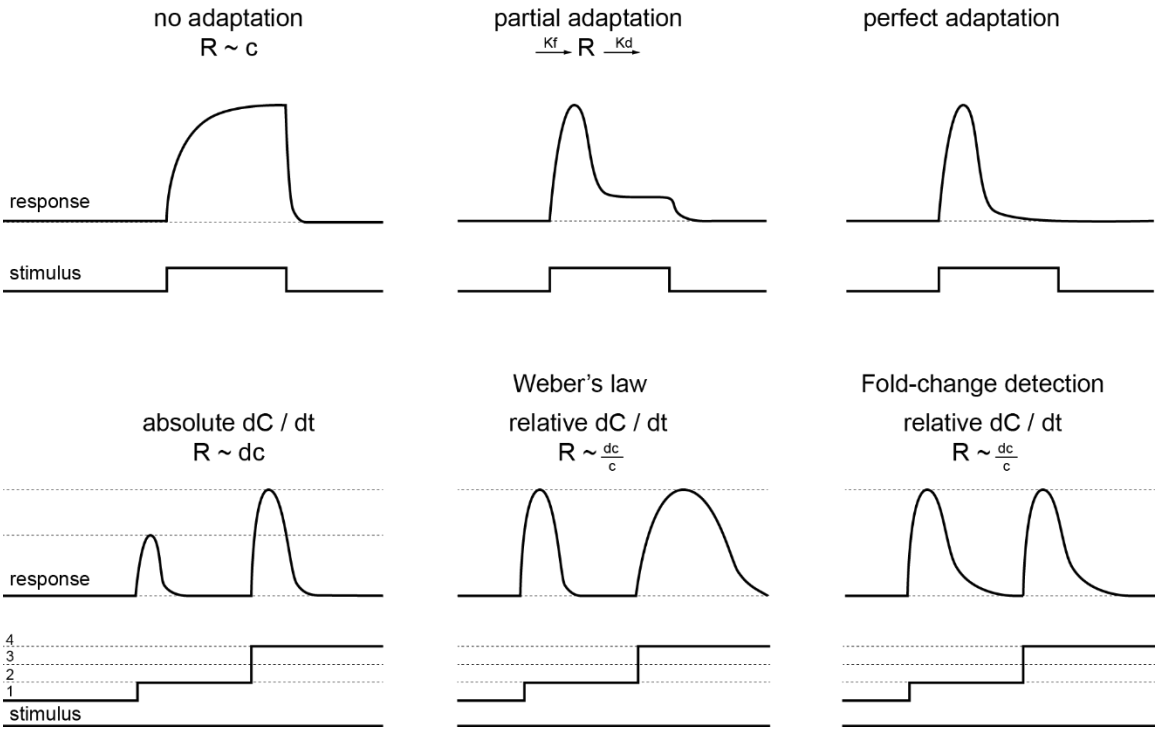

Figure 1-2 **Alternative modes of response adaptation.**
A response without adaptation reaches a steady state proportional to stimulus intensity. Adaptation converts the initially strong response to a lower steady state level. Steady state level and time course of adaptation depend on the relative rates of formation (k_f) and decay (k_d) of the response. During perfect adaptation, the response returns exactly to baseline. An adapting sensory systems can report absolute or relative dC/dt. A system reports relative dC/dt if responses to two identical fold-changes in stimulus intensity (e.g. 1 to 2 and 2 to 4, both 2 x fold change) are similar. Weber's law requires that peak response magnitude be constant for a given fold-change. Fold change detection is met if response dynamics and magnitude are constant. Illustration by Hannah Hesse.

A second benefit of adaptation is that it increases information transmission by increasing the dynamic range of the response around stimulus levels encountered in the recent past (Wark et al., 2007). This property can greatly improve performance of a sensory system that needs to encode a wide range of stimulus intensities with high resolution. Human vision, for example, operates over nine order of magnitude of light intensities ranging from dim moonlight to bright sunlight (Rieke and Rudd, 2009). Similarly, *C. elegans* chemotaxes towards the odor diacetyl over at least seven order of magnitude in odor concentration (Bargmann et al., 1993).

Fold-change detection

There are special cases of adaptation defined by the exact relationship of the response intensity with the stimulus level (Figure 1-2). In perfect or exact adaptation, the response returns to the baseline level at steady state, regardless of stimulus intensity. Exact adaptation is indeed observed across a wide range of sensory modalities and in bacterial chemotaxis. The regulation of turning frequency of single cells in response to attractant stimulation exhibits robust and exact adaptation over several orders of magnitude in attractant concentration (Barkai and Leibler, 1997; Berg, 2004).

A system that adapts and therefore reports changes rather than absolute stimulus intensity may report absolute changes in intensity or relative changes. If two increases in stimulus intensity of the same relative magnitude (i.e. 1 to 2 and 2 to 4, both increase by a factor of 2) cause the same response magnitude including identical response dynamics, the system performs fold-change detection (Goentoro et al., 2009; Shoval et al., 2010) (Figure 1-2). Certain molecular pathways such as stimulation of beta-catenin

responses by Wnt signaling and nuclear entry of MAPK after EGF stimulation exhibit fold-change characteristics (Cohen-Saidon et al., 2009; Goentoro and Kirschner, 2009). Fold-change detection is reminiscent of Weber's law, derived from psychophysical experiments in the visual system, which says that the just noticeable difference between two stimuli is proportional to the magnitude of the stimuli (Weber, 1905). Fold-change detection is defined more strictly than Weber's law, requiring conserved response dynamics across different stimulus levels, whereas Weber's law is satisfied with conserved peak response magnitude (Figure 1-2).

Normalization and adaptation

A normalized response to a stimulus is dependent on the magnitude of the total stimulus intensity, integrating multiple inputs. For example odor responses of individual first layer projection neurons in the antennal lobe of Drosophila melanogaster are normalized by the mean population response in the antennal lobe (Wilson, 2013). Effectively, the contribution of each neuron is scaled by the total number of neurons active at a particular time. Like adaptation, normalization works to keep sensory systems from saturating, expanding their dynamic range.

Network motifs for adaptation

The mechanism of adaptation in the presence of persistent stimulation can be conceptualized as the result of reciprocal interactions within a network consisting of an input, a response and an inhibitor (Ma et al., 2009). Specific interaction rules between these components can produce adaptation and in fact, a comprehensive computational search of all possible interactions showed that only two sets of interactions can achieve exact adaptation independent of stimulation level (Ma et al., 2009). Knowing a priori the

network motif underlying adaptation in a given biological system might inform experiments to reveal the biochemical implementation. A theoretical approach is currently being developed with the aim to infer network topology from experimentally measured responses to systematic stimulation using step pulses of varying pulse length and interpulse interval as inputs (Rahi et al., in preparation). The relationship of pulse length with the interpulse interval yielding maximal mean output might serve as a signature to distinguish between five alternative network topologies that can produce exact or inexact adaptation. This approach has not yet been applied to analyze neuronal network topologies.

Spatial orientation in *Caenorhabditis elegans*

The soil nematode *Caenorhabditis elegans* navigates the environment in response to numerous sensory cues. Animals have a preferred oxygen level, temperature, light, substrate osmolarity and texture, and they migrate towards these levels when allowed to move freely in a gradient (Gray et al., 2004; Mori and Ohshima, 1995; Ward et al., 2008; Zhang, 2008). In addition, animals respond with attraction or repulsion to a large number of chemicals that are thought to signal the presence of food or harmful conditions such as predators or toxins (Bargmann, 2006a). Pheromones can trigger complex physiological and behavioral programs such as the transition into a different developmental 'dauer' stage (Bargmann and Horvitz, 1991a) or regulate aggregation (Macosko et al., 2009). For this work, we will focus on stimuli that trigger robust orientation behavior. Chemicals with high enough vapor pressure to diffuse significantly in air upon evaporation will be called odors, to distinguish them from tastants which dissolve and diffuse predominantly in the liquid phase. Diacetyl (Butane-2,3-dione) is a typical odor with a vapor pressure of 7.5 kPa whereas non-volatile Na^+ and Cl^- ions are

typical tastants. Irrespective of volatility, chemicals must re-dissolve in the liquid phase surrounding *C. elegans* on its substrate in order to interact with odorant receptors.

The small size of *C. elegans* places important constraints on its detection of chemical gradients. 11 pairs of chemosensory amphid sensory neurons detect chemicals via sensory dendrites that project to the tip of the nose to reach two olfactory pores where they contact the environment (Ward et al., 1975). Like most neurons in *C. elegans*, amphid sensory neurons are found as bilateral pairs (left and right) that can be functionally distinct. The two AWC neurons, for example, exhibit asymmetric gene expression and drive behavior to partially overlapping but distinct sets of odors (Wes and Bargmann, 2001). In other neurons such as AWA, no such differentiation between the two sister neurons is known and they are presumed to detect the same chemicals. Two sensory neurons detecting the same stimulus theoretically provide a substrate for bilateral left-right sensing, but *C. elegans* locomotion is inconsistent with this strategy because animals crawl on their sides using dorsoventral body bends and cannot turn effectively along the left-right axis. Their posture aligns the left and right olfactory pores over the plane defined by the substrate and hence, animals can effectively only sample odor concentrations at one point in space at a time (Ward et al., 1975).

Chemotaxis strategies in *Caenorhabditis elegans*

Forward runs and turns alternate during locomotion

Analysis of *C. elegans* locomotion in gradients of tastants, temperature and odors has provided evidence for both taxis and kinesis strategies during spatial orientation. Generally, animals generate forward thrust on planar substrates by undulatory movement (Wallace, 1968). On homogeneous substrates such as agar plates, animals

spend most of their time in relatively straight (<50 deg/sec) forward motion that is occasionally interrupted by sudden changes in direction, termed turns (> 50 deg/sec) (Pierce-Shimomura et al., 1999). Two stereotyped turning patterns are typically distinguished. (1) A reversal followed by forward motion in a different direction. (2) A reversal followed by a sharp turn in which the animals head touches its tail, resembling the greek letter Omega, followed by forward motion, typically with a large change in direction (omega turn).

Animals removed from food exhibit a biphasic regulation of basal turning rates. The rate of turns is high for about 20 minutes, followed by a reduction in turning and long runs thereafter. This behavior results in low mean square diffusion during the first phase (termed local search) and dispersal in the second phase (Gray et al., 2005). The modulation of turns under these conditions is interpreted as a component of local exploitation vs. exploration strategy independent of orientation towards a specific stimulus.

Chemotaxis can be assessed on agar plates

A convenient and widely adopted way to assess chemotaxis in *C. elegans* is on flat agar plates. A chemical gradient is formed by spotting a chemical onto the plate and allowing it to diffuse in agar or air before placing about one hundred animals at some distance from the chemical. The migration towards or away from the chemical may be quantified after a defined amount of time, e.g. one hour. Alternatively, the entire experiment is recorded for subsequent analysis of individual animal paths.

Evidence for klinokinesis

The first demonstration that *C. elegans* regulates the rate of turning in response to chemical stimulation came from tethered animals where imposed decreases in attractant concentration increased the rate of turning (Dusenbery, 1980). Consistent with this observation, freely moving animals in a concentration gradient modulate the rate of turning, or, reciprocally, run length as a function of the change in concentration (dC/dt) (Iino and Yoshida, 2009; Pierce-Shimomura et al., 1999; Tsunozaki et al., 2008). Animals going up a gradient of an attractive chemical perform fewer turns than animals going down the gradient; In other words, the probability of turning is inversely correlated with dC/dt. The angle of each turn is, to a first approximation, random. Therefore, turns contribute to chemotaxis largely by randomizing bearing angle after animals experience a drop in attractants, resulting in a biased random walk towards higher attractant concentration. Computational modeling of this klinokinesis strategy with experimentally derived parameters was sufficient to generate chemotaxis behavior but the efficiency was less than that of wild type animals (Iino and Yoshida, 2009; Pierce-Shimomura et al., 1999). Further analysis revealed that post-turn bearing angles had a weak bias towards the peak of the gradient, a feature that improved chemotaxis performance in the model (Pierce-Shimomura et al., 1999).

Evidence for klinotaxis

In addition to klinokinesis, *C. elegans* uses a klinotaxis strategy of deterministic steering. In smooth gradients, animals on paths orthogonal to the gradient tend to curve gradually into the gradient (Iino and Yoshida, 2009; Luo et al., 2014) and on the edges of sharp

odor gradients, animals exhibit ‘surf turns’ steering into the odor with high probability (Albrecht and Bargmann, 2011).

Klinotaxis and klinokinesis appear to act in parallel in *C. elegans* (Iino and Yoshida, 2009; Luo et al., 2014). While both strategies are generally sufficient to drive chemotaxis in a computer simulation, it was argued that only the combined strategy recapitulates the efficiency of wild type animals and each strategy might be specialized for specific environments (Appleby, 2013; Iino and Yoshida, 2009).

Neural substrates for spatial orientation

The stereotyped arrangement of neurons and their wiring in *C. elegans* neurons has greatly facilitated the repeatable manipulation of identified neurons to study their contribution to behavior. Micro-surgery using a laserbeam made it possible to kill specific neurons in individual animals before testing their behavior in a chemotaxis experiment (Bargmann and Horvitz, 1991b; Fang-Yen et al., 2012). This paradigm revealed specific requirements for defined classes of neurons during chemotaxis.

Chemosensory neurons

Chemosensory neurons are directly regulated via interaction of receptor molecules with their external ligands. The *C. elegans* genome encodes over 1000 odorant receptors, and each olfactory sensory neuron expresses many receptors (Bargmann, 2006a; Brear et al., 2014; Taniguchi et al., 2014), but specific odor-receptor interactions have been demonstrated in only a few cases.

Different classes of chemosensory neurons have distinct ciliated structures at the distal tip of their dendrites, presumably specializations to improve stimulus detection. Cilia are thought to be the site of primary sensory transduction because signaling molecules such as olfactory receptors, G-proteins and transduction channels localize to this compartment (Brear et al., 2014; Tobin et al., 2002). Sensory cilia in *C. elegans* vary greatly in shape between individual classes of sensory neurons ranging from simple pointed endings in ASH to flattened sheet-like or highly branched structures in AWA (Doroquez et al., 2014) but the functional consequences of different cilium structures are not known. While cilium structure is generally stereotypic for each class of sensory neurons, morphological remodeling can occur at least in some cilia in response to environmental cues. For example, reduced sensory signaling in AWB sensory neurons causes remodeling of their cilia membrane structures (Mukhopadhyay et al., 2008).

Chemotaxis to specific chemicals requires identified sensory neurons

Laser ablations revealed that chemotaxis towards many chemicals strictly requires stimulus-specific types of sensory neurons (Figure 1-3). For example, ablation of AWA sensory neurons abolishes chemotaxis to a subset of volatile odors such as diacetyl and pyrazine whereas ablation of AWC sensory neurons abolishes chemotaxis to isoamyl alcohol, butanone and benzaldehyde. ASE sensory neurons are required for NaCl chemotaxis and are therefore considered gustatory neurons (Bargmann and Horvitz, 1991b; Bargmann et al., 1993). AWA mediated chemotaxis to diacetyl depends entirely on the odorant receptor ODR-10 (Sengupta et al., 1996). The requirement of AWA and ODR-10 for diacetyl chemotaxis is limited to low diacetyl concentrations. At higher concentrations AWA ablated animals still localize the odor. Double ablations revealed that AWC sensory neurons compensate for the loss of AWA and drive chemotaxis

behavior to high concentrations of diacetyl (Bargmann et al., 1993; Chou et al., 2001). Together, these results suggest that the sensory representation of specific chemicals at some concentrations may be driven by a single pair of sensory neurons, potentially simplifying the analysis of processing by the downstream circuit.

Sensory neuron identity predicts the sign of the chemotaxis response

C. elegans is attracted to a large panel of chemicals representing a diverse structural space and is repelled by a smaller number of chemicals (Bargmann and Horvitz, 1991b; Ward, 1973). Laser ablation revealed that avoidance or negative chemotaxis is mediated by a dedicated set of sensory neurons, AWB, ASH and ADL (Bargmann et al., 1993). It is the identity of the sensory neuron expressing a specific receptor that determines whether a given chemical binding to that receptor acts as an attractant or repellent. For example, wild type attraction to diacetyl can be re-programmed into avoidance by ectopic expression of the diacetyl receptor ODR-10 in AWB in animals that lack ODR-10 in AWA where it is normally expressed (Troemel et al., 1997). These results suggest that behavioral specificity to different stimuli arises from properties that are inherent to the sensory neuron and that activation of a single type of sensory neuron is sufficient to drive chemotaxis behavior.

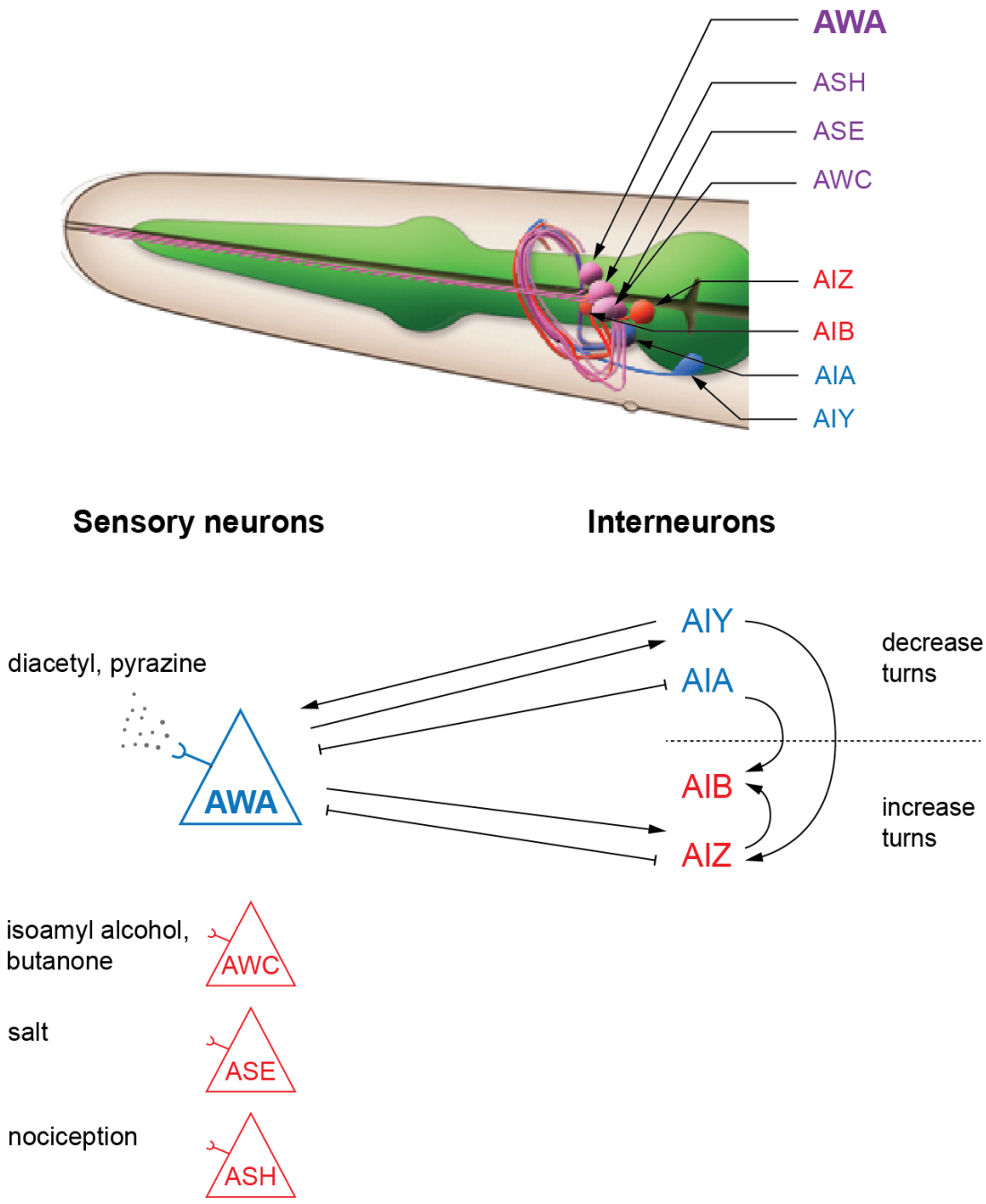

Figure 1-3 **Neurons involved in chemotaxis.**
(Top) schematic of the anterior end of *C. elegans* indicating the approximate location of four sensory neurons and four interneurons. Axonal processes make specific synaptic and gap junction contacts with each other in the nerve ring that wraps around the pharynx (green). Sensory neurons project a dendrite towards the tip of the nose animal. (Bottom) Sensory neurons are drawn with representative ligands. Selected synaptic contacts (→) and gap junctions (⊢⊣) of AWA to interneurons are shown. Neurons labeled in blue/red decrease/increase turning behavior when activated, respectively. Illustration by Hannah Hesse, adapted from www.wormatlas.com.

Sensory transduction in chemosensory neurons

C. elegans chemosensory neurons fall into two groups based on their primary signal transduction channel that converts ligand binding to a change in the membrane potential. Odor signaling in both groups begins in the sensory cilia with odor binding to G-protein coupled receptors and G-protein activation (Bargmann, 2006a). In one group, including AWA and ASH this signal converges onto transient receptor potential (TRP) channels. Animals lacking the main TRPV channel proteins OSM-9 and OCR-2 lose behaviors driven by cells that use this mode of transduction (Tobin et al., 2002). The biochemical steps linking G-protein activation to the opening of TRP channels include a requirement for of polyunsaturated fatty acids (PUFA) (Kahn-Kirby et al., 2004) but the regulation of PUFAs and their role in channel gating are currently unclear.

In the other group, including AWC and AWB sensory neurons, G-protein activation regulates levels of cyclic GMP that opens cyclic nucleotide gated (CNG) channels. A variety of guanylate cyclases (GC) and phosphodiesterases (PDE) are expressed in cyclic GMP sensitive neurons. It is not known which of these enzymes are directly regulated by G-proteins. The major necessary CNG channel proteins are TAX-2 and TAX-4 (Bargmann, 2006a). Interestingly, AWC also expresses the TRP channel subunit OSM-9 but in this neuron it regulates behavioral adaptation of the chemotaxis response after long term exposure with certain odors rather than primary sensory transduction (Colbert and Bargmann, 1995).

Internal state can modify behavioral preference

The chemotaxis response to some chemicals can be modified by experience, a process that may involve associative learning. For example, AWC_ON neurons normally drive

attraction to the odor butanone. This response can be modified by prior exposure to butanone. Exposure to butanone for 1 hour in the presence of food increases attraction to butanone (Torayama et al., 2007). Exposure to butanone for 2 hours in the absence of food inverts the behavior into repulsion, and certain mutations in AWC_ON signaling molecules can cause this behavior even in naïve animals (Tsunozaki et al., 2008).

Similarly, animals starved in the presence of 50 mM NaCl revert their naïve ASE mediated attraction to 50 mM NaCl into avoidance and this avoidance can be induced by enforced translocation of an insulin receptor within ASE sensory neurons (Ohno et al., 2014). Furthermore, salt chemotaxis is directed towards a setpoint concentration associated with the presence of food, such that animals grown at 50 mM NaCl migrate up the gradient when placed at 25 mM and down the gradient when placed at 75 mM (Luo et al., 2014; Saeki et al., 2001).

These examples demonstrate a high degree of plasticity in the chemotaxis response and suggest that the behavioral valence of certain stimuli can be regulated within the sensory network.

Interneurons

Chemosensory neurons in *C. elegans* form chemical and electrical synapses onto interneurons that are sometimes referred to as ‘first layer interneurons’ (White et al., 1986). For AWA, these include AIA, AIB, AIY and AIZ interneurons (Figure 1-3). Systematic laser ablation and subsequent analysis of locomotion patterns has revealed roles for these interneurons in the regulation of turning frequency in isotropic environments (Gray et al., 2005; Tsalik and Hobert, 2003) and numerous studies have extended these results using laser ablations or genetic ablations and optogenetic

silencing in the context of chemotaxis, thermotaxis, mechanosensation and spontaneous locomotion (Iino and Yoshida, 2009; Piggott et al., 2011; Shinkai et al., 2011; Shtonda and Avery, 2006; Yoshida et al., 2012). Generally, higher activity in AIA and AIY interneurons suppresses turning whereas loss of function in these neurons increases turning and the reverse is observed for AIB and AIZ interneurons (Figure 1-3). This has led to the hypothesis that sensory neurons drive chemotaxis behavior by dynamically modulating interneuron activity. This hypothesis was tested most extensively for ASE mediated salt chemotaxis. A complex picture emerges suggesting that of AIA, AIB, AIY and AIZ interneurons, no individual interneuron is strictly required for chemotaxis but they can be differentially required for klinotaxis vs. klinokinesis. For example AIB interneuron ablation causes a lower turning frequency and thus reduces the efficiency of the klinokinesis component of salt chemotaxis while leaving the klinotaxis component intact (Iino and Yoshida, 2009; Luo et al., 2014).

One promising candidate interneuron that might control klinotaxis is the RIA interneuron. Compartmentalized activity in RIA represents both odor information and information about the bending angle of the animal's neck, which is regulated from SMD motor neurons and odor information (Hendricks et al., 2012). This combination could serve as a neural substrate for gradual steering in a gradient: As the animal moves orthogonally to the gradient, the self-generated undulations of the head could lead to detectable differences in odor concentration at different phases of the undulation cycle. However, no direct evidence for this mechanisms currently exists. RIA or another neuron with similar properties might increase the amplitude of bends when they coincide with the detection of an increase in odor concentration, thus steering animals towards the peak. Further research is needed for a better understanding of the acute contribution of individual interneurons during chemotaxis.

Neural activity in the chemotaxis circuit

Calcium as a readout for neuronal activity

With the development of genetically encoded calcium indicators (GECI), measurements of intracellular calcium have become a convenient readout of neural activity in *C. elegans* and other animals. Intracellular calcium is usually low in neurons at rest. Elevated calcium correlates with neural activation and drives synaptic transmission by promoting synaptic vesicle fusion. Calcium transients in *C. elegans* chemosensory neurons are initiated from G-protein coupled receptor signaling converging either on CNG cation channels or TRPV channels (Bargmann, 2006a), both of which are somewhat calcium permeable. The transduction current generated by these events is amplified by voltage gated calcium channels (VGCC) and second messenger cascades that promote calcium release from intracellular stores and the extracellular lumen. Most neurons in *C. elegans* display graded membrane potentials rather than spiking action potentials. The lack of spikes correlates with the evolutionary loss of voltage activated Na channels in the *C. elegans* genome. Interpreting elevated calcium as a direct proxy for neural activation is useful, but likely an oversimplification, because neuronal calcium dynamics in the cell body do not always correlate with neuronal depolarization and synaptic signaling (Komuniecki et al., 2014). For example, RIA interneuron calcium levels are anticorrelated in two regions of the RIA axon and calcium transients in AIA and AIY interneurons are mostly confined to the neurite (Chalasani et al., 2007; Larsch et al., 2013). Furthermore, calcium has been implicated in feedback mechanisms that generally dampen the cellular responses (Kato et al., 2014; Kuhara et al., 2002). Whole cell calcium levels may therefore be a read-out of multiple processes including neuronal activation.

Calcium imaging in sensory neurons reveals ON cells and OFF cells

Laser ablations and genetic analysis have mapped specific stimuli to most sensory neurons in *C. elegans*. With the advent of calcium imaging, it became possible to study the nature of this mapping at the level of neural activity. Recordings of stimulus-evoked calcium transients exist for many *C. elegans* sensory neurons. The majority of these recordings were obtained from glued or trapped animals treated with step increases in stimulus intensity.

Chemosensory neurons fall into two groups based on the direction of their stimulus-evoked calcium responses. In some neurons, such as AWA, ASH and ASEL, calcium levels rise with increased ligand concentration. In other neurons, such as ASER and AWC, calcium levels fall below resting levels upon stimulation and rise after stimulus removal (Chalasani et al., 2007; Fukuto et al., 2004; Shinkai et al., 2011; Suzuki et al., 2008). These latter neurons are thought to have significant basal transmitter release that is suppressed upon stimulation. The molecular determinant of the response polarity is presumably embedded in the sensory transduction machinery.

The diversification of sensory neurons into ON and OFF cells is reminiscent of the segregation of processing pathways in the vertebrate visual system at the level of bipolar and retinal ganglion cells (Kandel, 2013) and in laminar cells of the *Drosophila* eye (Joesch et al., 2010). In the salt sensing ASE neurons this segregation emerges between the two sister neurons: ASER calcium levels decrease with upshifts in salt concentration and increase with downshifts whereas ASEL calcium increases with upshifts and is insensitive to downshifts (Suzuki et al., 2008). The asymmetric responses could together provide a substrate for behavioral responses that are similarly sensitive to

upshifts and downshifts, although ASER is essential and ASEL is dispensable for salt chemotaxis under most conditions (Luo et al., 2014), and several chemicals trigger chemotaxis with high fidelity even though they are only represented by one response polarity at the sensory level. Therefore, the functional significance of ON and OFF response polarities remains an open question.

Calcium imaging in Interneurons

Many first layer interneurons exhibit stimulus evoked calcium transients, often superimposed on fluctuations in calcium levels that are not related to the stimulus. For example, AIA and AIY interneurons increase calcium concentration in response to step pulses with attractive odors isoamyl alcohol or diacetyl (Chalasani et al., 2007, 2010; Larsch et al., 2013) suggesting that both neurons receive input from both AWC and AWA. The response polarity of the two sensory neurons is opposite, but they elicit the same polarity response in the interneurons. Therefore, AIA and AIY interneurons must differentially interpret signals from AWC versus AWA. Glutamate signaling from AWC onto inhibitory GLC-3 glutamate receptors in AIA is thought to suppress AIA activity at rest; this suppression is released upon odor stimulation when AWC calcium falls (Chalasani et al., 2010). The wiring diagram indicates a gap junction between AIA and AWA, which is likely a sign preserving connection between these two neurons.

Calcium imaging in freely moving animals

While immobilized animals offer practical advantages for calcium imaging, it is not always possible in this configuration to recapitulate the sensory experience of a freely moving animal to study neural responses to behaviorally relevant stimuli. Furthermore, interneurons reflect not only sensory input but also internal states and proprioceptive

feedback that are likely to be affected by restraint. Calcium recordings from sensory neurons in freely moving animals have largely matched those obtained from immobilized animals (Clark et al., 2006; Larsch et al., 2013; Luo et al., 2014), confirming the notion that sensory neurons can faithfully reflect sensory information, irrespective of the internal state of the animal. Several cases of interneuron imaging on the other hand have revealed extensive correlations of calcium responses with animal movements and behavioral state transitions. For example, high AIB and AVA calcium levels generally correlate with reversal behavior whereas AIY calcium levels fall upon initiation of reversals (Luo et al., 2014; Piggott et al., 2011). Transitions from dwelling to roaming states correlate with low calcium levels in NSM and high calcium levels in AIY (Flavell et al., 2013).

Variability in behavior and neuronal responses

Behavioral responses to sensory stimulation can be variable, even if conditions are precisely controlled. For example, behavioral analysis of *C. elegans* exposed to chemical stimulation in microfluidic devices showed that individual animals could respond by generating a pirouette, a reversal or no behavior at all (Albrecht and Bargmann, 2011). We have recently extended this analysis to show that under similar conditions, sensory responses faithfully reflect stimulation, independent of the behavioral response elicited by each stimulus (Larsch et al., 2013). Motor command neuron activity on the other hand correlates closely with behavior (Chronis et al., 2007; Larsch et al., 2013; Luo et al., 2014; Piggott et al., 2011). It is therefore likely that variability arises in the layers of interneurons between sensory input and motor command output, which in the case of *C. elegans* can be on the order of one to five synapses (Varshney et al., 2011). Consequently, it is of interest to improve imaging techniques to record large

samples of neural activity from many animals under precisely controlled conditions to understand how flexible behaviors arise from a stereotyped circuit such as the *C. elegans* nervous system.

Chapter 2 has been published in the journal PNAS (Larsch et al., 2013)

HIGH THROUGHPUT IMAGING OF NEURONAL ACTIVITY IN CAENORHABDITIS ELEGANS

Author contributions:

Johannes Larsch, Donovan Ventimiglia, Cori Bargmann, Dirk Albrecht

The work described in this paper was the result of a close collaboration with Dirk Albrecht who was a PostDoc in the lab and had developed large microfluidic devices for high content behavioral analysis (Albrecht and Bargmann, 2011). The collaboration started after I showed in pilot experiments using these microfluidic devices that AWA GCaMP signals can be recorded in freely moving animals at low magnification.

I initiated and performed experiments involving the odor diacetyl and AWA and AIA neurons and the drug nemadipineA on suggestion of Yifan Xu (data in Figure 2-1, Figure 2-4, Figure 2-5, Figure 2-6, Figure 2-7, Figure 2-8, Figure 2-11, Figure 2-12e,h, Figure 2-3) except for the chemical screen which was driven by DRA (Figure 2-9). I initiated the use of tetramizole to paralyze groups of animals for simultaneous imaging and generated strains with high GCaMP expression in AWA, AWC and AIA. DRA and I jointly wrote analysis scripts for neuronal tracking and data analysis.

DRA initiated and performed experiments involving neurons other than AWA and wrote scripts for behavioral analysis and the characterization of the optical properties of the system (Figure 2-4, Figure 2-12, Figure 2-13, Figure 2-5, Figure 2-6, Figure 2-10)

DRA designed and fabricated miniaturized PDMS devices and devised multi-odor stimulation via multi-channel valves and electronics for pulsed illumination. CIB and DRA supervised data analysis, experimental design and preparation of the manuscript.

DV performed and analyzed gradient experiments (Figure 2-13).

Chapter 2 High throughput imaging of neuronal activity in *Caenorhabditis elegans*

Summary

Neuronal responses to sensory inputs can vary based on genotype, development, experience, or stochastic factors. Existing neuronal recording techniques examine a single animal at a time, limiting understanding of the variability and range of potential responses. To scale up neuronal recordings, we here describe a system for simultaneous wide-field imaging of neuronal calcium activity from at least 20 *Caenorhabditis elegans* animals under precise microfluidic chemical stimulation. This increased experimental throughput was used to perform a systematic characterization of chemosensory neuron responses to multiple odors, odor concentrations, and temporal patterns, as well as responses to pharmacological manipulation. The system allowed recordings from sensory neurons and interneurons in freely moving animals, whose neuronal responses could be correlated with behavior. Wide-field imaging provides a tool for comprehensive circuit analysis with elevated throughput in *C. elegans*.

Introduction

Modern neuronal recording techniques are labor- and equipment-intensive, and generally designed to obtain maximal information from individual animals. However, individuals differ from one another. To understand the full range and variability of neuronal responses, it is desirable to apply high-throughput methods and systematic data collection to many animals under controlled stimulation conditions.

The nematode *C. elegans* is particularly amenable to high-throughput studies of neural and behavioral activity, which are facilitated by its small size, compact nervous system, ease of genetic modification, well-defined behavioral repertoire, and transparent body with optical access to single defined neurons. Optical neural recordings in *C. elegans* have primarily used high-magnification imaging of neurons expressing a genetically-encoded calcium indicator such as GCaMP or cameleon. Glued preparations (Faumont and Lockery, 2006) or partial-body traps (Chronis et al., 2007; McCormick et al., 2011; Wen et al., 2012) enable imaging of calcium dynamics in head neurons, but immobilization limits the animal's behavioral repertoire. More complex behaviors can be visualized in freely-moving animals on agar surfaces by using a moving stage or objective and computer-controlled feedback to track a moving animal and keep a specific neuron in view (Ben Arous et al., 2010; Faumont et al., 2011; Piggott et al., 2011; Zheng et al., 2012). These methods monitor a single animal at a time, as do optical and electrophysiological recording methods in flies, fish, and rodents, which rely upon complex surgeries, implanted sensors, and dedicated equipment for each animal (Ahrens et al., 2012; Dombeck et al., 2007; Ghosh et al., 2011; Maimon et al., 2010; Wilson and McNaughton, 1993).

Here we describe a strategy for recording neuronal activity evoked by precise chemical stimulation of freely-moving or anaesthetized *C. elegans* using wide-field microscopy. We adapted previous microfluidic arenas optimized for normal *C. elegans* crawling behavior and repeatable spatiotemporal stimulation (Albrecht and Bargmann, 2011) to simultaneous optical recording of calcium transients in individual neurons. The automated microscope is capable of continuous recording from over 20 animals at once for hours during repeated stimulation without user interaction. We demonstrate the performance of this method by systematically surveying neural responses to stimulation parameters, testing pharmacological modulators of neural dynamics, and correlating stimulus-evoked locomotory behaviors with calcium dynamics in several chemosensory neurons and interneurons. Our results demonstrate broad capabilities of wide-field microscopy for neural imaging.

Results

Fluorescence imaging at low magnification

Wide-field microscopy eases the challenge of neuron registration and focus in moving samples including live animals. As objective magnification (M) is reduced, the total volume from which light is projected onto the camera expands greatly, with the area field-of-view scaling by 1/M2 and axial depth-of-field by ~1/M. Fluorescent signals can be recorded from any neuron within this volume without stage tracking or focusing, as long as individual neurons can be resolved, motion blur is minimized, and signals exceed background noise. We met these requirements for calcium imaging of *C. elegans* neurons on a standard inverted epifluorescence microscope using high numerical aperture (NA) objectives (2.5x/0.12 NA or 5x/0.25 NA) and a sensitive low-noise electron-multiplying charged coupled device (EM-CCD) camera to maximize the signal-to-noise of fluorescence recordings, and fast-switching solid-state illumination to minimize motion artifacts and phototoxicity (Figure 2-1A).

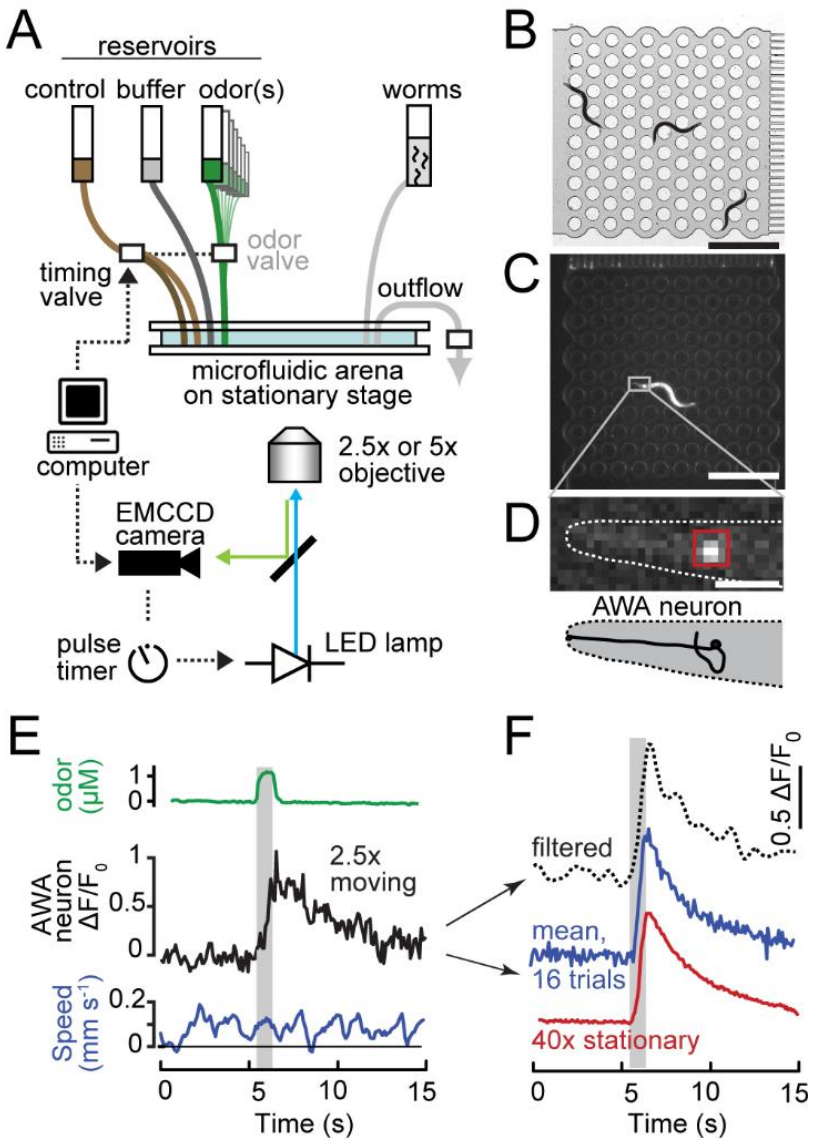

Figure 2-1 **Wide-field imaging of neural activity with microfluidic stimulation.** (**A**) Schematic of the automated microscope. Video acquisition and fluidic valves for chemical stimulation are computer-controlled; fluorescence illumination is pulsed via digital signals synchronized with each camera frame. No motorized stage or focus mechanisms are needed with low-magnification objectives and glass-mounted microfluidic arenas. (**B**) Brightfield image of the microfluidic arena containing three animals and dye to distinguish fluidic channels (gray) from microposts. Scale bar, 1mm. (**C**) Full-frame camera image showing one adult animal expressing GCaMP2.2b in the AWA sensory neurons. Scale bar, 1 mm. (**D**) Magnified view of the head from panel **c**. Red box indicates the integration window. Scale bar, 50 µm. (**E**) AWA sensory neuron response (relative fluorescence, $\Delta F/F_0$) and speed of a moving animal responding to a 1-s pulse of 1 µM diacetyl odor (DA). (**F**) Comparison of the single fluorescence trace at 2.5x from panel **e**, filtered to quantify individual response magnitude and dynamics, the mean of 16 repeated stimulations of the same moving animal, and a single recording in a stationary animal at 40x magnification.

A microfluidic arena for *C. elegans* behavioral analysis (Albrecht and Bargmann, 2011) was miniaturized to keep animals within the 3.28 x 3.28 mm2 field-of-view and ~50 µm depth-of-field at 2.5x magnification while delivering precise patterns of chemical stimulation. The fluidic design contained a structured micropost array for unimpeded crawling locomotion, barriers to prevent animal escape, and inlet channels tailored to present temporal pulses, spatial stripes, or linear gradients of liquid-borne stimuli (Albrecht and Bargmann, 2011) (Figure 2-1B and Figure 2-2). The microscope automatically controlled chemical stimulation via fluidic valves, selecting the concentration and timing parameters according to a programmed pattern (Figure 2-1A). A software suite, called NeuroTracker, tracked multiple animals as they traversed the arena, integrated fluorescent signals, corrected for background and illumination, and automatically detected behavioral responses, as described in the Supplementary Note.

The duration of optical neural recordings is typically limited by phototoxicity and photobleaching that reduce signal fidelity over time. Phototoxic damage in *C. elegans* is evident after 20 min of cumulative blue-light illumination by increased autofluorescence in many tissues (Clokey and Jacobson, 1986; Coburn et al., 2013). In contrast, pulsed illumination (10 ms per 100 ms frame) did not cause photodamage over at least 2 hours (Figure 2-3). Short illumination pulses also prevented motion blur in animals moving at up to 2 mm s−1, ten-fold greater than mean crawling speed (Figure 2-4).

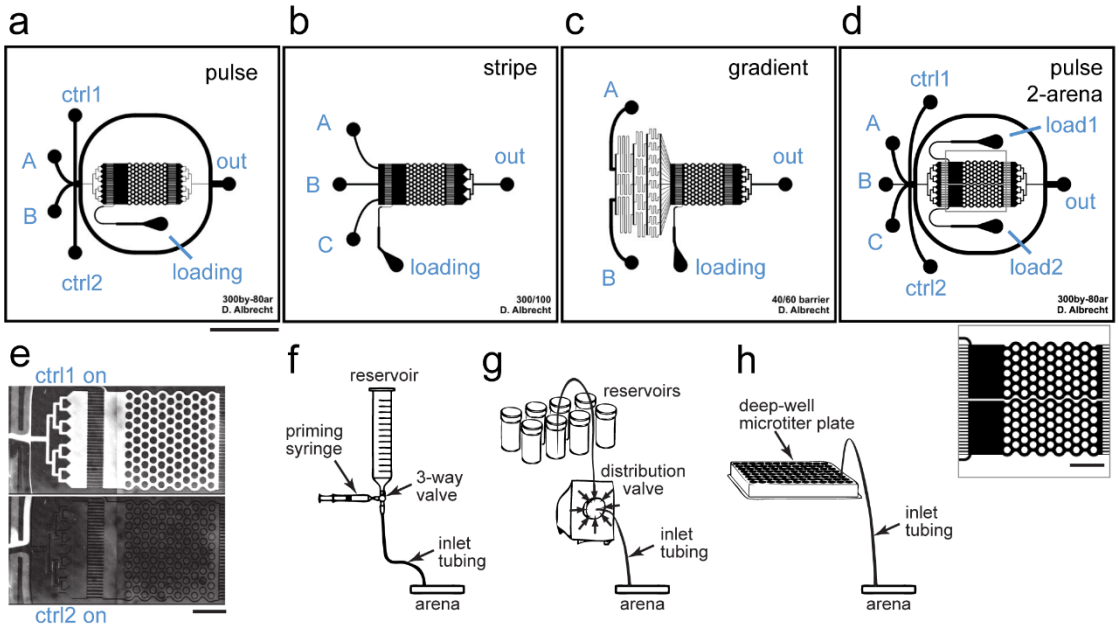

Figure 2-2 **Microfluidic device patterns and external fluidic connections.** (**a-d**) Microfluidic device designs. Black lines indicate fluidic channels. *A*, *B, C*, stimulus inlets; *loading*, animal loading inlet; *out*, outflow port; *ctrl1 & ctrl2*, control fluid inlets. Scale bar, 5 mm. Devices deliver a temporal pulse (**a**), spatial stripe (**b**), or linear gradient (**c**) to one or two independent animal populations (**d**). Magnified panel below (**d**) shows horizontal division separating the top and bottom arenas. Scale bar, 1 mm. (**e**) Operation of pulse device via shifting streams. With *ctrl1* open and *ctrl2* closed, stream A (bright) passes through the arena whereas B (dark) flows around the arena to outflow (top). With *ctrl2* open and *ctrl1* closed, B flows through arena (bottom). Scale bar, 1 mm. (**f-h**) Stimuli are delivered from a syringe reservoir (priming syringe aids in removing air bubbles) (**f**), via 8-position distribution valve (**g**), or by transfer of inlet tubing to multiwell plates (**h**).

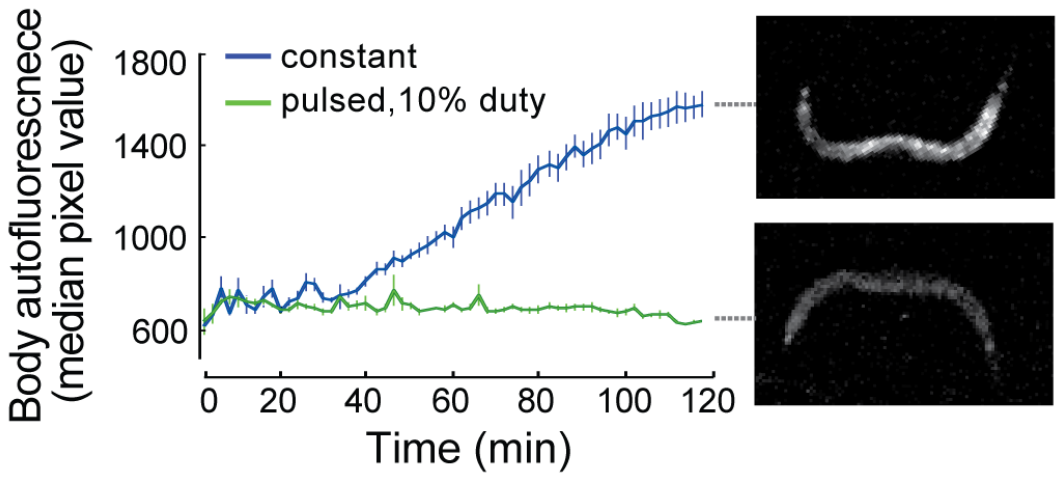

Figure 2-3 **Pulsed illumination prevents phototoxicity.**
Autofluorescence over 2 hrs during constant blue light (450−490 nm) exposure or pulsed exposure at 10 ms pulses every 100 ms. Exposure was one minute every two minutes for both modes. Autofluorescence was calculated as median intensity of brightest 2% of pixels from 40x40 pixels surrounding the neuron, excluding 9x9 pixels containing the neuron. Mean ± s.e.m., n=9 animals for constant exposure, n=6 animals for pulsed exposure. Representative frames are shown at 120 min.

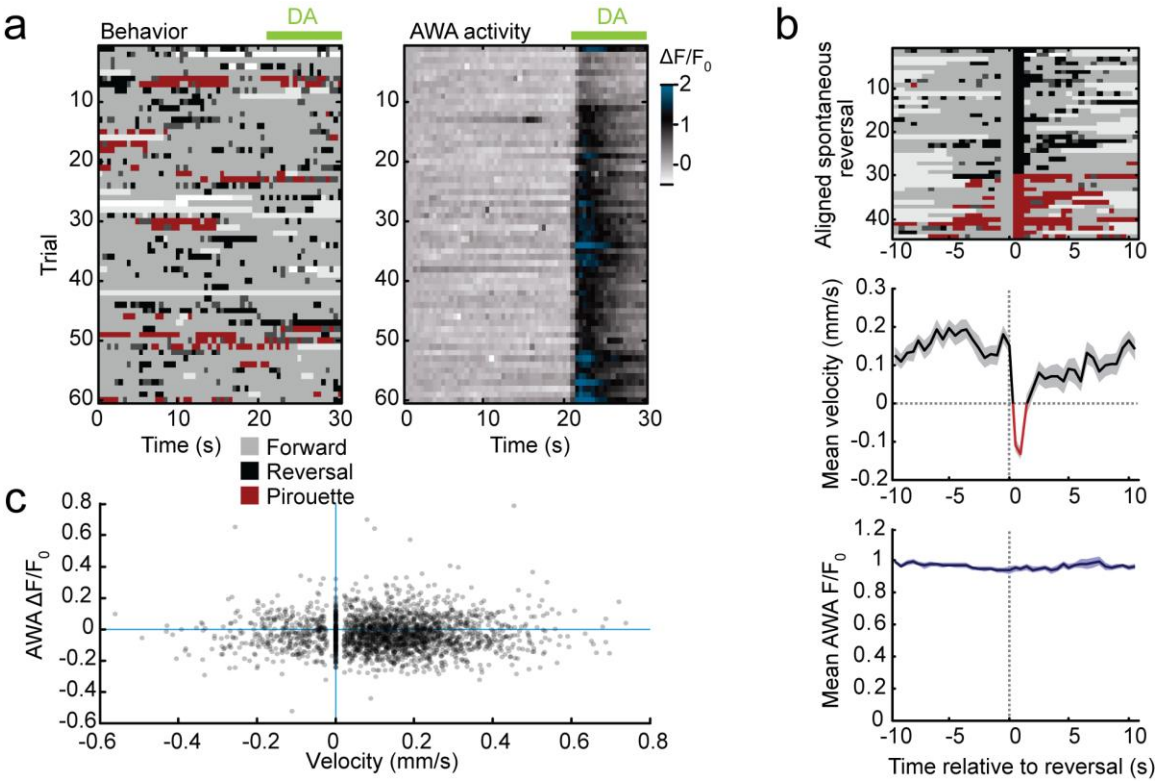

Figure 2-4 **Pulsed illumination and large depth-of-focus prevent motion artifacts.** (**a**) Ethogram of behavior during 20 s buffer presentation followed by 10 s diacetyl odor presentation, recorded with 10 ms pulsed illumination (left), and corresponding heatmap of AWA activity (right). AWA activity was low during spontaneous reversal and pirouette behaviors in buffer and rose in odor. (**b**) Ethogram of spontaneous reversals in buffer, short (black) and long pirouette (dark red), aligned to reversal onset (top). Corresponding mean velocity (center) and mean AWA fluorescence (n=44 reversals) showed reverse movement but no effect on neural fluorescence. (**c**) Scatter plot of instantaneous velocity vs. AWA fluorescence during 20 s buffer presentation from panel **a**. No correlation was observed; negative correlation would have suggested motion blur.

We expressed the genetically-encoded calcium sensor GCaMP2.2b in the two AWA sensory neurons, which respond to the attractive odor diacetyl with an increase in intracellular calcium indicative of depolarization (Bargmann et al., 1993; Shinkai et al., 2011). At 2.5x magnification, AWA neuron morphology could not be resolved due to spatial undersampling (6.4 µm/pixel, compared to an AWA cell body diameter of 3−5 µm), so a larger region of interest of standard size was used for analysis (Figure 2-1C,D and Figure 2-5). In response to a 1s pulse of diacetyl (10-7 dilution; 1.15 µM), we

detected a rapid increase and then a gradual decline in the integrated fluorescence signal (Figure 2-1E) that closely resembled standard high-magnification recordings of AWA GCaMP responses (Figure 2-1F). The fluorescence signal-to-noise ratio was proportional to objective magnification but remained above ~10 at 2.5x (Figure 2-1F and Figure 2-6), a value sufficient for quantification of response magnitude and dynamics from temporally-filtered single traces or averaged repeated trials. Thus, wide-field imaging at reduced resolution permits accurate measurement of GCaMP signal dynamics in individual *C. elegans* neurons.

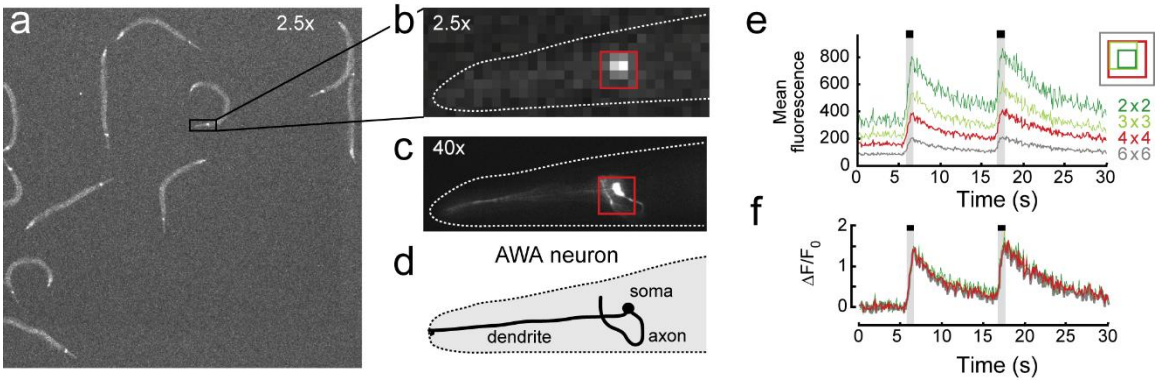

Figure 2-5 **Quantification of neural fluorescence from wide-field images.**
(**a**) Full field-of-view at 2.5x/0.12 N.A. showing 11 animals in the arena. (**b**) Magnified view of the head of one animal, directly magnified from panel **a**. (**c**) Same view after switching to 40x/0.75 N.A. Red boxes in **b**,**c** represent 4 x 4 pixel^2 (25.6 x 25.6 μm^2) integration region centered on the neuron soma. (**d**) Diagram of AWA neuron. (**e,f**) Neural fluorescence integrated across 2x2 to 6x6 pixel^2 boxes centered on the soma. Raw fluorescence (*F*) scales inversely with box size (**e**), but normalized fluorescence ($\Delta F/F_0$) is independent of box size (**f**). Larger boxes reduce artifacts due to imperfect tracking, and smaller boxes exclude nearby fluorescence such as gut autofluorescence.

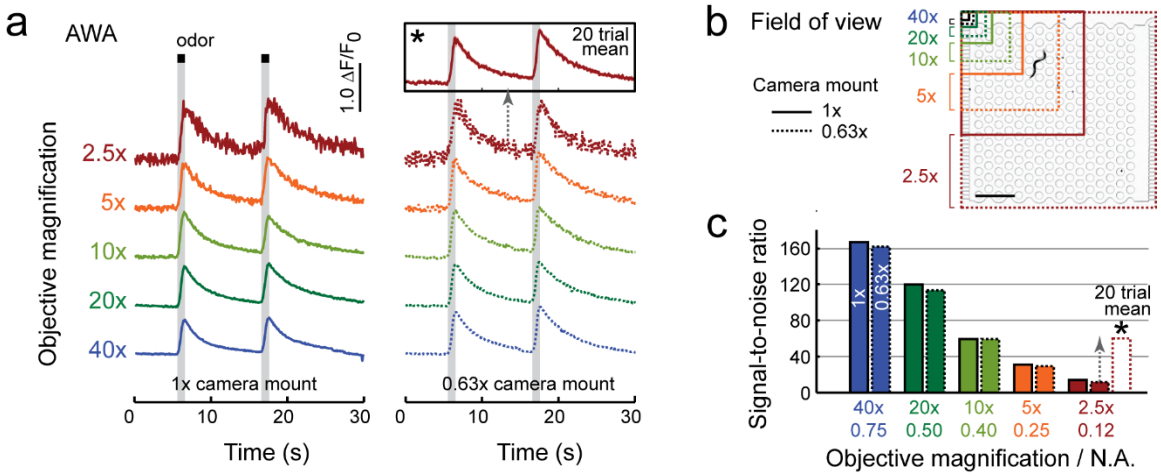

Figure 2-6 **AWA sensory neuron responses at various magnifications.**
(**a**) Representative fluorescence traces from a single animal subjected to two 1 s pulses of 1 µM diacetyl odor at the indicated objective magnifications (2.5x to 40x) with 1.0x (left panel) or 0.63x (right panel) camera adapters. The light source power level was adjusted, from 100% at 2.5x magnification to 3% at 40x magnification, for comparable baseline fluorescence at each magnification (pixel value ~1500). AWA neural fluorescence was obtained after downsampling images to 2.5x resolution (i.e., by factors of 2−16 for 5x−40x objectives) and integrating a 4x4 pixel^2 region corresponding to 25x25 µm^2 (1x adapter) or 40x40 µm^2 (0.63x). Magnitude and dynamics of responses did not change with objective magnification, but additional noise was present at lower magnifications. Noise was Gaussian, such that averaging *n* traces reduced noise by sqrt(*n*); for example, the average of 20 traces at 2.5x (*) resembles a single trace at 10x. (**b**) Comparison of the field of view at different magnifications, superimposed upon an adult animal in a microfluidic arena. Scale bar, 1 mm. (**c**) Signal-to-noise ratio (SNR) in calcium recordings from panel **a**, calculated as mean baseline fluorescence divided by standard deviation for the first 5 s of each trace before odor was applied. In each case the left bar is with 1.0x camera adapter and the right bar is with 0.63c camera adapter. N.A., numerical aperture. *, SNR for mean of 20 repeated trials.

High-throughput neural recordings in response to dynamic odor stimuli

A unique aspect of the wide-field imaging system is the ability to monitor at least 20 animals at once (Figure 2-7A), in contrast to high-magnification systems that focus closely on a single animal. Because maintaining the identity of so many moving animals is challenging, we first established that odor-evoked calcium transients in AWA sensory neurons were similar in the presence or absence of the paralytic acetylcholine agonist tetramisole (Lewis et al., 1980) (Figure 2-7B). Next, we measured 2,852 AWA calcium responses from a total of 40 immobilized animals subjected to repeated diacetyl pulses of varying concentration, duration, or rate of concentration change (*dC/dt*) (Figure 2-7).

All animals responded to diacetyl odor with increased fluorescence of the GCaMP2.2b indicator in AWA neurons (Figure 2-7C). Habituation was evident during the first few odor presentations, resulting in a ~20% reduction in peak magnitude over five trials (Figure 2-7C,D). The peak and the initial slope of the AWA calcium response showed a dose-dependent increase across a 105-fold diacetyl concentration range from 1 nM to 100 µM (Figure 2-7E,H). The calcium response rose throughout the 10-s odor pulse for low and high odor concentrations, but fell before odor was removed at intermediate concentrations (0.1−1 µM); this short-term densitization recovered in the 50 s before the subsequent odor pulse. Peak AWA calcium levels increased with odor duration up to the saturation point (2 s at 1 µM) (Figure 2-7F,I). The rate of odor concentration change (*dC/dt*) affected the magnitude, slope, and apparent latency of the neural response (Figure 2-7G,J). Thus, AWA sensory neuron dynamics reflect both the magnitude and the temporal properties of chemical stimuli.

Figure 2-7 **High-throughput recording of neural responses.**
(**A**) Camera frame showing 23 animals expressing G-CaMP2.2b in AWA neurons (arrowheads). (**B**) AWA sensory neuron responses are similar in freely-moving and paralyzed animals. Each curve represents mean fluorescence of one animal, n=20 trials each for 2 moving and 6 paralyzed animals. (**C**) Odor-evoked fluorescence during ten repeated 10 s pulses of 1 µM diacetyl at one pulse per minute. Each row represents an individual animal in panel **A**; orange trace is from the animal indicated by an orange arrowhead. (**D**) Mean peak AWA fluorescence and peak coefficient of variation (CV) for repeats 1–5 (dark blue) and 6–10 (light blue) calculated from data in panel **C**. (**E-G**) Mean AWA fluorescence response to systematic variation in (**E)** odor concentration (10 s pulses), (**F**) odor duration (1 µM diacetyl), (**G**) odor gradient (*dC/dt*) (5 s pulses, 0-1 µM diacetyl). Schematics on top represent time course of stimulus modulation, measured from fluorescein dye controls. Light shading on calcium traces depicts s.e.m. (**H-J**) Mean (blue) AWA peak fluorescence and time of response peak are influenced by odor concentration (**H**), pulse duration (**I**), and odor gradient (**J**), as calculated from traces in panels **E-G**. The peak response appeared saturated at 10 uM diacetyl (10 s pulse, E,H), and at 3 s of stimulation (1 uM diacetyl, F,I). C, control (buffer) stimulus. Orange curves represent the individual animal highlighted in panels **A**,**C**. For all data in **D-J,** error bars represent s.d., n=8–22 animals, one experiment per stimulus parameter, 6–12 trials per condition.

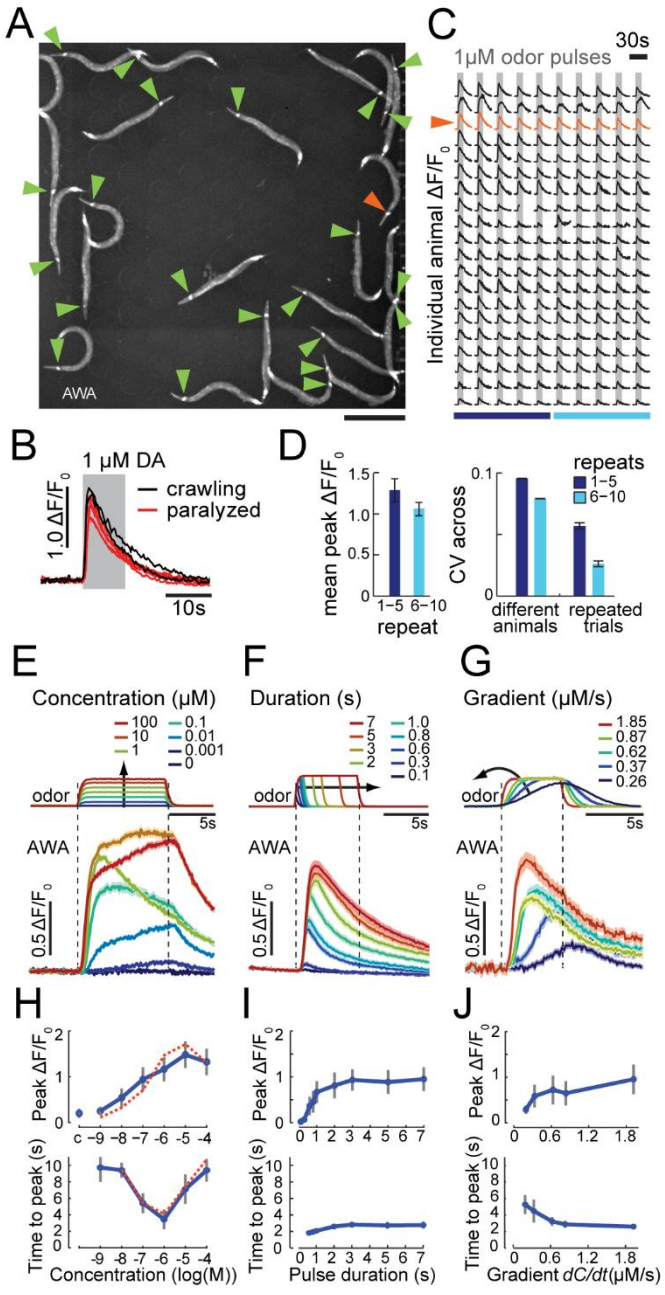
A
AWA
C
1μM odor pulses
30s
Individual animal ΔF/F0
B
1 μM DA
crawling
paralyzed
1.0 ΔF/F0
10s
D
mean peak ΔF/F0
1–5 6–10
repeat
CV across
repeats
1–5
6–10
different animals
repeated trials
E
Concentration (μM)
100
10
1
0.1
0.01
0.001
0
odor
5s
AWA
0.5 ΔF/F0
F
Duration (s)
7
5
3
2
1.0
0.8
0.6
0.3
0.1
G
Gradient (μM/s)
1.85
0.87
0.62
0.37
0.26
H
Peak ΔF/F0
Time to peak (s)
Concentration (log(M))
I
Pulse duration (s)
J
Gradient dC/dt (μM/s)

A single animal's response was reliable with respect to each stimulation parameter, but differences were observed across individual animals. Dose-response curves for individual animals yielded half-maximal effective concentration (EC50) that varied by two orders of magnitude (Figure 2-8). Response magnitude was more variable between animals than between repeated stimulation of one animal, and more variable for the first five trials than later repeats; hence, the most consistent calcium responses were obtained from an individual animal after a few preconditioning pulses (Figure 2-7D).

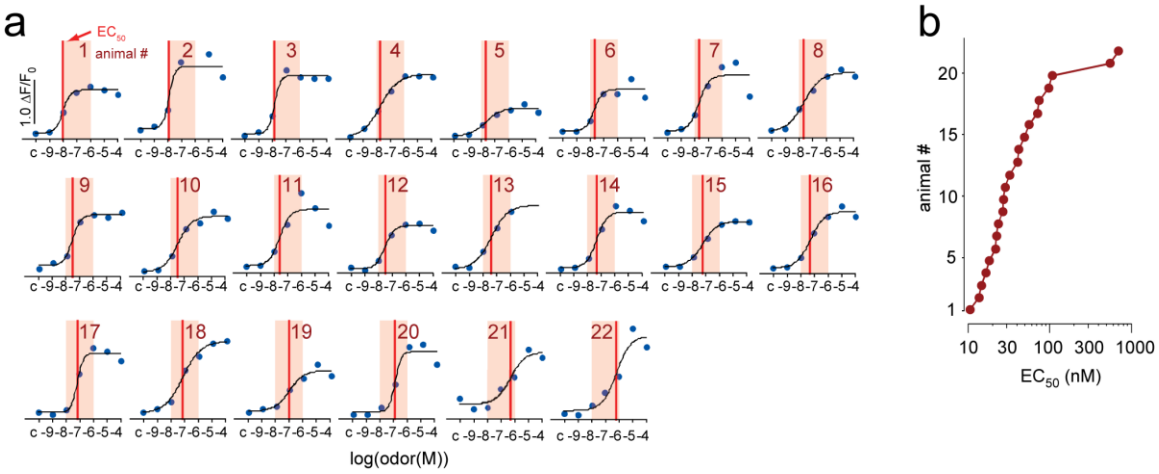

Figure 2-8 **Variable individual animal diacetyl dose-response curves.**
(**a**) Dose-response curves for 22 individual animals subjected to ten repeated 10 s pulses of diacetyl odor, from 1 nM to 100 µM in ascending sequence, one pulse per minute (70 mins total). c, buffer control. Combined data are presented in Figure 2. The odor concentration yielding a 50% peak response, the EC_{50}, was determined for each animal from a four-parameter sigmoidal curve fit. Vertical red lines indicate EC_{50}; shading indicates range across all animals. (**b**) Summary of diacetyl EC_{50} for the AWA neurons in 22 animals. Sensitivity varies by 1-2 orders of magnitude across these animals; median EC_{50} = 30.6 nM diacetyl.

Efficient determination of a neuron's chemical receptive field

In previous studies, laborious behavioral assays and laser ablation experiments demonstrated that each *C. elegans* chemosensory neuron detects multiple odors, tastes, or pheromone stimuli (Bargmann, 2006a). To more efficiently map chemical stimuli to sensory neurons, we used the wide-field imaging system to test AWA neural responses to 30 small-molecule odors (Figure 2-9A,B). Odors were delivered sequentially in triplicate from 96-well plates using ~60 µL sample per trial.

The known AWA-sensed odors diacetyl, pyrazine, 2,4,5-trimethylthiazole, and 2,3-pentanedione elicited robust calcium transients in nearly all tested animals (Figure 2-9A,B). Dose-response curves revealed a substantial variation across these four odors in sensitivity (Figure 2-9A). A broad survey of odors tested at 10^{-6} dilution showed that benzaldehyde and butanone, known to be detected primarily by AWC neurons, did not elicit reliable responses in AWA (Figure 2-9B).

Among previously uncharacterized odors, hexyl acetate elicited a response comparable to known AWA odors. Interestingly, several other 3- to 7-carbon acetates elicited responses in only a subset of animals (Figure 2-9B). These responses were consistently weak or strong across repeated stimulation of an individual, but uncorrelated to the strength of the individual's diacetyl response (Figure 2-9D,E and Figure 2-10).

Similar experiments in *odr-10(ky32)* mutant animals, which have a loss of function mutation in the diacetyl receptor (Sengupta et al., 1996), demonstrated greatly diminished AWA responses to 1 µM diacetyl, whereas responses for most other odors were preserved (Figure 2-9B,C). Mutant animals also failed to respond to the related odor 2,3-pentanedione, suggesting that ODR-10 contributes to its detection.

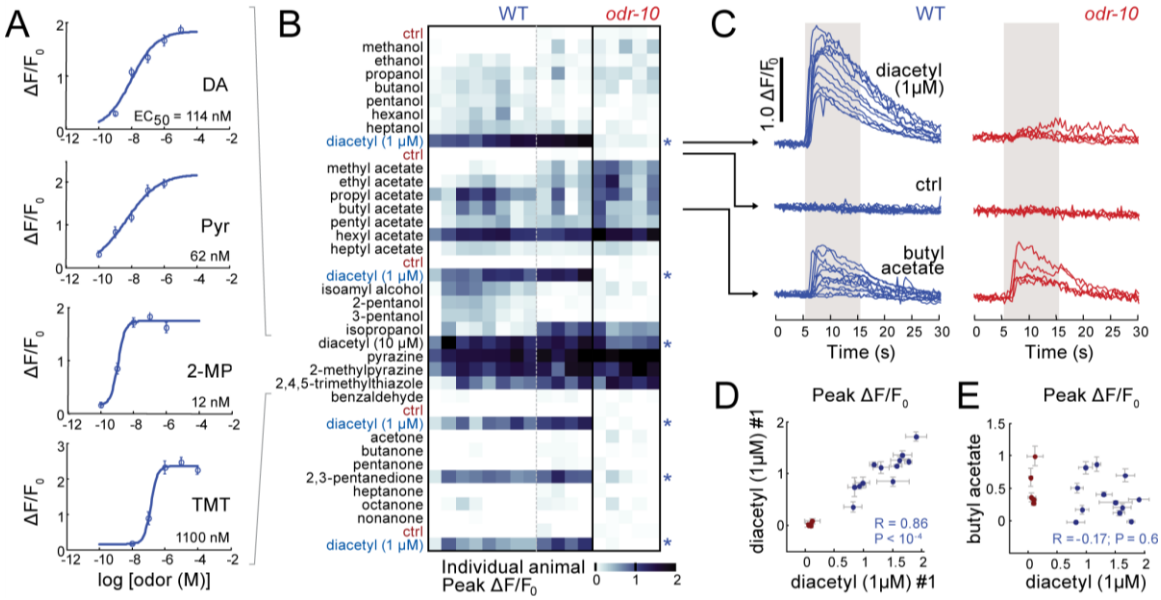

Figure 2-9 **Chemical screening of neural responses.**
(**A**) Neurometric curves of peak fluorescence in AWA neurons subjected to increasing concentrations of four odors. DA, diacetyl; Pyr, pyrazine; 2-MP, 2-methylpyrazine; TMT, 2,4,5-trimethylthiazole. Data are mean ± s.e.m., n=22 traces (1 experiment, 11 animals, 2 trials each). (**B**) Small-molecule odor screen for AWA-detected odors. Thirty odors (10^{-6} dilution) were presented from a 96-well plate, sequentially and in triplicate, to 12 wild-type (WT) and five *odr-10* mutant animals. Heatmap shows mean peak fluorescence following odor addition. Multiple positive controls (1 μM diacetyl) indicate neural sensitivity throughout the series, and negative controls (ctrl, S-basal buffer) show no contamination across odors. Data represent 2,456 traces from 17 animals in two experiments. Odors with reduced response in *odr-10* mutants are indicated by *, P<0.05 via ANOVA with Benjamini-Hochberg correction. (**C**) Individual animal mean responses to diacetyl, S-basal buffer, and butyl acetate for WT (blue) and *odr-10* mutants (red). (**D,E**) Peak AWA response to diacetyl is strongly correlated with a second presentation of diacetyl (P<0.0001, panel **D**) but uncorrelated with response to butyl acetate (P=0.6, panel **E**). Points represent mean of each animal and error bars are s.e.m. for n=3 trials per animal.

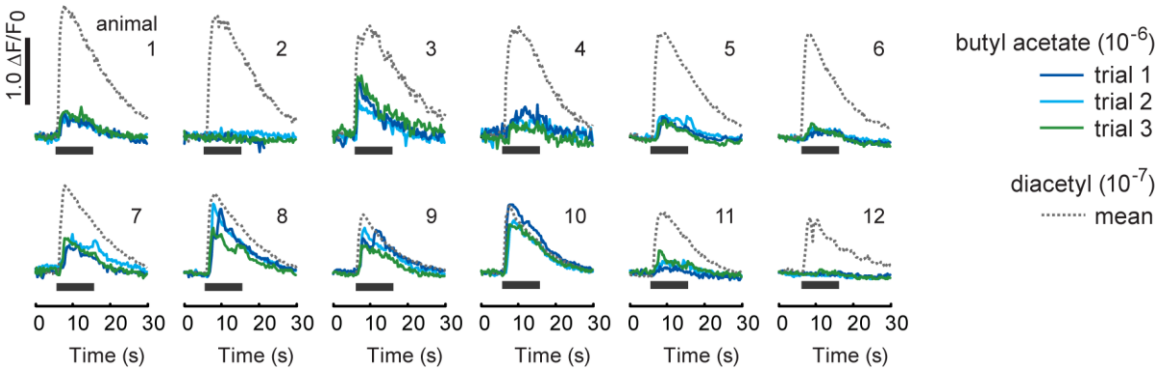

Figure 2-10 **Variable responses to butyl acetate across animals.**
Plots represent AWA calcium responses from three successive trials (colored) of twelve individual wild-type animals to a 10^{-6} dilution of butyl acetate during the odor panel experiments (Figure 3). Gray dotted line indicates the mean response of three presentations of diacetyl odor (10^{-7} dilution), recorded in the same animals prior to butyl acetate responses. Each animal consistently responded strongly or weakly to butyl acetate over the three trials, and all animals responded strongly to diacetyl.

Pharmacological modulation of neural activity

High-throughput pharmacological screening of *C. elegans* can identify new modulators of conserved biological pathways as well as antihelminthic agents (Kwok et al., 2006; Lockery et al., 2012; Petrascheck et al., 2007). One such screen and subsequent genetic analysis identified nemadipine-A as a compound that induces morphological and egg-laying defects by antagonizing the α1-subunit of *C. elegans* L-type voltage gated calcium channels, EGL-19 (Kwok et al., 2006). Reduced-function mutations in *egl-19* and other L-type calcium channel blockers decrease stimulus-evoked calcium transients in ADL (Suzuki et al., 2003), ASH (Hilliard et al., 2005) and URX (Busch et al., 2012) sensory neurons, implicating the L-type channel in sensory activity. We assessed the suitability of the high-throughput system for chemical screening by examining the effects of nemadipine-A on AWA calcium transients. Animals were challenged with nine diacetyl pulses to establish a baseline response, then switched to 10 µM nemadipine-A for the next ten diacetyl pulses, then returned to initial conditions (Figure 2-11A). Within 1 minute in nemadipine-A, the AWA calcium response was suppressed by ~70%; this suppression recovered in 1-2 minutes after washout (Figure 2-11B).

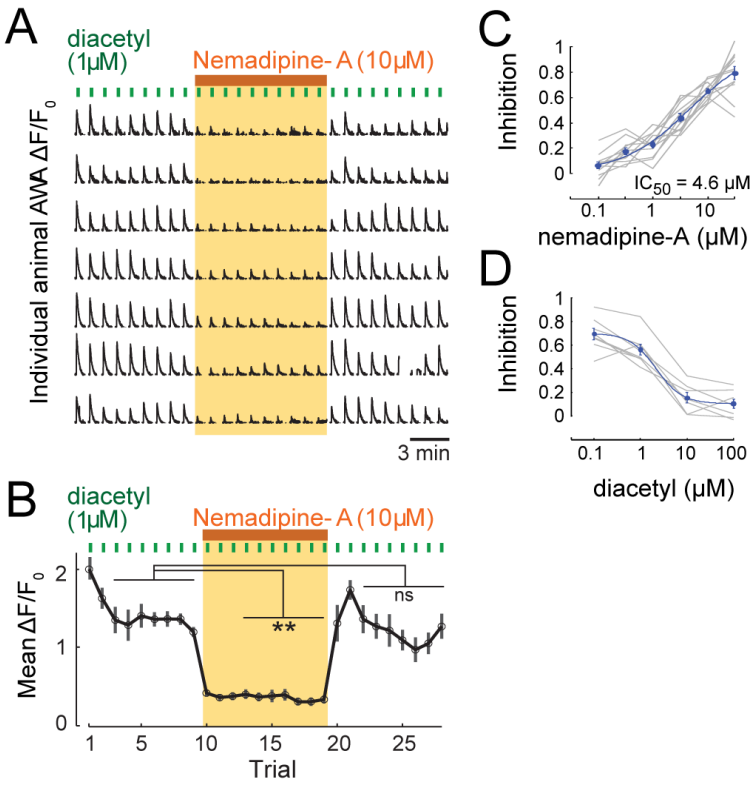

Figure 2-11 **Pharmacological modulation of neural responses to odors.**
(**A)** Seven animals were subjected to repeated 1 μM diacetyl odor pulses (10 s) in the presence or absence of 10 μM nemadipine-A, an L-type calcium channel antagonist. Rows represent odor-evoked AWA calcium transients in individual animals measured simultaneously. Each trial was repeated once per minute. (**B**) Peak fluorescence response per trial after odor addition. Error bars indicate s.e.m., n=7 animals from A. **, P<0.001; ns, not significant. (**C**) Dose response curve for nemadipine-A inhibition of responses to 1 μM diacetyl odor stimulation. Mean ± s.e.m., n=12 animals, 6 trials per concentration, 1 experiment. Blue curve is sigmoidal fit and grey lines represent individual animal curves. (**D**) Dose response curve for inhibition of diacetyl response by 10 μM nemadipine-A, which increases the EC_{50} about 100-fold from 30 nM (Figure 2-8) to 2.5 μM DA. Mean ± s.e.m., n=8 animals, 6 trials per concentration, 1 experiment.

A dose-response curve for nemadipine-A inhibition of AWA calcium transients yielded an IC_{50} of 4.6 μM nemadipine A (Figure 2-11C), comparable to its 1–5 μM IC_{50} for egg-laying and morphological phenotypes (Kwok et al., 2006). Nemadipine-A strongly inhibited AWA responses to low diacetyl concentrations, but had minimal effects at saturating diacetyl levels (Figure 2-11D), suggesting that the voltage-gated EGL-19 channel amplifies AWA calcium signals to weak odor stimuli.

Neural activity during free-moving behavioral responses

Direct observation of neuronal activity in unrestrained animals is essential for understanding how neural signals guide behavior. One interesting aspect of behavior is its variability in apparently constant conditions. For example, when *C. elegans* experiences removal of the attractive odor isoamyl alcohol (IAA), which is sensed by AWC sensory neurons, it can generate a pirouette (a reversal coupled to a sharp omega turn) or just a reversal, or it can fail to respond at all (Albrecht and Bargmann, 2011; Pierce-Shimomura et al., 1999). To characterize the neural signals associated with these responses, we subjected freely-moving animals to 60 repeated IAA pulses and simultaneously recorded behavior and calcium transients in one AWC neuron using the GCaMP3 calcium sensor (Figure 2-12A-C). Regardless of the behavioral outcome, the animal's AWC calcium transients had similar response dynamics and magnitude (Figure 2-12C-E). These observations suggest that AWC calcium transients reliably report sensory input and that the variable behavioral response arises at a different site. Individual animals expressing GCaMP in AWA or ASH sensory neurons also showed consistent calcium transients upon diacetyl or glycerol addition, respectively, despite behavioral responses that varied across trials (Figure 2-12E).

Contrasting results were obtained in the same IAA odor stimulation paradigm when calcium was monitored in the AVA command interneurons, which drive backward locomotion (Chalfie et al., 1985). AVA calcium levels were coupled to the behavioral output, not the sensory input, rising during ~90% of reversals and declining during forward motion (Figure 2-12F). The fraction responding and dynamics of the AVA response were similar to previous recordings of AVA during spontaneous reversals

using high-magnification tracking systems (Ben Arous et al., 2010; Faumont et al., 2011; Piggott et al., 2011).

Detection of subcellular calcium transients in interneurons

In AIA and AIY interneurons, calcium transients occur primarily along axonal processes rather than in cell bodies (Chalasani et al., 2007, 2010). To accommodate weaker fluorescent signals, we used a 5x/0.25 NA objective and 0.63x demagnification lens for substantially higher light-gathering power at a similar spatial resolution (5.1 µm/pixel) and field-of-view (2.6 x 2.6 mm2) than the 2.5x/0.12 NA objective (Figure 2-12G,I).

We measured AIA interneuron activity in moving animals by tracking the bright cell body and integrating fluorescence in a larger region that included a portion of the axon. Calcium levels in AIA interneurons increased upon diacetyl addition and fell immediately when odor was removed (Figure 2-12H), like previously reported responses of AIA neurons to IAA odor in trapped animals (Chalasani et al., 2010). Calcium levels also rose in neurites of the AIY interneurons upon addition of diacetyl or IAA, although no responses were observed in the AIY cell body to either odor (Figure 2-12J).

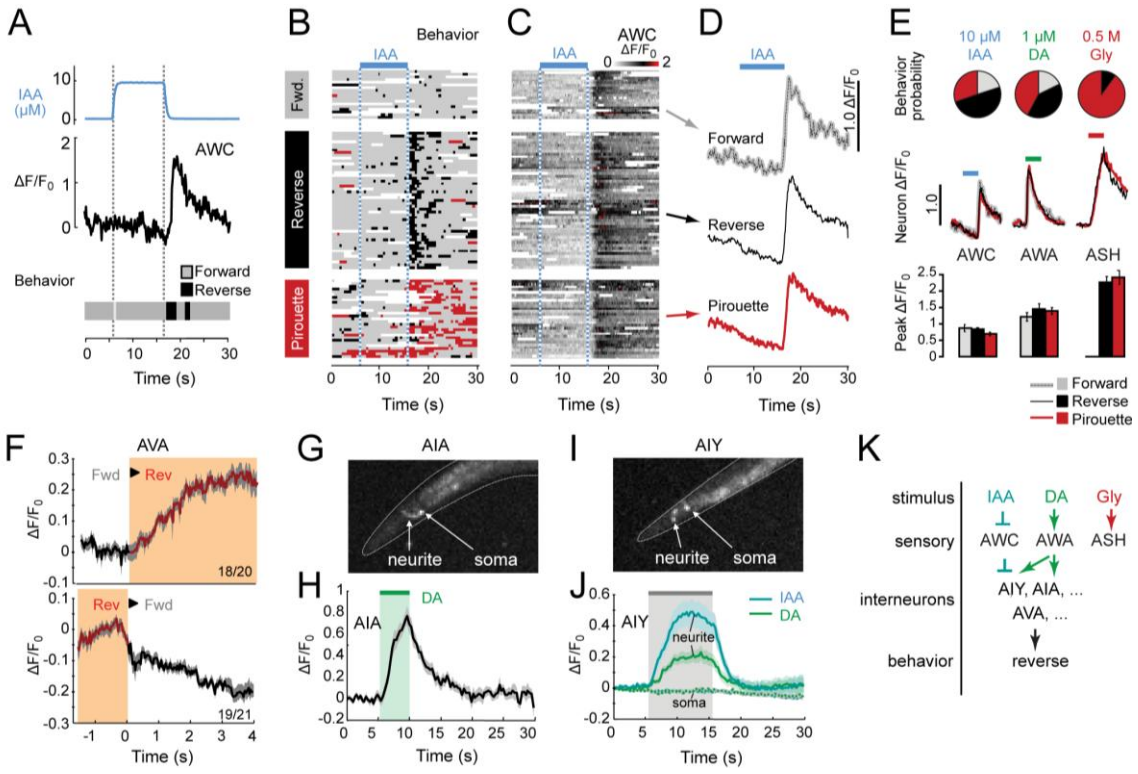

Figure 2-12 **Sensory neuron, interneuron, and behavioral responses.**
(**A**) Time course of odor stimulation, AWC^{ON} neuron fluorescence, and locomotory behavior in a single animal following 10 μM isoamyl alcohol (IAA) odor stimulation. Black indicates short reversal; gray, forward movement. (**B**) Ethogram of behavioral responses, grouped by predominant response to odor removal: *Forward*, short *Reverse*, or *Pirouette* (coupled reversal and omega turn). Red indicates the long reversal component of a pirouette response. White, missing data. (**C**) AWC^{ON} activity corresponding to each trial (row) in **B**. (**D**) Average AWC^{ON} fluorescence for each behavioral response group in **B**. (**E**) Behavior response probability and superimposed behavior-calcium average traces for AWC (data from **D**) and from AWA stimulated by 1 μM diacetyl (DA) and ASH stimulated by 0.5 M glycerol (Gly). No significant differences were seen between peak calcium levels associated with different behaviors. Data in **B**-**E** are from two animals tested individually per neuron-stimulus pair, 60 trials per animal. (**F**) AVA (backward command interneuron) activity in freely-moving animals stimulated with IAA odor rose upon initiation of reverse movement and fell after reversal termination. (**G**) GCaMP expression in AIA interneuron neurites and soma. (**H**) Time course of AIA response to 1 μM DA stimulation in freely-moving animals. AIA fluorescence was integrated in a 6 x 6 pixel area that included the cell body and a portion of the neurite. Shading indicates s.e.m., n=18 traces from 4 animals, 1 experiment. (**I**) AIY::GCaMP expression. The two anterior bright spots represent integrated fluorescence across the neurite. (**J**) AIY responses to 10 s pulses of 10 μM IAA and 1 μM DA recorded at the neurite or soma in stationary animals. Shading indicates s.e.m., n=70 traces from 7 animals, 1 experiment. (**K**) Partial list of neurons transducing stimulus information to behavioral response. Pointed and T-shaped arrows indicate functional excitatory and inhibitory interactions confirmed in this work, respectively.

Responses to spatial odor patterns

Whereas temporal stimulus patterns, such as odor pulses, provide a uniform stimulus history to many animals across repeated experiments, spatial odor patterns may better approximate sensory signals experienced during goal-directed tasks such as chemotaxis. To demonstrate the ability to correlate behavior and neural activity in response to spatial chemical patterns, we used a modified microfluidic device that presented a stable ~1 mm wide stripe of odor with a sharp interface at the stripe edge (Albrecht and Bargmann, 2011) (Figure 2-13A and Figure 2-2). As a freely-moving animal left the 1 µM IAA odor stripe, AWC fluorescence increased sharply, often preceding a reversal or pirouette behavior that reoriented the animal back into the attractive odor (Figure 2-13B). A second device presented a linear odor gradient (300 µM/mm IAA) across the arena (Figure 2-13C). Each excursion down the odor gradient elicited AWC neural activity, frequently followed by reversal or turning behaviors that returned the animal to an elevated odor concentration (Figure 2-13D,E). The intervals between odor decrease, neural activation, and reversal response were longer in the shallow stimulus gradient (up to several seconds) than they were at the sharp odor edge of a stripe; on average an animal traversed 0.6 mm down the gradient before responding with a reorienting behavior (Figure 2-13E).

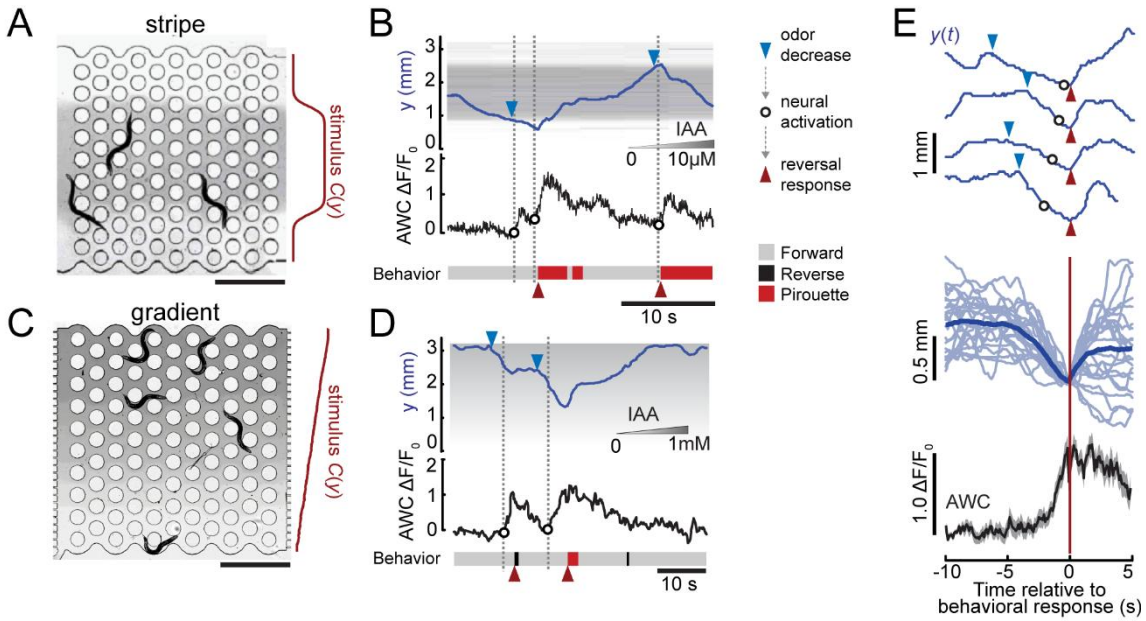

Figure 2-13 **Neural and behavioral responses to spatial odor patterns.**
(**A**) Brightfield image of the microfluidic arena presenting a stable horizontal fluidic stripe (visualized with dye). Scale bar, 1 mm. (**B**) Time course of *y*-axis position and AWC neuron fluorescence of a single animal responding to a stripe of isoamyl alcohol (IAA) odor. Vertical lines and open circles indicate the onset of AWC activity increase, which coincided with odor decrease at the lower or upper stripe edge (blue arrowheads) and preceded the onset of behavioral responses (red arrowheads). (**C**) Brightfield image of a linear odor gradient (visualized with dye). Scale bar, 1 mm. (**D**) *y*-axis position and AWC fluorescence of one animal responding to a linear IAA gradient. labels as in B. (**E**) Temporal alignment of position in a linear gradient to the initiation of reversal or pirouette responses. Four representative descents are shown, indicating the onset of gradient descent (blue arrowheads), increased AWC activity (circles), and behavioral response (red arrowheads). Below, individual trajectories, mean relative position, and mean AWC fluorescence for 24 gradient descents aligned to the onset of reversal response. Shading indicates s.e.m., n=2 animals from independent experiments.

Acknowledgments

We thank S. Flavell, A. Gordus, P. Kong, Y. Xu and P. Roy for facilitating experiments with reagents and advice; and T. Geer and D. Szent-Gyorgyi (Biovision) for assistance with microscope hardware and automation and the Leibler lab for use of their clean room. DRA holds a Burroughs Wellcome Fund Career Award at the Scientific Interface; JL was supported by a Boehringer Ingleheim Fonds graduate fellowship; and CIB is an Investigator of the Howard Hughes Medical Insititute. This work was funded by HHMI and by a grant from The Ellison Medical Research Foundation.

Chapter 3 Acute adaptation in a chemotaxis circuit of *Caenorhabditis elegans*

Summary

Spatial orientation is a ubiquitous problem in biology. The compact nervous system of the soil nematode *Caenorhabditis elegans* is ideally suited to reveal the circuit implementation of computations underlying oriented navigation through space. In *C. elegans,* food odors regulate the frequency of stereotyped turning events, ultimately driving animals to the odor source via klinokinesis, a biased random walk strategy analogous to chemotaxis of *E. coli* in nutrient gradients. This behavioral strategy requires differential stimulus representation that is sensitive to changes in rather than absolute levels of odor concentrations. Here, we present a survey of neuronal activity in the chemotaxis circuit and behavior of *C. elegans*. Odor-evoked responses at the sensory level adapted within seconds and were further sharpened in a downstream interneuron, yielding sensitive fold-change detection over two orders of magnitude in odor concentration. Mutations in genes with conserved roles in ciliary function affected the dynamics of adaptation. Fold-change detection was preserved at the behavioral level, demonstrating that *C. elegans* can reliably detect changes in odor concentration to navigate odor gradients. This work sheds light on the biological implementation of an adaptation-based algorithm that may underlie acute computation during spatial orientation.

Introduction

Natural environments offer regions that differ in their value to organisms, for example, by providing more nutrients, suitable mating partners, or shelter. As a result sophisticated sensory systems have evolved to allow animals to navigate to favorable conditions. Design principles derived from animal navigation are fundamental examples of sensorimotor transformations within nervous systems that relate behavior to external stimulation. Some of these have inspired biomimetic engineering of autonomous robots that mimic spatial computations performed by animals (Franz and Mallot, 2000).

The nematode worm *C. elegans* orients in response to many external sensory cues including temperature, osmolarity, light and water soluble as well as volatile chemicals (Bono and Villu Maricq, 2005). For example, animals migrate towards food odors in a process called chemotaxis. *C. elegans* locomotion in isotropic environments alternates between relatively straight ‘runs’ and sporadic ‘turns’ of random orientation, resembling a random walk (Berg, 1993; Pierce-Shimomura et al., 1999). Animals chemotax in odor gradients by prolonging runs in the efficient orientation, towards attractants or away from repellents, relative to the inefficient orientation, reminiscent of the biased random walk observed in bacterial chemotaxis (Berg, 2004; Pierce-Shimomura et al., 1999).

A remarkable feature of chemotaxis is its robustness and sensitivity over several orders of magnitude in odor concentration. For example, the odor diacetyl elicits chemotaxis over at least seven orders of magnitude in odor concentration (Bargmann et al., 1993), suggesting active mechanisms for keeping the underlying sensory system within dynamic range. It has thus been hypothesized that animals monitor relative changes rather than absolute odor concentrations (Bono and Villu Maricq, 2005). In addition,

theory suggests that biased random walks require differential stimulus representation (Benhamou and Bovet, 1989). One mechanism to differentiate an input is response adaptation. Adaptation converts the initially strong response to a stimulus to a lower steady state level even if the stimulus persists. After adaptation diminishes the response, the system may be able to respond to another increase in stimulus intensity. Adaptation is a functionally conserved mechanism across phyla and sensory modalities including bacterial chemotaxis (Berg and Brown, 1972), invertebrate and vertebrate olfaction (Reisert and Zhao, 2011; Wilson, 2013) and vision (Montell, 2012; Rieke and Rudd, 2009)

Special cases of adaptation are defined by the exact relationship of the response intensity to the stimulus level. In perfect or exact adaptation, responses return to the baseline level at steady state, regardless of stimulus intensity. Exact adaptation is implemented as a robust internal control feedback mechanism in bacterial chemotaxis (Barkai and Leibler, 1997).

If two increases in stimulus intensity of the same relative magnitude (i.e. 1 to 2 and 2 to 4, both constitute a two-fold increase) cause the same response, the system performs fold-change detection (FCD) (Goentoro et al., 2009; Shoval et al., 2010). Certain molecular responses such as beta-catenin accumulation stimulated by Wnt and nuclear entry of MAPK stimulated by EGF exhibit FCD (Cohen-Saidon et al., 2009; Goentoro and Kirschner, 2009). FCD is reminiscent of Weber's law, derived from psychophysical experiments in the visual system, which says that the just noticeable difference between two stimuli is proportional to stimulus magnitude (Weber, 1905). FCD is defined stricter than Weber's law, requiring conserved response dynamics across stimulus levels whereas Weber's law is satisfied with conserved peak response magnitude.

Five chemosensory neurons mediate odor responses in *C. elegans* and specificity amongst neurons is endowed by selective expression of different sets of olfactory receptor genes (Bargmann, 2006b). Laser ablations and genetic analysis revealed that diacetyl chemotaxis is driven by AWA sensory neurons at certain odor concentrations (Bargmann et al., 1993; Sengupta et al., 1996) providing an entry point to the neural basis of chemotaxis. Behavioral analysis showed that *C. elegans* regulates turns in response to changes in odor concentration rather than absolute odor levels (Iino and Yoshida, 2009; Pierce-Shimomura et al., 1999), supporting a role for adaptation in chemotaxis. At the neuronal level, odor-evoked responses in several sensory neurons including AWA exhibit short term adaptation (Hilliard et al., 2004; Larsch et al., 2013; Suzuki et al., 2008).

We hypothesized that adaptation of odor-evoked AWA activity provides a cellular mechanism to sensitize AWA to fold changes, thus enabling chemotaxis over a wide range of odor concentrations. We systematically measured neuronal responses to odor in the diacetyl chemotaxis circuit and followed odor-evoked activity from AWA sensory neurons to connected downstream interneurons where it is integrated with activity from other neurons. Adaptation of neuronal responses to odor yielded a sensitive response to small increases in odor concentration in AIA interneurons that were necessary for behavior, providing a mechanism for efficient gradient sensing. Adaptation dynamics at the sensory level were stimulus-dependent and cell-autonomously altered in several classes of mutants.

Behavioral responses to different concentrations of diacetyl resulted from overlapping contributions from multiple sensory neurons. AWA was specifically required for transient orientation behavior in response to small increases in odor concentration that are encountered in shallow gradients, demonstrating functional specialization amongst sensory neurons for particular stimulus characteristics.

Results

AWA neural dynamics reveal adaptation on multiple time scales

AWA sensory neurons respond to diacetyl pulses with dose-dependent calcium transients (Larsch et al., 2013; Shinkai et al., 2011). We found odor-evoked responses to be strongly dependent on stimulation history, prompting the analysis of response adaptation and its implications for chemotaxis.

During continuous stimulation with diacetyl, AWA calcium fell within 30 s to a low steady state level that was maintained for 5 minutes until diacetyl was removed (Figure 3-1a). To better understand the dynamics of desensitization, we stimulated animals with pairs of short odor pulses at varying intervals (Figure 3-1b). AWA responses to the first pulse of each pair were consistent, but short inter-pulse intervals diminished responses to a second pulse. The effect on the second pulse was largest with an interval of four seconds but recovered for intervals longer than ten seconds (Figure 3-1b). Desensitization could be overcome by stimulation with higher odor concentrations, indicating that this process represents a reduction in sensitivity rather than a general inability to respond (Figure 3-1c).

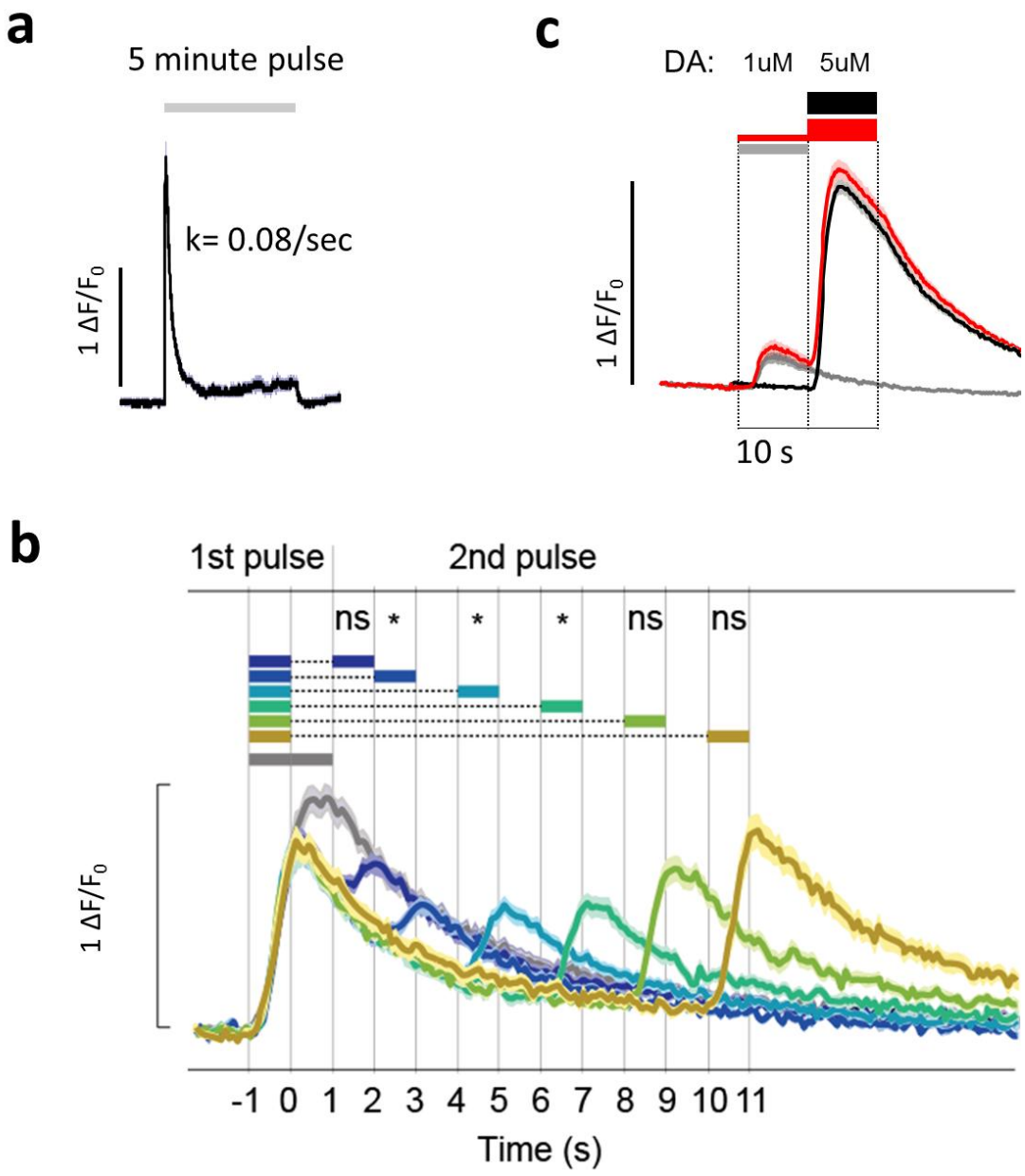

Figure 3-1 **Rapid desensitization of odor-evoked AWA calcium transients.**
(**a**) Mean AWA response (relative GCaMP fluorescence, $\Delta F/F_0$) to 5 min pulse of 1uM diacetyl (gray horizontal bar); trace shading = S.E.M, n = 12 animals, 3 stimulations each. (**b**) A short 1 uM odor pulse reduces subsequent responses for 3-6 s. Mean AWA fluorescence to 1 s paired pulses with 1-10 s inter-pulse interval and 60 sec between pulse pairs. Horizontal bars above traces indicate pulse timing, colors relate pulse timing to respective AWA responses. (*P<.001; ns, not significant versus first pulse by ANOVA and Bonferroni's correction for multiple comparisons). (**c**) Desensitization of AWA response to 1 µM diacetyl (red) is overcome by stimulation with 5µM diacetyl (red). Shading shows s.e.m., n=63 traces from 9 animals x 7 trials.

Responses to odors also changed gradually on a minute time scale. In a five hour experiment, we pulsed animals once per minute with a 5 s pulse of 1 uM diacetyl (Figure 3-2a). Peak AWA calcium responses fell rapidly during the first 5-10 odor pulses, then more slowly over the next ~300 pulses (Figure 3-2a). The degree of habituation to 10 s stimuli depended on the pulse duty cycle, with shorter inter-pulse intervals leading to greater habituation (Figure 3-2b).

Habituation re-scaled odor response magnitude but preserved the desensitization property of a given odor concentration (Figure 3-2c-e). For example, the peak magnitude of the response to 0.1 uM diacetyl fell over 50% after 5 pulses, but the characteristic within-pulse desensitization at this concentration was always preserved. Thus, sustained stimulation and intermittent stimulation at a given odor concentration reduce odor responses in distinct ways.

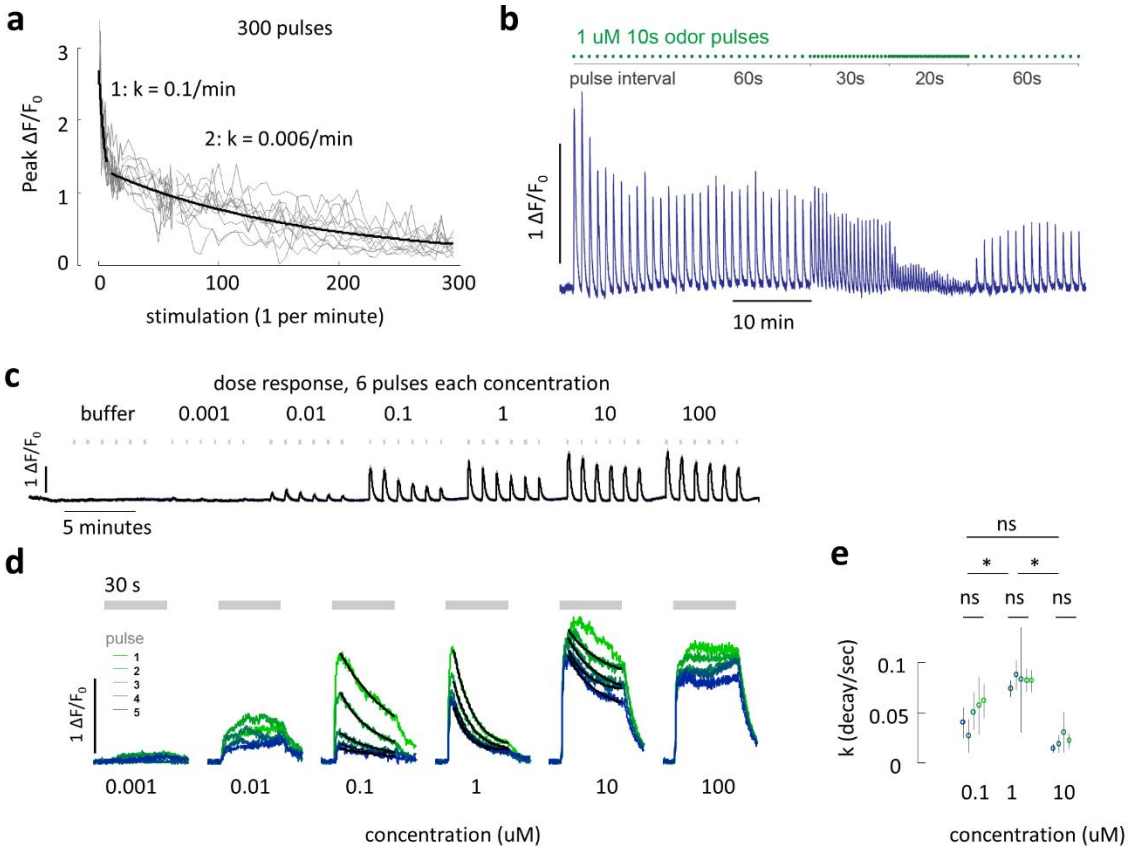

Figure 3-2 **Habituation of odor-evoked AWA calcium transients.**
(**a**) Mean peak AWA fluorescence during repeated stimulation for 5 s every 60 s at 1 uM. Gray: 11 individual animals, black: best fit to the equation $y = y_0*\exp(-k*t)$ separately during two phases: 1, pulses 1-7, 2, pulses 11-300. (**b**) Mean AWA response to stimulation with 10 s pulses at 1 uM diacetyl depends on the inter-pulse interval. (**c**) Mean AWA fluorescence during odor stimulation at six concentrations. Each stimulus is presented six times for 10 s separated by 60 s and additional 60 s between concentration blocks. Shading = s.e.m. n = 21 animals. (**d**) Concentration dependent AWA response dynamics are preserved during adaptation. Traces are mean AWA fluorescence during 5 repeated stimulations in five blocks representing one concentration each. Pulse order within each block is color coded: green, first; blue, last. Black lines are best fit to the equation $y = c + y_0*\exp(-k*t)$. n = 9 animals. The first response to 10 uM was not fitted because its shape was inconsistent with the model. (**e**) Response decay k is consistent across repeated pulses of the same concentration but different between concentrations (same data and colors as in **d**) (*P<.01; ns, not significant).

We extended AWA calcium imaging to a panel of genetic mutants in cellular odor signaling components to dissect the molecular requirements for odor sensing and desensitization. Dose-response measurements of AWA calcium transients showed a ten thousand fold reduction in sensitivity of AWA in *odr-10(ky32)* receptor mutant animals compared to wild type animals (Figure 3-3), confirming ODR-10 as the sole receptor in AWA for behaviorally relevant concentrations of diacetyl. G-Protein signaling downstream of *odr-10* converges onto a group of three TRPV channel proteins (Bargmann, 2006a). No calcium responses were observed in *osm-9(ky10)* TRPV mutant animals up to 100 uM diacetyl (Figure 3-3) and o*cr-2(ak47)* mutants were one thousand fold less sensitive than wild type (Figure 3-3). *ocr-1/ocr-2* double mutants were as defective as *osm-9* mutants (Figure 3-3). These results confirm that the OSM-9/OCR-2/OCR-1 TRPV channels are strictly required for AWA signaling to odor, and reveal partially redundant roles for OCR-1 and OCR-2 in stimulating calcium influx.

Downstream of TRPV, voltage gated calcium channels (VGCCs) can amplify calcium currents and odor-induced depolarization. The L-type VGCC blocker nemadipine acutely reduces calcium responses in AWA (Kwok et al., 2006; Larsch et al., 2013), and AWA calcium responses in *egl-19(n582)* partial loss of function mutants in the L-type VGCC were strongly reduced across all concentrations (Figure 3-3). In agreement with behavioral and genetic analysis, AWA calcium responses did not require the cyclic nucleotide channel subunits *tax-4* or *tax-2* (data not shown), which are necessary for signaling in other sensory neurons such as AWC and ASE (Bargmann, 2006a; Suzuki et al., 2008).

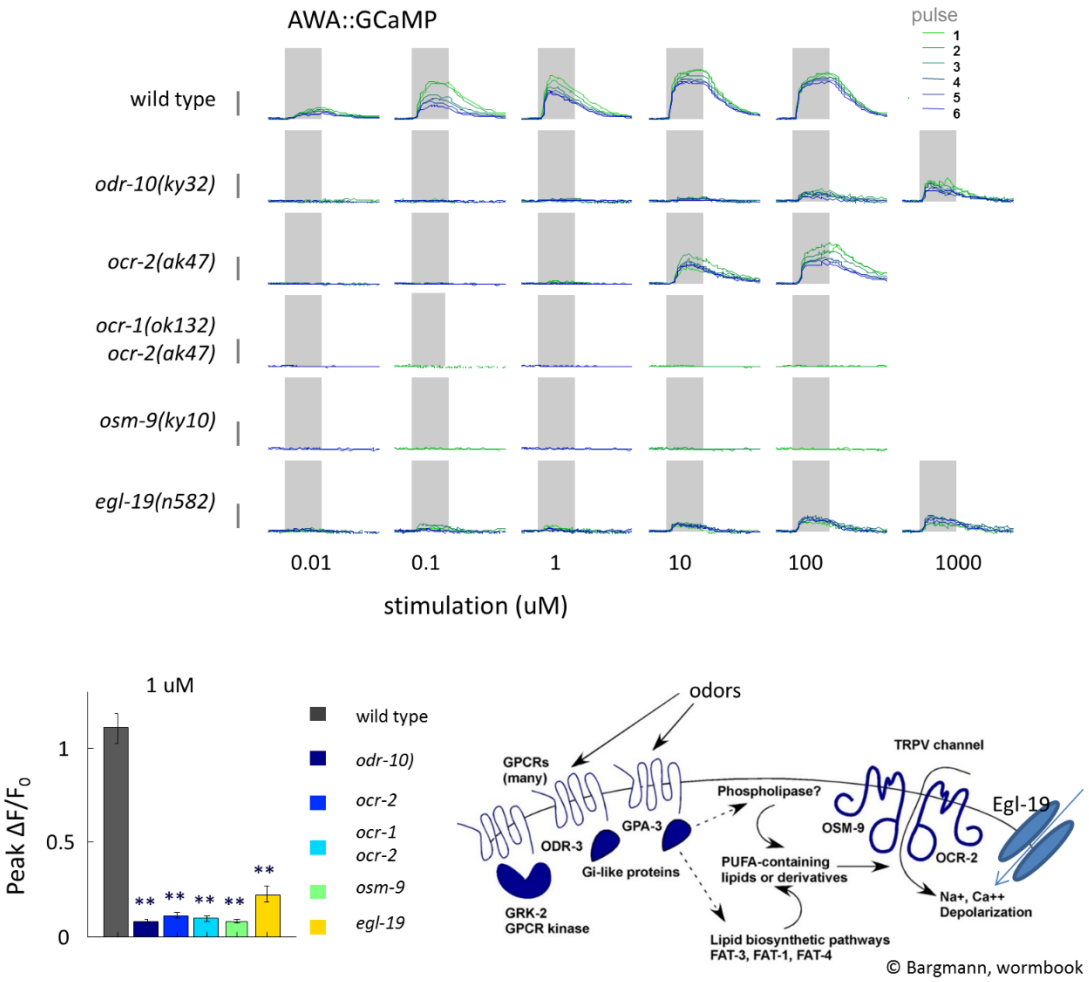

Figure 3-3 **AWA odor responses are lost in sensory transduction mutants.**
(Top) mean AWA fluorescence during dose response experiments using 10 s pulses and six stimulations at each concentration. No switch: baseline fluorescence without actuation of the stimulus switching valve. Buffer: stimulation from a separate buffer reservoir. Vertical bar to the left indicates 1 $\Delta F/F_0$. Gray shading indicates odor stimulus. (Bottom) Peak AWA fluorescence during stimulation at 1 uM. (**P<.0001 versus wild type). Schematic of AWA chemosensory signal transduction pathways adapted from (Bargmann, 2006a).

Modulators of the sensory response to diacetyl pulses

To test if desensitization of the calcium response is intrinsic to AWA or mediated by feedback from other neurons, we tested *unc-13* and *unc-18* mutants that have severely reduced synaptic transmission (Richmond et al., 1999; Weimer et al., 2003). *Unc-18(e234), unc-13(e51) and unc-13(s69)* had odor responses that decreased normally within and across odor pulses, suggesting that desensitization and habituation are independent of synaptic input (Figure 3-4). Unexpectedly, CB450 *unc-13(e450)* mutant animals did not show fast desensitization at any odor concentration. Instead, calcium rose and plateaued during a 10 s stimulation (Figure 3-4). Using high throughput imaging, linkage analysis, and whole genome sequencing, we determined that the defect was not caused by the *unc-13* mutation but rather by a linked mutation in *che-3*, the cytosolic dynein heavy chain motor protein (Wicks et al., 2000). *che-3* is 0.37 map units from *unc-13*, explaining why the two alleles co-segregated. The canonical loss of function allele *che-3(e1124)* had the same AWA defects as CB450, suggesting that enhanced AWA responses in *CB450* represent the effect of loss of function of the CHE-3 motor protein (Figure 3-4).

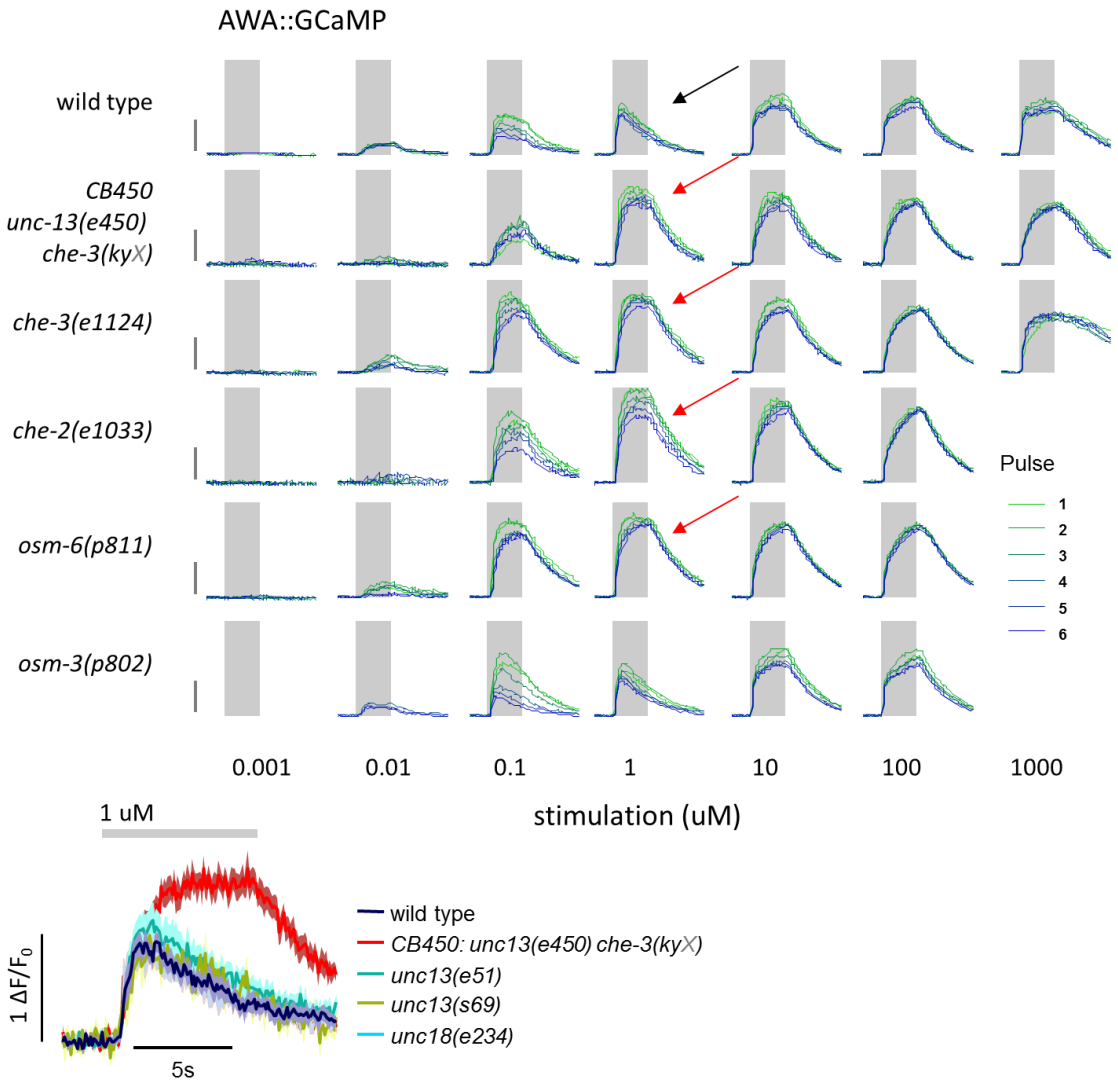

Figure 3-4 **Fast desensitization is lost in several mutants in the IFT machinery.** Traces are mean AWA fluorescence during odor stimulation, n=5-10 animals per genotype. Gray shading indicates odor stimulus. Wild type responses desensitize at intermediate concentrations (black arrow) but IFT (intraflagellar transport) mutants did not desensitize (red arrows). The anterograde IFT motor *osm-3* is required for morphogenesis of channel cilia, but does not affect AWA. (Bottom) other alleles of *unc-13* and one allele of *unc-18* showed normal desensitization at 1 uM diacetyl, shading: s.e.m. n=5-10 animals per genotype, 1 pulse each.

Intraflagellar transport mutants have defects in desensitization and habituation

Olfactory receptor neurons detect chemicals in specialized membrane compartments termed cilia that are structurally conserved across metazoans (Bargmann, 2006a; Doroquez et al., 2014; Perkins et al., 1986). *che-3* falls within a group of genes involved in intraflagellar transport (IFT) that are necessary for cilia morphogenesis and have been implicated in an emerging class of diseases know as ciliopathies (Gerdes et al., 2009). IFT mutants in *C. elegans* generally fail to chemotax to a variety of sensory cues (Perkins et al., 1986).

We confirmed the structural defect of AWA cilia by fluorescence imaging of AWA::GFP in *che-3(e1124)* as well as other IFT mutants such as the IFT adaptor OSM-6 (Fig.5 and data not shown) (Collet et al., 1998). Although there was an AWA structural defect in these mutants, we found that *che-3(e1124), osm-6(p811)* and *che-2(e1033),* another IFT adaptor mutant (Fujiwara et al., 1999) had stronger odor-evoked calcium transients than wild type in AWA at intermediate odor concentrations (Figure 3-4, Figure 3-5). Moreover, responses in the IFT mutants showed no fast desensitization and no habituation after repeated stimulation. (Figure 3-4, Figure 3-5f). The defects in *osm-6(p811)* could be rescued by AWA-restricted expression of an *osm-6* cDNA (Figure 3-5e, Figure 3-6) suggesting that the increased sensitivity in the mutant is cell-autonomous to AWA.

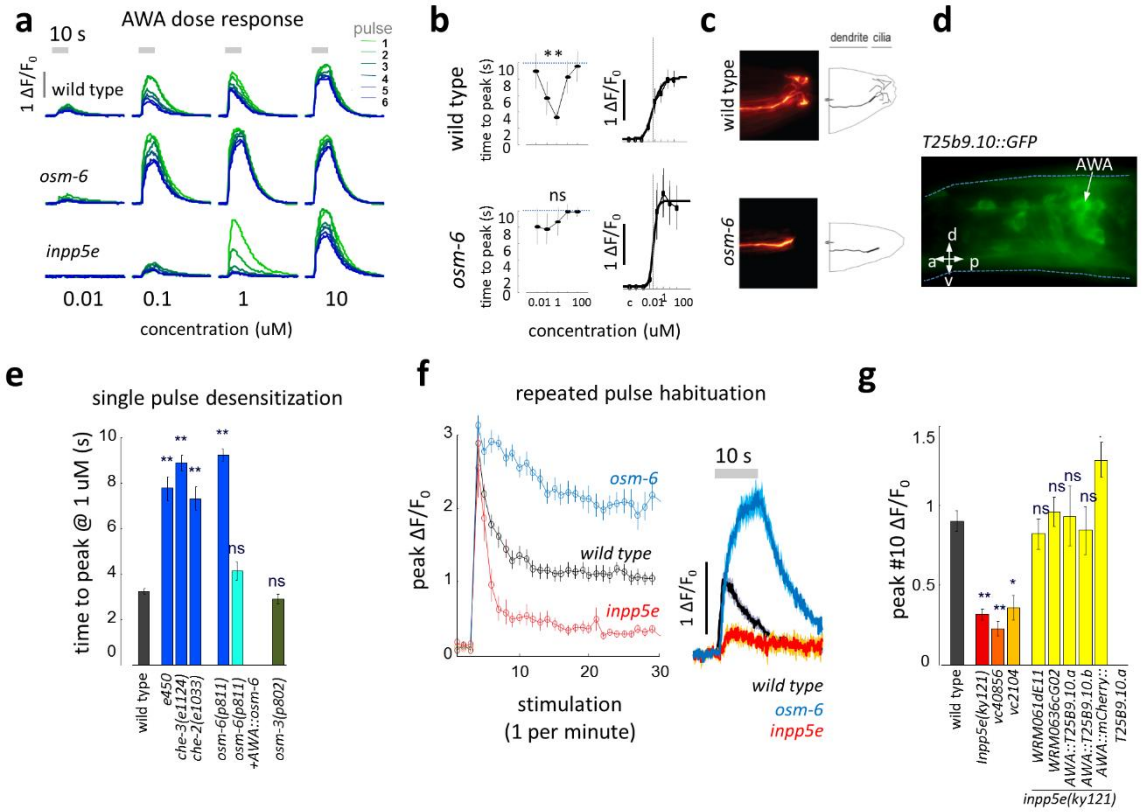

Figure 3-5 **Genetic modulators of AWA adaptation.**
(**a**) Mean AWA fluorescence during odor stimulation. AWA responses do not desensitize in *osm-6(p811)* mutant animals, and habituate exessively in *inpp5e*(*ky121)* mutant animals. (**b**) Mean peak AWA fluorescence and time to peak calculated from (a). Time to peak was shortest at intermediate concentrations in wild type but not *osm-6(p811)* animals (*P<.01; ns, not significant). Peak responses fitted to a Hill equation indicate a higher gain in *osm-6*, see methods. Error bars represent sd, n=10-21 animals x 6 pulses at each concentration) (**c**) Fluorescence z-stack projection of anterior tip of representative animals expressing GFP in AWA sensory neurons showing the sensory dendrite. Cilia are stunted in *osm-6(p811)* animals. (**d**) Fluorescence z-stack projection of the nerve ring of a representative animal expressing a *T25B9.10::gfp* fusion gene from a recombineered fosmid. Diffuse GFP expression is observed in many neurons. AWA was identified by mCherry expression from a separate transgene (mCherry not shown). (**e**) Time to peak of AWA fluorescence during stimulation at 1 uM diacetyl (**P<.001; ns, not significant versus wild type). Error bars represent s.e.m. n = 5-20 animals, 1 pulse each. (**f**) Mean peak AWA fluorescence during repeated stimulation for 10 s every 60 s at 1 uM diacetyl. Traces at right are mean AWA fluorescence during stimulation #30. Error bars and shading represent s.e.m. n = 5-12 animals. (**g**) Peak AWA fluorescence quantified during stimulation #10 is reduced in three alleles of *T25B9.10 (inpp5e)*. Rescue was achieved by fosmid transgenes that encompass *T25B9.10* or by expressing *T25B9.10* cDNA in AWA. (**P<.0001; *P<.001 versus wild type). n = 7-38 animals, 1 pulse each.

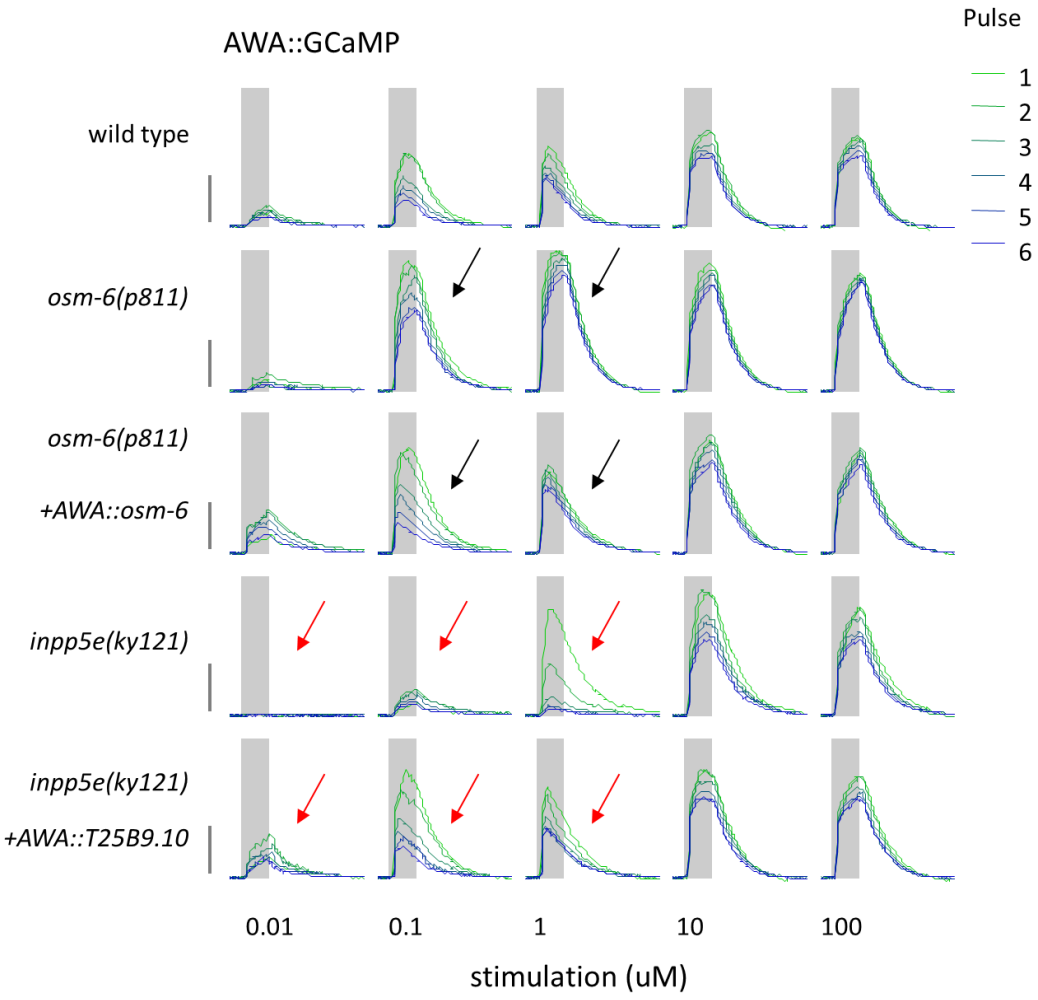

Figure 3-6 **Rescue of AWA fluorescence dynamics.**
Traces are mean AWA fluorescence during odor stimulation. Gray shading indicates odor stimulus. Desensitization was rescued in *osm-6(p811)* mutants by expressing *osm-6* cDNA in AWA (black arrows). Sensitivity at low diacetyl concentrations and normal habituation were restored in *inpp5e(ky121)* mutants by expressing *mCherry::T25B9.10a* cDNA in AWA (red arrows).

Phospholipid signaling regulates AWA desensitization

To find novel molecular regulators of AWA adaptation, we tested additional mutants with defects in chemotaxis to AWA sensed odors (Roayaie, Bargmann, unpublished results). We observed that calcium responses to diacetyl were weaker at low concentrations and desensitized more quickly upon repeated stimulation in *ky121* mutants than in wild type (Figure 3-5a,f,g). We mapped this phenotype to a missense mutation in the predicted Phosphoinositol-5-Phosphatase (INPP5) *T25B9.10*. Two independent predicted null mutations of *T25B9.10* had AWA calcium defects similar to *ky121*, indicating that this phenotype likely represents a complete loss of gene function (Figure 3-5a). AWA response magnitude was rescued by wild type transgenes including *T25B9.10* on a 37 kb fosmid (WRM061dE11) that was expressed in AWA and many other neurons (Figure 3-5d) or by AWA-restricted expression of *T25B9.10a::mCherry* cDNA (Figure 3-5a, Figure 3-6).

The *T25B9.10* locus encodes three predicted isoforms (a-c) generated by alternative splicing of the predicted first exons. Reverse transcription PCR identified two cDNAs *T25B9.10a*(short) and *T25B9.10b*(long) that were both sufficient to rescue the adaptation phenotype cell specifically in AWA (Figure 3-5g) suggesting that *T25B9.10* acts cell autonomously in AWA to maintain odor sensitivity at low stimulation regimes. Loss of function in *T25B9.10* also disrupted signal transduction in ASH sensory neurons, which have a bi-phasic response to 1M glycerol consisting of a transient increase in calcium during glycerol stimulation and a second peak upon odor removal (Chronis et al., 2007). The *ky121* allele caused a 75% reduction in ASH magnitude of the initial response, but did not reduce the second peak (Figure A-0-4).

The closest human homolog of *T25B9.10* INPP5E localizes to and stabilizes primary cilia. Mutations in this gene can cause Joubert syndrome, a ciliopathy affecting midbrain development (Bielas et al., 2009; Jacoby et al., 2009). We detected diffuse cytoplasmic fluorescence of *T25B9.10a::mCherry* and a genomic *T25B9.10::GFP* fusion, so cilia localization may not be preserved across species (Figure 3-5d and data not shown).

The INPP5 class of enzymes removes the 5' phosphate of specific phospholipid substrates that act as targeting signals for intracellular localization and trafficking (Bae et al., 2009; Conduit et al., 2012). For, example, acute depletion of phosphatidylinositol 4,5-bisphosphate by ectopic membrane recruitment of a 5-phosphatase domain in HEK293 cells disrupted endocytosis of angiotensin II, type 2C serotonin and b2 adrenergic receptors (Toth et al., 2012).Therefore, *T25B9.10* might regulate sensitivity via a role in odorant receptor trafficking. The diacetyl receptor ODR-10::GFP is distributed evenly in wild type cilia but had a tendency to accumulate in patches at the end of ciliary branches in *ky121* animals (Figure 3-7). *C. elegans* INPP5 may act in AWA to increase sensitivity at low odor concentrations and reduce habituation by affecting odorant receptor localization or cilium structure in a subtle way.

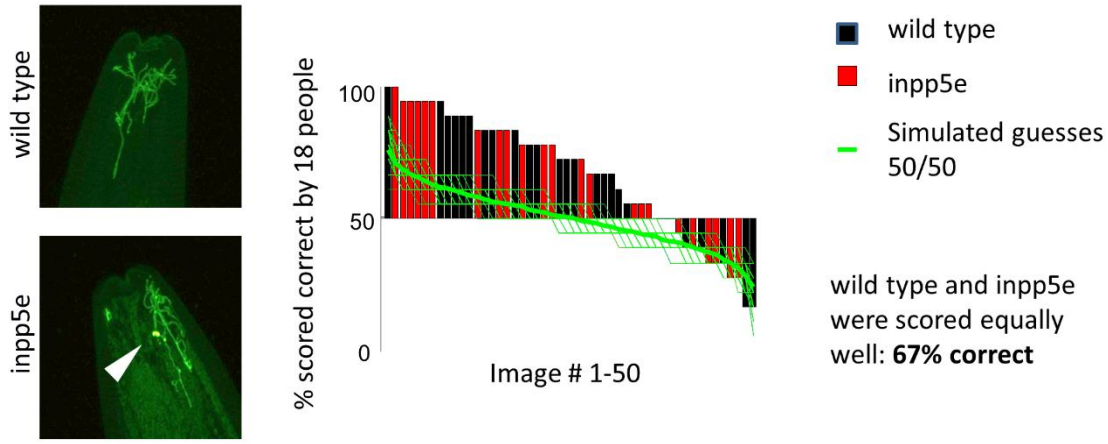

Figure 3-7 ***inpp5e* affects the distribution of the diacetyl receptor ODR-10.**
(Left) fluorescence z-stack projection of anterior tip of representative animals showing ODR-10::GFP localization to AWA cilia. Fluorescence is evenly distributed in cilia of wild type animals. Fluorescent patches (white arrowhead) occur in *inpp5e(ky121)* animals. (Right) 50 z-stack projections were scored by 18 people who were asked to match images to the wild type or mutant fluorescence pattern (see methods). Bars represent the percentage of correct calls for each image. Green lines indicate scoring distributions for 100 simulated rounds of 50 random guesses (thin lines) and the mean for these 100 rounds (thick line).

Interneuron responses to diacetyl pulses

The neurites of the AIA interneurons responded to diacetyl pulses from 1 nM to 100 uM with transient calcium increases (Figure 3-8a). Unlike AWA responses, which were 100% reliable, AIA occasionally failed to respond to individual odor pulses. AIA responses were highly sensitive, with a median EC50 of 7 nM. Unlike AWA, AIA peak responses were only weakly dose dependent: they saturated at ~100 nM diacetyl, and fell sharply at 100uM (Figure 3-8a,b). Desensitization within 10 s pulses was also highly uniform across concentrations so that AIA had a characteristic odor response shape. The peak response to repeated pulses at the same concentration of diacetyl decreased weakly after the first pulse and were stable thereafter (Figure 3-8a,b), unlike AWA responses that could be suppressed by 50% or more at certain concentrations. Together, these results suggest that the diacetyl signals in AIA are relatively uniform whereas responses in AWA are highly sensitive to odor concentration and history.

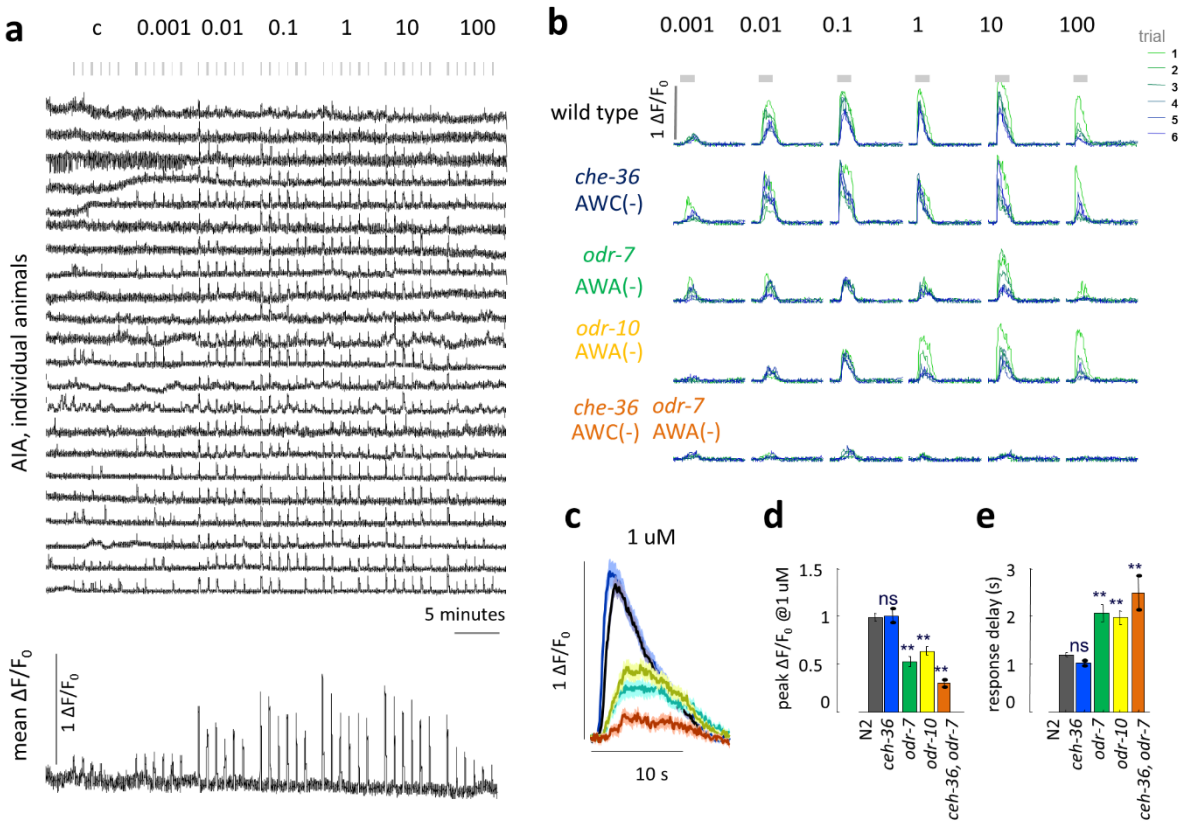

Figure 3-8 **AIA integrates input from AWA and other neurons.**
(**a**) Individual animal (top) and mean (bottom) AIA neurite fluorescence during dose response experiment. Each stimulus is presented six times for 10 s separated by 60 s, additional 60 s between concentration blocks. (**b**) Mean AIA neurite fluorescence per odor pulse, six repeats at each concentration are superimposed. *ceh-36(ky640)* and *odr-7(ky4)* are transcription factor mutants affecting AWC and AWA developmental cell fate. (**c**) Mean AIA neurite fluorescence during 1 uM diacetyl stimulation, shading represents s.e.m. n = 54-144 responses from 9-24 animals per genotype. (**d,e**) Peak AIA neurite fluorescence (d) and delay to respond (e) during 1 uM diacetyl stimulation. Delay is the time from odor pulse begin until fluorescence levels exceed 2 standard deviations of baseline fluorescence (**P<.0001; ns, not significant versus wild type).

AIA responses reflect AWA-dependent and AWA-independent diacetyl signals

To identify the sensory origin of AIA diacetyl responses, we examined mutant animals. *odr-7(ky4)* and *odr-10(ky32)* mutants with defective AWA neurons had sensitive AIA responses to diacetyl, but these responses were reduced in magnitude and altered in their dynamics compared to wild type animals (Figure 3-8b-e).

The AWC neurons have previously been shown to support diacetyl chemotaxis at high concentrations (Chou et al., 2001). A *ceh-36(ky646)* mutation results in developmental loss of the AWC and ASEL neurons (Koga and Ohshima, 2004). This mutant had near-normal AIA calcium responses to diacetyl (Figure 3-8b-e), but c*eh-36(ky646) odr-7(ky4)* double mutant animals had only 10% of the wild type response to diacetyl (Figure 3-8d). This suggests that the second sensory neuron that senses diacetyl could be AWC or ASEL

The AWC neurons express the vesicular glutamate transporter *eat-4*, which supports their synaptic response. Like *ceh-36*, *eat-4* mutations had little effect on AIA responses to diacetyl, but *eat-4(ky4); odr-10(ky32)* double mutants were severely defective across the concentration range (Figure 3-9). A comparable interaction was observed with *osm-6*. We conclude that AWA is a major source of AIA diacetyl responses but is supported by one or more additional sensory neuron(s) affected by *ceh-36, eat-4* and *osm-6*.

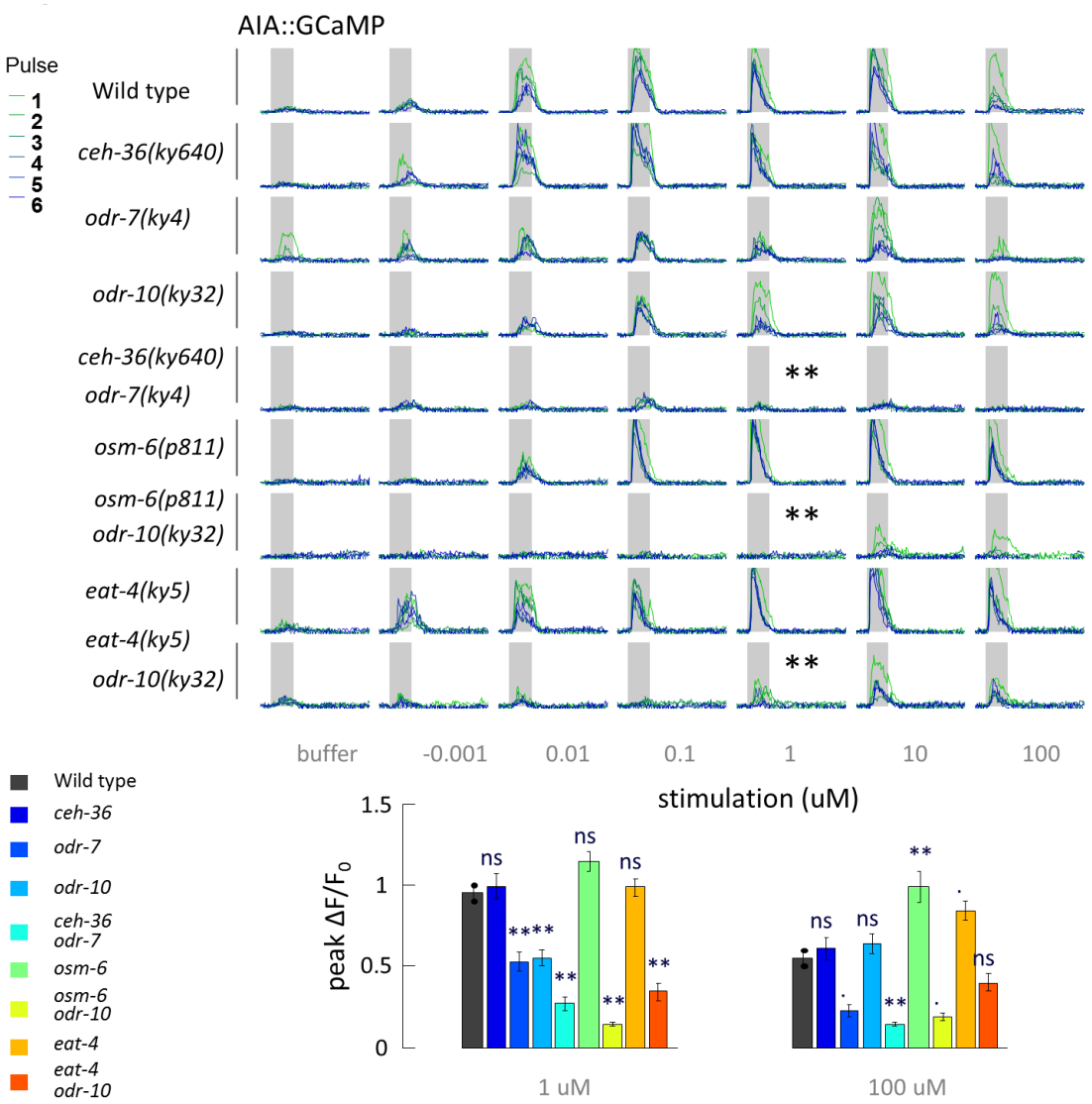

Figure 3-9 **Parallel transmission of diacetyl signals to AIA.**
AIA receives diacetyl signals in parallel via *odr-10/odr-7* and *ceh-36/osm-6/eat-4.* (Top) Mean AIA neurite fluorescence during odor stimulation (gray shading). The vesicular glutamate transporter *eat-4* regulates AWC synaptic output. Top five rows are repeated from Figure 3-8. (Bottom) peak AIA neurite fluorescence. (**P<.0001; +P<.01; .P<.05; ns, not significant versus wild type).

Neural representation of fold-changes in odor concentration

To ask how AWA responds to smaller changes in odor concentration, we measured AWA calcium responses to twelve successive increases in diacetyl concentration from 0.01 to 1.58 uM. Each step represented an increase in odor concentration of 58% relative to the previous concentration (fold-change) and lasted one minute (Figure 3-10a). AWA responded to eight fold-change steps with an increase in calcium that returned to baseline within about 30 seconds. Above 0.64 uM diacetyl, AWA calcium responses became larger and adapted only partially within the 60 seconds before the next stimulation (Figure 3-10a,c).

AIA interneurons also responded with transient calcium increases to this series of odor steps (Figure 3-10b). Response dynamics in AIA were more similar between successive odor steps than in AWA (Figure 3-10d): AIA had a three-fold lower coefficient of variation than AWA for response magnitudes across the full range of odor concentrations (Figure 3-10e). Thus, response normalization in AIA extended fold-change detection across a wider range of concentrations compared to AWA (Figure 3-10a,b).

AIA responses to diacetyl fold changes were ODR-10 dependent (Figure 3-10b,d), even at concentrations at which AIA can respond to diacetyl from a baseline (Figure 3-9). This result indicates that AWA sensory neurons are sensitive to and necessary for the detection of 58% fold changes, whereas the other sensory neurons dependent on *ceh-36, eat-4,* and *osm-6* are insensitive in this stimulation regime.

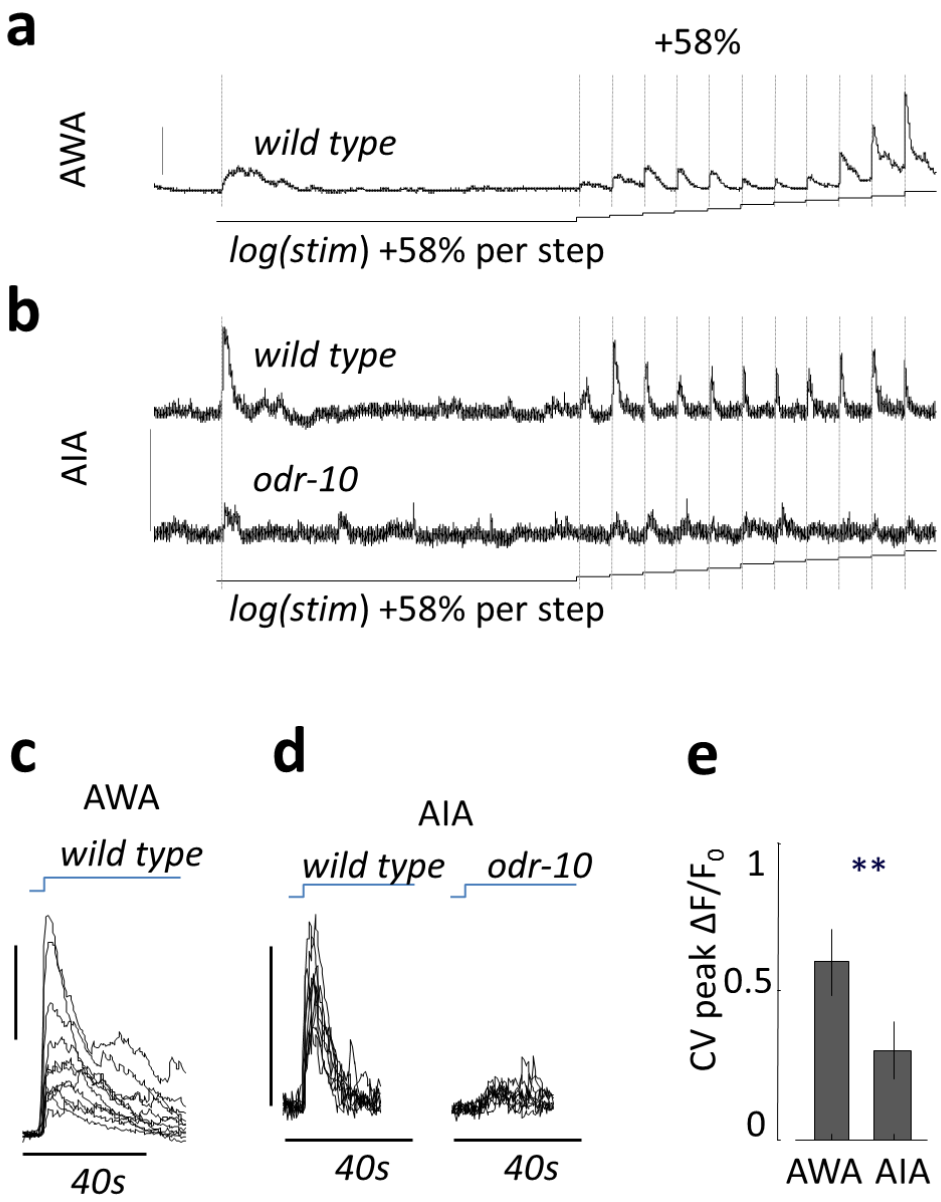

Figure 3-10 **AWA and AIA responses to fold-changes in odor concentration.**
(**a**) Mean AWA fluorescence during 12 successive 58% increases in odor concentration from 0.01 uM to 1.6 uM diacetyl. The first step from no odor to 0.01 uM is maintained for 10 minutes, subsequent steps are 1 minute each. Black line below trace indicates step timing. (**b**) AIA neurite fluorescence during fold-change stimulation. (**c,d**) Mean AWA (c) and AIA (d) fluorescence for each fold-change increases superimposed. (**e**) Coefficient of variance of peak fluorescence during fold-change stimulation was calculated for each animal as the standard deviation of 12 peak responses during fold-change stimulation divided by the mean peak response. Error bars represent s.e.m. n = 14-16 animals; **P<.0001

The altered dynamics of diacetyl responses in *osm-6(p811)* and *inpp5e(ky121)* mutants were associated with defects in the fold change response as well. AWA neurons of *osm-6(p811)* IFT mutant animals failed to return to baseline between odor pulses, and AWA neurons of *inpp5e(ky121)* mutants responded weakly across all concentrations (Figure 3-11).

To some extend, these defects were reversed by the AIA neuron which normalized the response to more closely resemble the wild type (Figure 3-11).

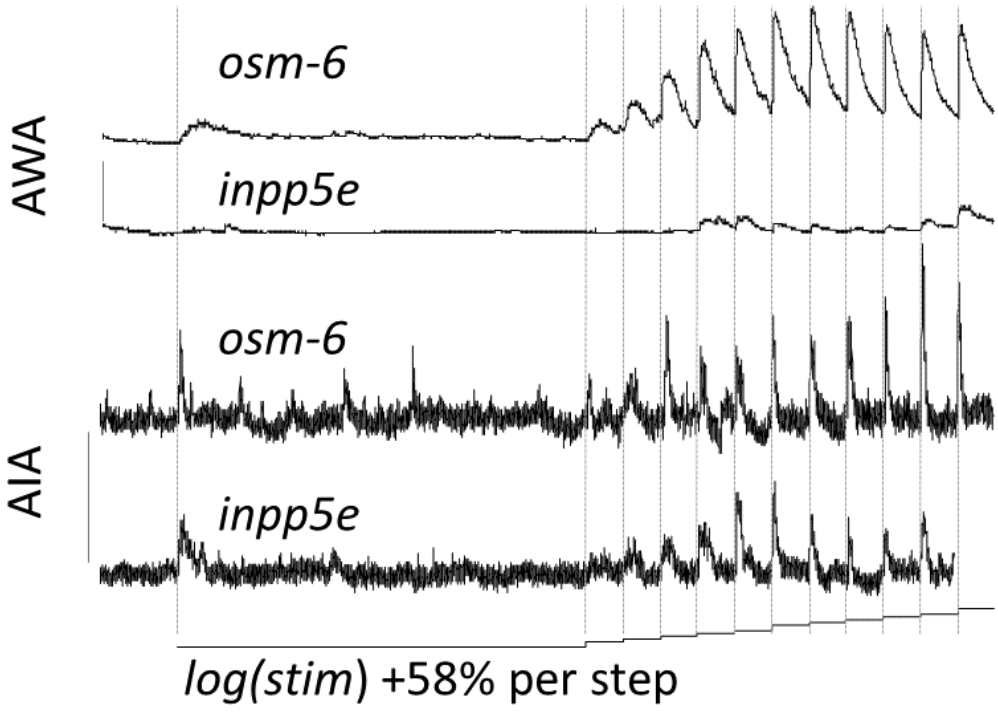

Figure 3-11 **AWA and AIA responses to fold-changes in *osm-6* and *inpp5e* mutants.** Mean AWA and AIA calcium responses in *osm-6(p811)* and *inpp5e(ky121)* mutant animals. Vertical bars in a-f indicate 1 $\Delta F/F_0$.

Behavior in microfluidic devices

Having established that AWA detects changes in odor concentration and relays this information to downstream interneurons, we wanted to relate these stimulus regimes to spatial orientation behavior. To define stimuli that trigger chemotaxis specifically through the AWA sensory neurons we monitored animal behavior in a microfluidic device during stimulation with diacetyl. Microfluidic devices provide a structured liquid environment to deliver precise quantities of chemicals to unrestrained animals. Animal behavior is recorded for post-hoc high content analysis of stereotyped patterns of locomotion with respect to odor encounters (Albrecht and Bargmann, 2011).

We first observed navigation in spatial odor gradients; in this configuration, animals control their sensory experience actively by moving within the gradient, as they do in chemotaxis on agar plates. Animals were tested in a sigmoidal gradient between selectable diacetyl concentrations (Figure 3-12a,b). Wild type animals distributed evenly throughout the arena when odor was uniform in the device, but readily migrated towards the peak when a gradient was present (Figure 3-12b). Individual animals occasionally descended the gradient but on average, animals remained near the peak of the gradient. In addition, animals spent more time at the device edge, irrespective of the presence or absence of odor (Figure 3-12b), a behavior that may result from mechanosensation at the walls of the device (Nam et al., 2013). To quantify chemotaxis performance we calculated a chemotactic index that reflects at each time point the distance of all worms to the top of the gradient. This index is -1 if all animals are at the center of the gradient, -1 if all animals are at the device edge, and near zero if all animals distribute randomly.

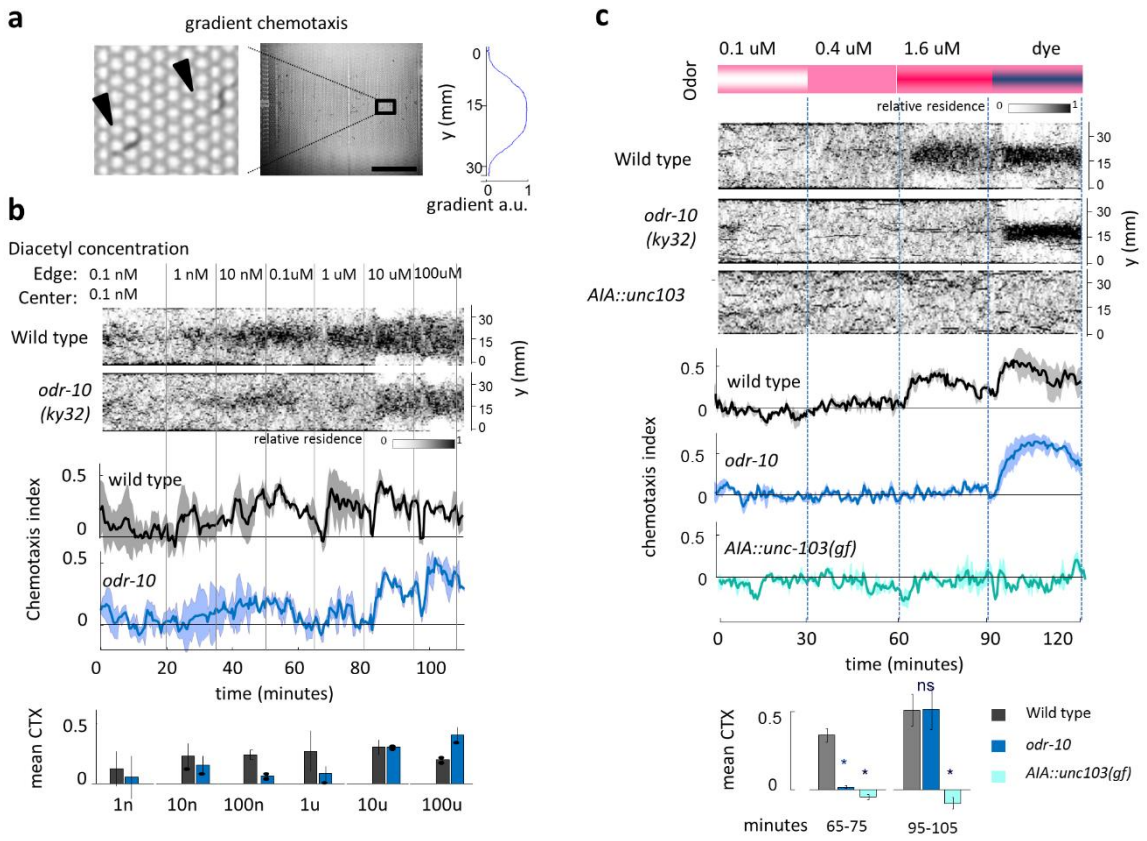

Figure 3-12 **Chemotaxis in microfluidic gradients.**
(**a**) (Middle) camera frame showing microfluidic device. Darker shading in the center is dye gradient. Scale bar = 10 mm. Stimulus reservoirs are connected to the device via a multi-channel valve to serve continuous flow and allow computer-controlled stimulus selection (not shown). (Left) magnified view showing two animals (black arrowheads) crawling through device post array. (Right) background subtracted dye intensity profile in arbitrary units. For example, a gradient from 0.1 uM to 1 uM has a dC/dx of 0.11 uM/mm on the approximately linear flanks and worms moving at .2 mm/sec experienced a rate of change in concentration (dC/dt) of up to .019 uM/sec (also see Figure 3-14). (**b**) (Top) gradient peak concentration of diacetyl was increased ten-fold every 15 minutes from 0.1 nM to 100 uM at the center whereas the edges were held constant at 0.1 nM, creating a sigmoidal diacetyl gradient. Animals are introduced into the center of the device and disperse evenly in the absence of a gradient. Wild type residence along the device's y-profile increased in the center in the presence of a gradient. (middle) Mean chemotaxis index representing the distance of all animals from the device center during 2 s time bins. Shading represents s.e.m. n = 2 sets of 20-30 animals per genotype. (bottom) Mean chemotaxis 5-15 minutes after exchanging gradient center concentration. Error bars: s.e.m. (**c**) Simplified chemotaxis assay using concentrations between 0.1 uM and 1.6 uM diacetyl. The edge is held constant at 0.4 uM diacetyl, the center is 0.1, 0.4 or 1.6 uM diacetyl or dye (0.5 mg mL^{-1} xylene cyanole). Data display as in (b), n = 2-3 sets of 20-30 animals per genotype; *P<.001; ns, not significant.

To define the range of diacetyl concentrations that can elicit chemotaxis, we varied the peak of the gradient from 1 nM to 100 uM, the range that AWA sensory neurons can detect (Larsch et al., 2013). Chemotaxis performance was relatively constant from 10 nm to 10 uM and dropped at 100 uM (Figure 3-12b). This dose response relationship is reminiscent of that found in plate assays where high odor concentrations also result in a drop in performance relative to lower concentrations (Bargmann et al., 1993). The chemotaxis response is therefore sensitive over three orders of magnitude in peak concentration and saturates above 10 uM.

The diacetyl receptor ODR-10 is required for diacetyl chemotaxis on plates and AWA calcium responses to diacetyl (Larsch et al., 2013; Sengupta et al., 1996). In the microfluidic gradient device, *odr-10(ky32)* animals did not chemotax if the diacetyl concentration at the peak of the gradient was below 10 uM (Figure 3-12b), indicating that this behavior required AWA sensory neurons. The ODR-10 receptor was not required for chemotaxis towards a control dye used at the end of the experiment (Figure 3-12c). Interestingly, *odr-10(ky32)* animals performed better than wild type animals at 100 uM (Figure 3-12b) suggesting that saturated AWA neurons interfere with chemotaxis performance mediated by lower affinity neurons. Based on these result, we generated a simplified assay for detection of gradients in the range of 1 uM diacetyl. *odr-10(ky32)* were defective in this assay (Figure 3-12c).

To test for a role of AIA in diacetyl-induced behavior, we examined a strain in which AIA was inactivated by expressing a constitutively active form of the ERG-like potassium

channel UNC-103 (Shinkai et al., 2011). These animals were severely defective in diacetyl chemotaxis in the microfluidic chamber (Figure 3-12c).

Pirouettes in response to fold-changes in odor concentration

In principle, turns could be modulated only when odor concentrations increase, only when odor concentrations decrease or under both conditions. Either mechanism alone is theoretically sufficient to bias a random walk. To distinguish among these possibilities, we measured turning rates in response to defined temporal upsteps and downsteps of diacetyl concentration in a microfluidic pulse device in which all animals experience the same stimulus history (Albrecht and Bargmann, 2011) (Figure 3-13).

Animals were pre-adapted to 0.1 uM diacetyl, then exposed to five 58% upsteps from 0.1 uM to 1 uM at an interval of 2 minutes, followed by five downsteps, visiting the same concentrations used during upsteps (Figure 3-13, Figure 3-14). Animals were then behaviorally classified for their instantaneous behavioral state (Albrecht and Bargmann, 2011). At steady state after pre-adaptation at 0.1 uM, 80% of animals were engaged in forward locomotion and 20% in reversals or omega turns (reorientations) (Figure 3-13a,b). Each odor upstep caused a transient suppression of turning before 30 seconds, and a subsequent complete recovery within the following 30 seconds (Figure 3-13a,b). However, successive downsteps had no effect on the turning rate (Figure 3-13a,b).

We next delivered six successive 58% upsteps in odor concentration from 0.1 uM to 1.58 uM at an interval of one minute between each step, followed by a larger downstep to 0.1 uM diacetyl. As before, each upstep transiently suppressed turning and the turning rate adapted to the baseline within each step (Figure 3-13c). Unlike the small

downsteps, a large step from 1.58 uM to 0.1 uM strongly increased turning with subsequent recovery over 5 minutes (Figure 3-13d).

Returning to the AWA diacetyl receptor ODR-10, we found that suppression of turns following upsteps was strongly reduced in *odr-10(ky32)* mutant animals (Figure 3-13c,d). By contrast, the increased turning following the large downstep was not reduced compared to wild type, suggesting that sensory inputs other than AWA contribute to this behavior. Hyperpolarizing AIA abolished the behavioral response to upsteps but not a large downstep (Figure 3-13c,d).

Figure 3-13 **Fold-change step responses in microfluidic gradients.**
(**a**) (Top) schematic of stimulus protocol. In pulse configuration, liquid flow exchanges stimulus fluids continuously throughout the device. Stimuli were delivered via a computer controlled multi-channel valve from up to eight liquid reservoirs. Half-time for stimulus switching was 20 s, matching the magnitude of dC/dt experienced during crawling in the microfluidic gradient device (see Figure 3-14). Concentration increased every 2 minutes by 58% per step from 0.1 to 1 uM diacetyl. (Bottom) instantaneous fraction of animals engaged in turning behavior during fold-change stimulation. Fraction of animals turning was lower 5-15 s after each upstep compared to baseline before first upstep in wild type animals (*P<.05). Fraction of animals was unchanged 5-15 s after downsteps compared to baseline before first downstep. Shading represents s.e.m. n = 4 sets of 20-30 animals per genotype x 2 repeats per set. (**b**) Percent change in the fraction of animals turning during all upsteps was larger for wild type animals compared to *odr-10(ky32)* mutant animals (*P<.001). Error bars represent s.e.m. (**c**) Instantaneous turning rate during 58% upsteps from 0.1 to 1.6 uM diacetyl lasting 1 minute each, followed by a large downstep from 1.6 to 0.1 uM diacetyl. Statistics as in (a), (*P<.001; '.' P<.05). n = 4 – 10 sets of 20-30 animals per genotype. (**d**) Percent change in the fraction of animals turning, statistics as in (b). Downstep response was quantified as the change in the mean fraction of animals turning during 10-70 seconds after the downstep compared to 60 seconds prior to the downstep.

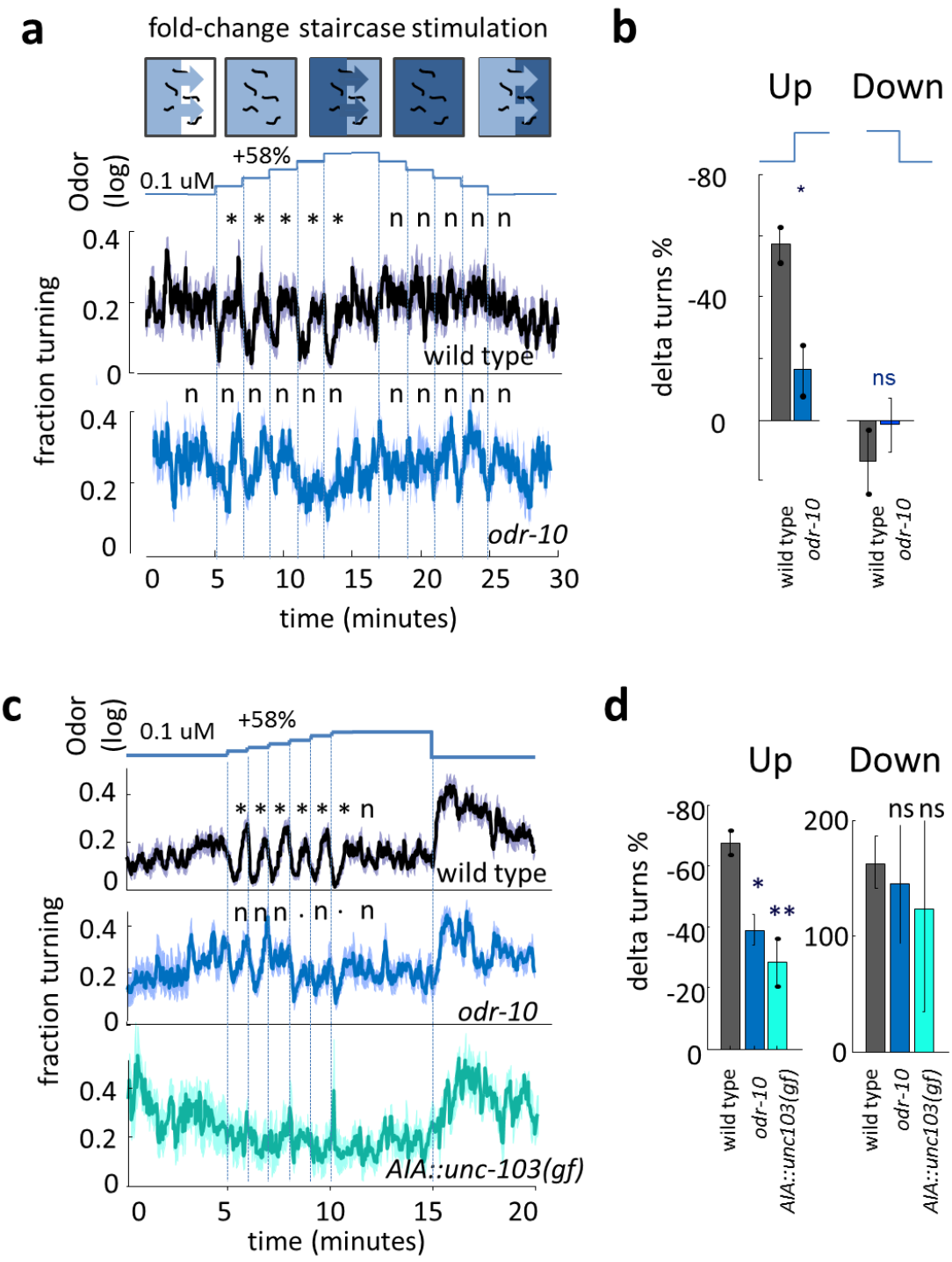
a
fold-change staircase stimulation
Odor (log)
0.1 uM
+58%
fraction turning
wild type
odr-10
time (minutes)
b
Up
Down
delta turns %
ns
wild type
odr-10
c
AIA::unc-103(gf)
d

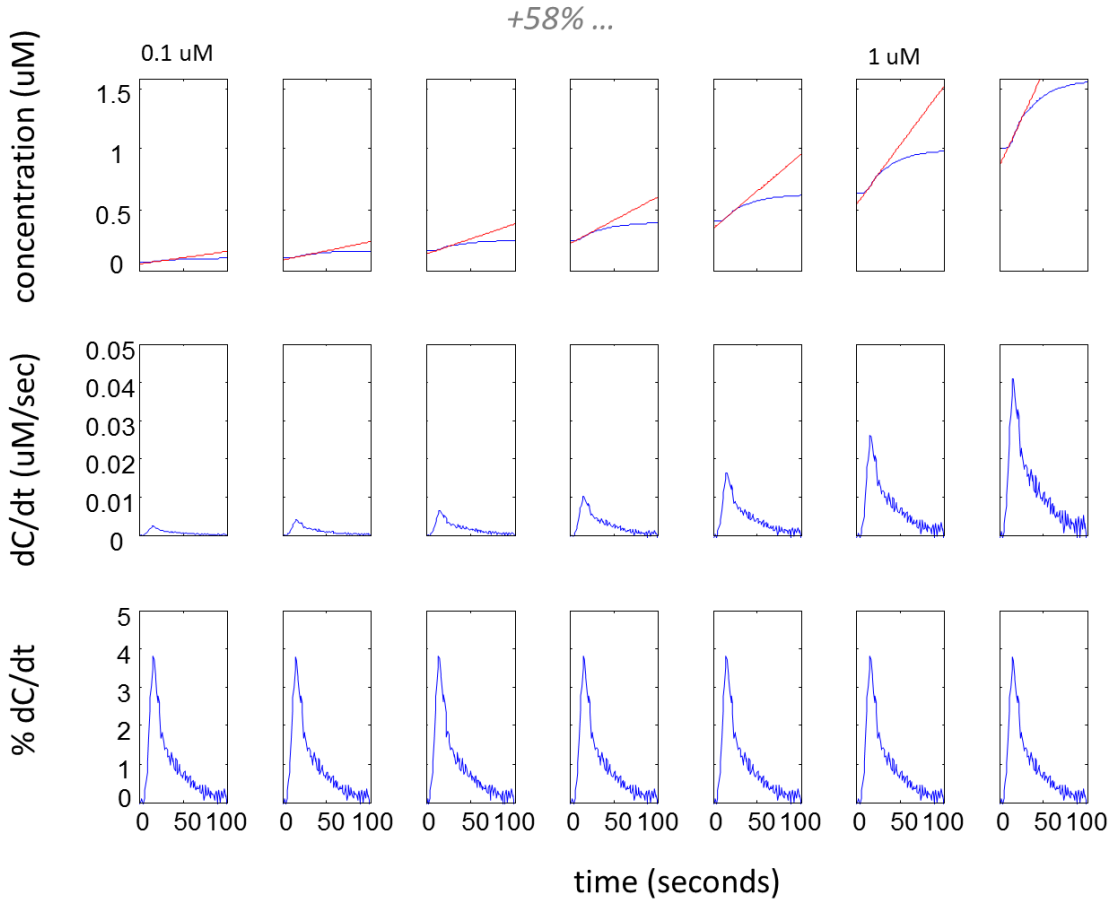

Figure 3-14 **Time-course of odor switching during fold-changes.**
To approximate odor concentration, we measured dye intensity over time at one concentration (0.5 mg mL^{-1} xylene cyanole) and extrapolated the resulting time course to seven 58% fold-changes from 0.1 uM to 1.6 uM diacetyl. The time to reach half maximal concentration during each step was 15-25 seconds, depending on the location in the microfluidic device and we used the mean for this extrapolation. (Top) absolute concentration (blue) and linear fit (red) during the first 10 seconds of stimulation. (Middle) change in concentration. (Bottom) change in concentration divided by starting concentration of each step. In summary, animals experience peak dC/dt of 4-40 nM/sec during the 7 58% fold-change steps, corresponding to a relative change of up to 4%/sec relative to the starting concentration of each step. This is similar to dC/dt experienced in the microfluidic gradient assay (Figure 3-12).

Optogenetic interrogation of the AWA-AIA connection

While odor stimulation is the most natural means of stimulating the chemotaxis circuit, overlapping odor recognition by multiple sensory neurons leaves ambiguity that can be addressed by orthogonal cell-specific activation experiments. Recently, Chrimson, a far red-shifted variant of Channelrhodopsin was described (Klapoetke et al., 2014) with excitation wavelength that overlaps minimally with G-CaMP, enabling recordings of calcium transients during cell specific light activation.

When Chrimson was co-expressed with G-CaMP in AWA sensory neurons, we observed strong calcium transients upon illumination with 605 nm light (Figure 3-15a-c). Perhaps surprisingly, Chrimson recapitulated the AWA calcium dynamics observed during odor stimulation: Transients varied with light duration and intensity (Figure 3-15b) and peak calcium was observed after five seconds even if the light stimulus was sustained for ten seconds (Figure 3-15c). AWA calcium transients with variable slopes could be generated by varying the rate of increase in light intensity during stimulation (Figure 3-15c).

By expressing Chrimson in AWA and G-CaMP in AIA, we were able to ask if AWA activation is sufficient to modulate calcium in AIA. Indeed, Chrimson excitation in AWA induced transients in AIA with a similar magnitude as diacetyl administration (Figure 3-15d,e).

To ask if AWA activation is sufficient to modulate turning behavior we excited Chrimson in AWA and quantified turning rates of animals on agar plates. AWA activation suppressed turning within 5 seconds. After 20 seconds, turning off the light elicited a rebound turning behavior (Figure 3-15e).

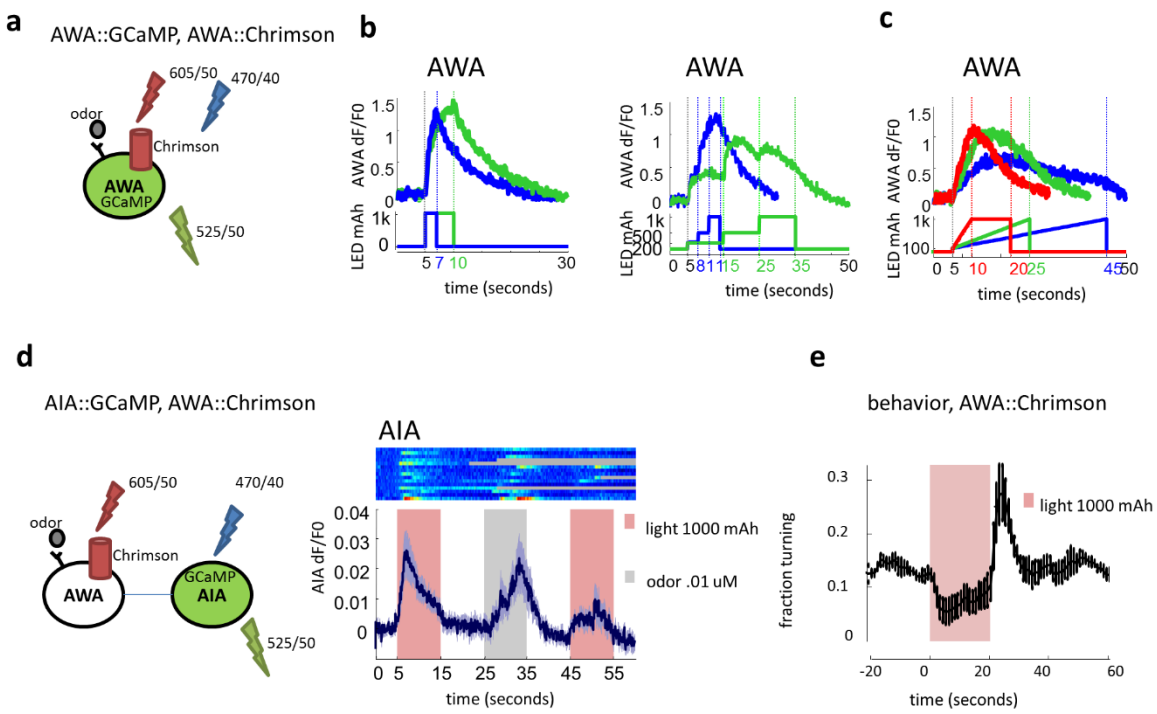

Figure 3-15 **Optogenetic probing of the AWA-AIA circuit.**
(**a**) Schematic of optogenetic probing of AWA: Chrimson is co-expressed with GCaMP in AWA. Red light excites Chrimson to depolarize AWA. Blue light excites GCaMP to emit green fluorescence. (**b**) (Left) mean AWA fluorescence during Chrimson stimulation for 2 or 5 seconds. (Right) Magnitude of AWA fluorescence is dependent on Chrimson stimulation intensity. (**c**) AWA fluorescence during Chrimson stimulation ramping to maximum within 10, 20 or 40 seconds. (**d**) Probing of signal transmission from AWA expressing Chrimson to AIA expressing GCaMP. 10 s Chrimson stimulation alternated with one 10 s pulse of diacetyl. Shading represents s.e.m. n = 15 animals. (**e**) Mean fraction of animals turning during 20 s Chrimson stimulation. Error bars represent s.e.m. n = 3 experiments, 15-20 animals each.

These results suggest that a single depolarization of AWA with Chrimson is sufficient both for transmission of an informative signal to AIA, and for regulation of turning behavior in a pattern that resembles wild type responses to diacetyl.

Agent-based model of diacetyl chemotaxis

The fold-change experiments suggest an asymmetric turning bias elicited by AWA stimulation: small increases suppress turning, but small decreases do not enhance turning. An open question is whether these changes are sufficient to explain accumulation in our microfluidic gradient assay. To explore this possibility, we implemented an agent based biased random walk model in NetLogo (Wilensky, 1999).

We defined a virtual gradient and agents that use a set of rules to control their movement that matched the spatial properties of odor and *C. elegans* locomotion in the microfluidic gradient assay (Figure 3-16a). Agents travelled in straight runs at a constant speed of 0.2 mm/sec and had a baseline turning rate of 20%. Turns were modeled as a 5 second period without locomotion, and subsequent heading was random. Turn probability was regulated by odor concentration as agents traversed a sigmoidal virtual odor gradient. The model was used to explore the effect of different modes of odor sensing on chemotaxis performance.

In a preliminary model, the initiation rate of turns p(turn) was regulated by absolute odor levels (no adaptation). In separate runs, increases in odor concentration increased or decreased turning respectively.

1a) $p(turn) = k * C$

(turns increase with odor concentration)

1b) $p(turn) = p(turn)_{baseline} * e^{-k*C}$

(turns decrease with odor concentration, in this case exponentially)

This model with modulation of turns by absolute odor concentrations did not exhibit any chemotaxis.

Building from the data obtained for AWA odor responses, we next modeled regulation of the turning rate by (absolute) changes in odor levels (the result of adaptation). To match our behavioral data using small 58% changes in odor concentration, turns were suppressed if dC/dt was positive. If dC/dt was negative, agents turned with baseline probability.

2) $p(turn) = p(turn)\_baseline * e^{-k*dC/dt}$ for dC/dt >0

$p(turn) = p(turn)\_baseline$ for dC/dt < 0

The choice to model p(turn) in with this particular function was made to reflect that turning rates asymptotically approach a low level for large dC/dt. In the range of 0.1 to 1 uM diacetyl, the response of turn suppression was similar during successive fold-changes (Figure 3-13). Therefore, we cannot determine the exact shape of the relationship of dC/dt and turning rate. For the purpose of this model, we chose k of the exponential decay model (equation 2) to suppress the baseline turning rate of 0.05 initiations per second by 75% in response to the first 58% fold-change from 0.1 to 0.158 uM representing a dC/dt of ~3 nM/sec[1].

k: ~500 [s / uM]

This model produced efficient chemotaxis in a virtual gradient (Figure 3-16b).

[1]The exact shape of the function relating p(turn) to dC/dt can be experimentally obtained by surveying turning responses to a wider range of different fold-change steps in diacetyl concentration but the main purpose of the model is at this point to show how different modes of odor sensing can produce qualitatively different chemotaxis behavior.

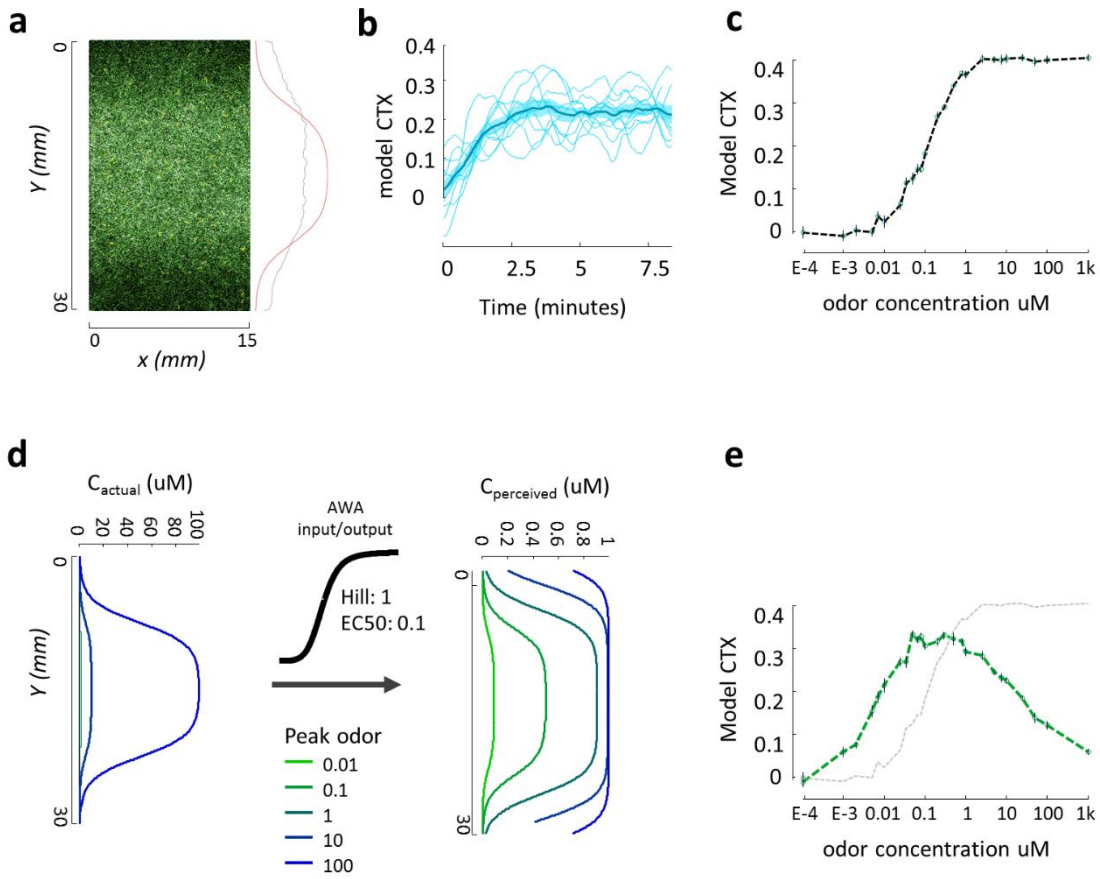

Figure 3-16 **Multi-agent model of chemotaxis.**
(**a**) Virtual gradient arena, showing relative residence of agents during 10000 simulation steps at 2 Hz. Lighter shading indicates more time spent. Red line: simulated odor gradient ranging from 0.001 – 0.1 uM diacetyl. gray line: histogram of relative residence. (**b**) Model chemotaxis over time for 10 individual simulations with 100 agents each (thin lines). Thick line indicates mean, shading represents s.e.m. Agents start at randomized locations. (**c**) Steady state model chemotaxis at different peak gradient diacetyl concentrations using absolute concentrations as the input to calculate dC/dt. Mean of 5 simulations per concentration, error bars: s.e.m. (**d**) Transformation of actual odor concentration into perceived concentration by the Hill function that describes AWA's odor to calcium input/output function. Gradient before and after transformation is shown for 5 different peak odor concentrations, low end of gradient is kept constant at 0.001 uM odor. (**e**) Model chemotaxis using transformed odor concentrations as the input to calculate dC/dt. Data in panel (c) is reproduced in gray for comparison.

By analogy to the microfluidic gradient, we calculated a chemotaxis index at each time point representing the distance of each agent from the top of the gradient. The agent chemotaxis index in the virtual gradient increased in a dose dependent manner and saturated at peak gradient concentrations of 1 uM (Figure 3-16c). In this simple model, the sensitivity (EC_{50}) of the chemotaxis response was solely determined by k, the factor scaling turn suppression at a given dC/dt. When concentrations were very high (e.g. 100 uM), dC/dt was also high and strongly suppressed turning in agents moving up the gradients, resulting in maximal chemotaxis performance.

These results show that suppression of turns in response to odor increases is sufficient for gradient climbing on the length scales of our experiment. On the other hand, this simplified model is inconsistent with our chemotaxis data in two ways. First, real chemotaxis performance was relatively constant over several orders of magnitude at intermediate concentrations and fell at higher concentrations. Second, fold-change stimuli indicated that both neural and behavioral responses reflected relative changes in diacetyl concentration rather than absolute dC/dt (Figure 3-10, Figure 3-13).

We therefore implemented a more sophisticated model of odor sensing that reflected sensitivity over the dynamic range of AWA sensory neurons. Instead of reading out actual odor concentration (C_a) at each agent's position, that concentration was filtered through a saturating nonlinearity to yield the perceived concentration (C_p) which was subsequently used to calculate dC/dt.

3) $$C_p = \frac{1}{1+\left(\frac{EC_{50}}{C_a}\right)^h}$$

EC_{50} and h were obtained from the experimentally measured AWA calcium responses to a wide range of diacetyl concentrations:

EC_{50} = 100 nM

h = 0.8

With this transformation, perceived odor concentrations were bounded between zero and one (Figure 3-16d) and became buffered around the EC_{50} concentration. We re-ran the virtual dose response gradient experiment. Now, chemotaxis performance in the gradient increased at low concentrations and decreased at high concentrations, resulting in a bell shaped dose-response relationship (Figure 3-16). Agent chemotaxis was maximal near the EC_{50} for AWA odor sensitivity because this is the steepest part of the AWA dose response curve for odor perception and therefore, perceived dC/dt is largest. At higher concentrations, the non-linearity is saturated and perceived dC/dt falls.

Further work is needed to include acute adaptive rescaling observed in AWA calcium responses to fold-changes into this model. This is expected to further broaden the range of concentrations where chemotaxis performance is constant at intermediate concentrations.

Discussion

High throughput Imaging

Imaging neural activity with low-magnification optics yielded substantial benefits in animal throughput, experiment duration and repeatable chemical stimulation compared to existing systems for high-magnification imaging of an individual restrained or freely-moving animal. We obtained wide-field recordings of activity in sensory neurons, and from interneurons whose calcium transients were restricted to their axons, despite reduced spatial resolution and fluorescent signal-to-noise ratio. For many applications, such as characterizing stochastic neural and behavioral responses, it should be beneficial to increase experimental throughput at the expense of image resolution.

Experimental reproducibility is often challenging for studies of animal behavior in which small variations in training, stimulus history, or assay conditions can substantially influence behavioral outcomes (Richter et al., 2009; Wahlsten et al., 2003). In our system, precisely-delivered chemical stimuli elicited predictable behavior probabilities and calcium responses: population-average responses adapted consistently over time at similar rates from one experiment to another, and individuals consistently responded strongly or weakly to repeated stimuli. Whereas *C. elegans* neural recordings generally have been made in naive animals, we found that sensory calcium responses in AWA were most variable during the first few stimuli, becoming more reproducible and stable after several pulses. Defining the stable response regimes for other neurons and sensors should facilitate characterization of their properties and comparisons of their responses across experimental conditions.

The magnitude and sensitivity of odor-evoked AWA calcium dynamics varied among isogenic animals. Possible sources of this variation include developmental or epigenetic variations between animals, effects of recent experience or modulatory state, variability associated with the GCaMP transgene, or stochastic effects. These observations emphasize the need to examine neural and behavioral responses in many individual animals under repeatable stimulation.

Continuing improvements in optical components, software, and neural sensors will likely further increase the experimental throughput of wide-field neural imaging. Cameras are already available with larger sensors for increased field-of-view, as are objectives with higher NA. Improvements to analysis software, particularly for tracking many freely-moving animals, will be required for full automation of data analysis.

We present here several examples of experiments enabled or accelerated by wide-field neural imaging. Mapping neural activity during probabilistic behaviors, such as decision-making in complex or conflicting sensory environments, will require large numbers of neural recordings, as will genetic and pharmacological analyses of neural response dynamics. Long-term recordings should enable the continuous study of neural and behavioral plasticity, adaptation, and learning over hours. We anticipate this reliable and efficient system will aid in the detection of subtle neural phenotypes, the study of neural dynamics, and the generation of data for systems modeling of brain circuitry.

Roles for sensory adaptation during spatial orientation

During navigation, organisms control their movement through space based on information extracted from the environment. Key to understanding this sensory-motor transformation is to define what information is extracted and how the behavioral goal is achieved by regulated, specific motor patterns. To dissect the mechanisms underlying orientation in chemical gradients, we surveyed neuronal and behavioral responses in *C. elegans* during odor stimulation. Our results show that precise adaptation sensitizes the chemotaxis response to positive changes in diacetyl concentrations rather than absolute levels. At the behavioral level, small upsteps in odor concentration transiently suppressed reorientation behavior whereas small downsteps had no effect, providing a mechanism for indirect orientation in a stimulus gradient.

The biased random walk model is currently the predominant formalization of *C. elegans* chemotaxis. It postulates that animals detect dC/dt to regulate the frequency of turns that are randomly oriented to prolong runs towards higher concentrations of attractants bias net movement up the gradient. Detection of dC/dt rather than absolute odor concentration requires adaptation at some level in the chemotaxis circuit. A second reason chemotaxis requires adaptation is response sensitivity over a wide input range, a dilemma sometimes called the 'sensitivity paradox' (Sourjik, 2004). The challenge is that for example *E. coli* responds to a 0.2% change in receptor occupancy with a ~20% change in tumbling frequency, a 100x signal amplification that is maintained over five orders of magnitude in stimulus concentration. A system with 100x amplification would saturate at 1% input signal intensity and thus behave no different from a system without amplification but higher sensitivity unless adaptation keeps signaling within the dynamic range (Sourjik, 2004). *C. elegans* faces a similar challenge because animals can

chemotax to certain odors such as diacetyl over seven orders of magnidute in concentration, suggesting active and acute adaptation mechanisms for maintaining sensitivity (Bargmann et al., 1993).

Desensitization of sensory responses could provide a mechanism to differentiate inputs over a wide range of stimulus intensities without saturation. Alternatively, desensitization may also reflect other cellular properties such as novelty detection (Wark et al., 2007) acute protection from overstimulation, sharpening of response dynamics for efficient downstream processing or restricting cellular responses to a limited number of stimulus encounters to yield a switch like behavior. However, the functional consequences of sensory desensitization in *C. elegans* have not been explored systematically.

Stimulus induced responses in several classes of *C. elegans* sensory neurons besides AWA are transient. For example, calcium levels in ASEL and ASH sensory neurons rise transiently in response to upsteps in salt and copper concentrations, respectively, and then return to baseline or a lower sustained level, depending on the stimulus concentration (Hilliard et al., 2004; Suzuki et al., 2008). Interestingly, desensitization is widespread but not a universal feature of *C. elegans* chemosensory neurons. For example, AWC and ASER sensory neurons respond to certain odors and salts, respectively, with little or no apparent adaptation for several minutes to hours (Chalasani et al., 2007; Suzuki et al., 2008). These neurons exhibit suppressed calcium levels upon stimulation. Generally, desensitization is more common in neurons that increase calcium levels upon stimulation: ADF (Qin et al., 2013), ADL (Jang et al., 2012), BAG (Zimmer et al., 2009) and AWB (Yoshida et al., 2012) belong in this group of ON neurons together with AWA and ASH. URX (Zimmer et al., 2009), ASK (Macosko et al., 2009) and AQR and PQR (Busch et al., 2012) are OFF neurons like AWC and ASER that do not

desensitize. One notable exception to this correlation are calcium responses in AFD sensory neurons to changes in carbon dioxide concentration. Like AWC, AFD exhibits suppressed calcium levels upon stimulation and an overshoot above baseline after stimulus removal but, unlike responses in AWC, AFD suppression is transient and returns to baseline within 60 seconds (Bretscher et al., 2011).

This functional classification of sensory neurons may have implications for the sensitivity in detecting their respective ligands. Stimuli that are detected by non-adapting OFF-polarity sensory neurons may still be differentiated by the downstream circuitry, but for any given signal transduction pathway, the sensitivity is limited by the least sensitive component; the system cannot be more sensitive than its sensor. Other sensory systems such as *Drosophila* olfaction increase overall sensitivity above the level of single receptor neurons by convergence of hundreds of sensory neurons onto fewer projection neurons (Bargmann, 2006b; Wilson, 2013) but this is not possible in *C. elegans* where many stimuli are detected by only a single pair of sensory neurons. By this argument, adaptation is most effective at the sensory level to increase sensitivity of a neural circuit. Within the sensory neuron, adaptation would be most effective at the receptor level. For example, adaptation in E. coli during chemotaxis involves desensitizing receptor molecules via methylation (Sourjik, 2004).

At the sensory level, we have shown that AWA sensory neurons are transiently activated by increases in diacetyl concentration. Odor-evoked calcium transients revealed two distinct kinds of changes to AWA sensitivity on different time scales: within and between stimulations. Generally, naïve animals had the largest response magnitudes to odor stimulation, analogous to high sensitivity in the visual system after dark adaptation (Kandel, 2013). Repeated stimulation at a fixed frequency reduced response magnitudes

to individual odor pulses over the course of minutes, and this habituation recovered on a similar time scale in the absence of stimulation or during stimulation at a lower frequency. In addition, sustained stimulation at certain concentrations reduced the response magnitude within each odor pulse. In wild type animals, we observed this desensitization at concentrations between 0.1 and 10 uM diacetyl, but not at higher or lower concentrations.

A desensitizing response during continuous stimulation indicates that two processes act antagonistically. One process is excitatory, acting to increase the response; the other is inhibitory, acting to decrease the response. Our recordings constitute a combined readout of the balance of both processes over a range of diacetyl concentrations. Our data is consistent with a model in which excitation increases gradually with diacetyl concentration between 0.01 and 100 uM, inhibition is triggered above 0.1 uM and antagonizes responses up to 10 uM, and inhibition is saturated above 10 uM. The rate of desensitization reflects the ratio of excitation to inhibition at specific diacetyl concentrations, not response magnitude. This dissociation between response magnitude and response decay suggests that the two phenomena are separately regulated by distinct physiological processes.

Importantly, desensitization endows AWA with the ability to respond repeatedly to successive increases in odor concentration. We detected characteristics of fold change detection (FCD) in AWA calcium transients as defined by concentration-invariant response dynamics in response to 58% fold-changes in diacetyl concentration and a saturation point of this process just below 1 uM diacetyl concentration.

Together, these results reveal a complex set of concentration dependent dynamics of diacetyl induced AWA calcium transients. To relate absolute concentrations delivered in our microfluidic assays to odor dilutions applied in classical agar plate chemotaxis assays, we can use the *odr-10(ky32)* mutant for calibration. *odr-10* mutant animals are defective in diacetyl plate chemotaxis at dilutions up to 1:1000[2]. During gradient chemotaxis in the microfluidic device, we found that *odr-10* mutant animals were defective up to 1 uM diacetyl, serving as an approximate equivalent between the two assays. Therefore, it is realistic to assume that desensitization and habituation reflect dynamic responses to behaviorally relevant diacetyl concentrations.

Adaptation mutants reveal unexpected roles for conserved genes

Two genetic lesions affected the dynamics of adaptation in opposite ways. These observations indicate that odor-evoked AWA response dynamics reflect physiologically regulated processes, and suggest that the balance of excitation and inhibition is actively maintained in wild type animals.

Animals mutant in intraflagellar transport (IFT) neither desensitized nor habituated to diacetyl, and had stronger AWA diacetyl responses than wild type animals. Mechanistically, it is unclear how mutations in IFT genes affect AWA calcium responses. Possibilities include direct and indirect effects of IFT. For example, IFT may be directly required for desensitization and habituation by translocating signaling molecules, by analogy with light dependent movement of Arrestin in the *Drosophila* visual system (Montell, 2012). To address this particular hypothesis, we tested *arr-1* mutants, the only

[2] In a typical chemotaxis plate assay, 1 uL of this dilution is applied to a 10 cm agar plate containing approximately 10 mL agar. The odor is then left to diffuse under the lid of the plate for a few minutes before animals are introduced and allowed to chemotax in the gradient that has formed in the meantime. Quantifying the exact distribution of the gradient is challenging.

known arrestin homolog in *C. elegans,* but found no AWA desensitization defect (data not shown). Nonetheless, IFT could act by moving other signaling molecules. In addition, we have tried to inhibit IFT via bath application of a small molecule inhibitor of dynein that can acutely stall retrograde IFT without immediately disrupting primary cilium morphology in cell culture (Firestone et al., 2012) but pilot experiments did not yield an effect (data not shown). A more general formulation could be that IFT transports a cytoplasmic protein into cilia that is needed for habituation or adaptation, but not actively transported. An example might be calmodulin, which acts in vertebrate olfactory desensitization (Kurahashi and Menini, 1997; Munger, 2001).

Alternatively, the adaptation defect may be a structural effect of stunted cilia that bring the diacetyl receptor and associated signaling molecules into abnormal physical interactions. Wild-type AWA cilia are highly branched and a large proportion of their surface is buried in a surrounding sheath cell (Doroquez et al., 2014). It is currently unclear where ligands interact with odorant receptors within this structure. One possibility is that odor signaling occurs at the exposed cilium shaft that may be largely intact in IFT mutants, and that cilium branches are partially or fully insulated from odor exposure and may therefore serve as regulatory domains. Currently, no data exists to support or refute this model. Our results, perhaps surprisingly, suggest that cilia may serve a net inhibitory function in AWA rather than mediating primary transduction of odor signaling.

AWA sensory neurons are specialized to detect small increases in diacetyl concentration

Based on behavioral results in microfluidic and agar plate gradients, we anticipated that AWA sensory neurons and the diacetyl receptor *odr-10* would be required for both neural circuit responses and behavioral responses to diacetyl concentrations below 1 uM, but this was not strictly true. *odr-10(ky32)* AIA responses were similarly sensitive to diacetyl pulses as wild type animals, albeit with slower dynamics and lower response magnitudes, and we showed that this residual response is transmitted from other sensory neurons. Presumably, these other neurons also mediate the behavioral response to large step changes in diacetyl concentration, which are also AWA-independent. However, no other neuron compensated for the loss of *odr-10* function for responses of AIA interneurons or for responses at the behavioral level to fold-change upsteps in diacetyl concentration, indicating that only AWA was sensitive in this regime.

Together, these results suggest that AWA is a specialized detector of small changes in diacetyl concentration, well suited to instruct downstream circuitry to regulate turns during chemotaxis. Over a certain range, AWA responses exhibit characteristics of FCD. Further experiments are needed to determine if AWA responses truly reflect absolute or relative dC/dt. A pilot survey suggests that AWA response magnitudes to diacetyl fold-changes generally depend on the magnitude of the fold-change but can be superimposed on history- and concentration-dependent calcium fluctuations (Figure A-0-5).

AIA interneurons perform a high gain, low threshold readout of AWA activity

To understand which aspects of AWA dynamics are transmitted to other neurons as part of the sensory-motor transformation underlying chemotaxis, we extended calcium imaging to AIA interneurons. The wiring diagram shows a gap junction between AWA and AIA, and AIA neurites can respond to diacetyl with the same direction as AWA. In isotropic environments, loss of AIA neurons led to more turning behavior, suggesting that AIA neurons normally act to suppress turning (Chalasani et al., 2007). Therefore, in a simple model, activity could be transmitted from AWA to an interneuron AIA upon diacetyl detection and transiently suppress turning behavior. Consistent with this model, we found that AIA was highly sensitive to increases in diacetyl concentration.

Despite the direct electrical coupling with AWA, AIA responses did not merely mirror AWA. Instead, AIA resembled a high gain readout of AWA activity that converted the richness of AWA dynamics observed across diacetyl concentrations and during repeated stimulation into uniform responses. AIA responses were also largely insensitive to perturbation of AWA dynamics caused by IFT and *inpp5e* mutants. These properties may arise from active cell-intrinsic amplification of inputs to AIA, for example by voltage activated currents. Our results also predict efficient inactivation mechanisms in AIA that can terminate calcium transients during ongoing signaling from AWA, because AIA responses desensitized within about ten seconds even at high odor concentrations and during sustained AWA depolarization using Chrimson. Together, AWA and AIA compute diacetyl dC/dt with high sensitivity and large response gain, which resembles a two stage process of adaptation and subsequent amplification.

Analogies in architectures for chemotaxis

Our behavioral analysis and neural imaging showed that small changes in diacetyl concentrations are only sensed and acted upon when diacetyl concentrations rise. Turning frequency was suppressed during increases in odor concentration but unaffected by decreases in odor concentration. This is highly similar to the bacterial biased random walk strategy, where turning frequency of single cells is suppressed upon increases in attractant concentration but unchanged upon decreases (Berg and Brown, 1972).

In addition, signal processing in these two systems bears some resemblance: In *E. coli*, the 'sensitivity paradox' is resolved in part by a high-gain response of the motor proteins that mediate runs versus tumbles to CheY, the output of receptor signaling (Cluzel, 2000; Sourjik, 2004). In *C. elegans*, AIA appears to serve a similar function by amplifying sensory AWA inputs into uniform responses that likely feed into motor control circuits to suppress turning. Consistent with this model, optogenetic activation of AIA suppresses turns (Navin Pokala, unpublished results).

In both *E. coli* chemotaxis and *C. elegans* diacetyl chemotaxis, stimulation of turning above baseline can be observed in response to decreases in concentration once the step size becomes sufficiently large. In the case of *E. coli*, it was argued that its swim speed is barely sufficient to escape the drag of the surrounding media and hence it would be unlikely to experience such sudden changes in odor concentration (Berg, 2004). Odor distributions in natural habitats of *C. elegans* are not known and it remains to be seen which modes of behavioral response are accessed during locomotion.

Chrimson stimulation showed that AWA is sufficient to trigger both suppression and enhancement of turning behavior. However, under natural odor stimulation, AWA is redundant with other neurons that enhance turning after diacetyl removal.

Alternative behavioral strategies during chemotaxis

The strong phenotype of AIA hyperpolarization in the microfluidic assay is in contrast to its minor effect on diacetyl chemotaxis on agar plates (Shinkai et al., 2011) (and our own unpublished results). This discrepancy may indicate a difference between chemotaxis strategies employed in the endpoint assay on agar plates versus in the microfluidic gradient assay. For example on plates, animals ascend the gradient once and are paralyzed by a drug at the odor source to facilitate animal counting, whereas the microfluidic assay reports the animals' ability to constantly reorient to remain near the top of the gradient. In addition, the device geometry might prevent some strategies of locomotion that can be accessed on plates that are independent of AIA. This interpretation is consistent with a previous report of AIA laser ablation specifically disrupting regulation of turns in salt gradients but having little effect on the use of directed curves in the salt gradient (Iino and Yoshida, 2009).

Wide field imaging unlocks a wider range of stimuli and genetic analysis of neural dynamics

At the methodological level, this work demonstrates the strength of wide field imaging of neural activity with elevated throughput. In principle, the calcium imaging results presented in this study could have been obtained using traditional imaging techniques that focus on one animal and deliver one stimulus per experiment. However, largely

automated wide field imaging encouraged us to survey a wider range of stimulus conditions and thus led to a clearer picture of the dynamics of adaptation throughout the range of diacetyl concentrations that *C. elegans* detects. Testing ten animals each of two genotypes in a single experiment is not only convenient but is also valuable to confirm experimental consistency, for example by testing a set of control animals in each experiment that experience the same stimulation as the test animals.

Despite the reduced spatial resolution during imaging, neural response dynamics could be reliably quantified even from individual animals. We found a single segregant animal among ~80 double mutant animals in two experiments using a specialized microfluidic device during the initial analysis of the CB450 strain. We recovered and propagated that animal for genome sequencing, providing an important pilot experiment towards genetic screening for mutants that affect neural dynamics.

Outlook

We suggest that our work points to an adaptation based mechanism for spatial orientation in *C. elegans*. We hypothesize that the chemosensory AWA-AIA circuit computes and amplifies small positive dC/dt to suppress turning during runs towards diacetyl odor. Our hypothesis is built on a number of observations presented in this thesis: (1) Neural responses to diacetyl in AWA and AIA are transient and repeatable during successive upsteps in diacetyl concentration and thus reflect dC/dt rather than C of diacetyl. (2) The transient nature of AWA responses appears to be physiologically regulated. (3) The probability of turning is transiently suppressed during upsteps in diacetyl concentration. (4) Optogenetic depolarization of AWA (and AIA, N. Pokala) can mimic odor stimulation and suppress turns.

Building on this hypothesis and the established assays and stimulus conditions will make it now possible to relate these observations more directly to the ultimate behavioral goal of gradient chemotaxis.

Turns are thought to be largely undirected although a weak directional bias has been described (Iino and Yoshida, 2009; Pierce-Shimomura et al., 1999). We would like to characterize how turns contribute to spatial orientation in our assays to understand if the formalization of chemotaxis as a biased random walk is valid and this will require further behavioral analysis in microfluidic gradients. For example, an analysis of individual animal responses during interaction with spatial odor patterns should reveal if indeed turns are undirected and only modulated relative to the baseline when animals move up the gradient. Our initial attempts of this analysis met computational and intellectual challenges in the segmentation of behaviors (e.g. is what looks to the eye like three

closely spaced successive turns that eventually reorient the animal up the gradient a sequence of three undirected turns or, rather, one directed turning event? How can we deal with tracks lost during collisions?). Furthermore, the length scale of our current microfluidic device configuration is similar to the average run length at baseline (0.2 mm/sec x ~ 20 s run length = 4 mm, compared to ~5 mm linear gradient regime within 15 mm total extent of the gradient on both sides) making it difficult to relate the odor gradient to behavior. Larger devices are already being designed.

Optogenetic stimulation provides a powerful means to test directly if suppression of turns is sufficient to generate spatial orientation. A more complete characterization of the AWA::Chrimson strain might identify stimulation intensities that closely mimic the behavioral effect of odor stimulation on turning frequency (to suppress but not subsequently enhance turns). It should be possible to devise a closed loop experiment to acutely bias the random walk of an animal in an isotropic environment by light activation of AWA when animals crawl in one orientation versus another, mimicking AWA activation during movement up and down a gradient. Uniform illumination would provide a purely temporal cue to the animal. In a pilot experiment, we provided patches of light of different intensities on an agar plate to animals expressing Chrimson in AWA. This crude experiment did not result in obvious accumulation of animals in those patches but more sophisticated paradigms such as light gradients may reveal if direct AWA depolarization can guide orientation behavior.

Interpreting optogenetic experiments will benefit from a better understanding of the relationship of AWA depolarization and AWA output signaling to (subcellular) calcium. Our calcium imaging during Chrimson stimulation showed that calcium transients subside during light activation but electrophysiology revealed that Chrimson causes

sustained AWA depolarization (Qiang Liu, unpublished results). This bears the question if AWA depolarization and synaptic output are also transient, as calcium imaging suggests, and if AWA output also adapts and reflects dC/dt. It is currently challenging to apply odors during electrophysiological recordings but we expect that genetically encoded voltage sensors will soon become available for use in *C. elegans*. Furtheremore, a technique to image synaptic vesicle release is currently being developed that likely detects glutamatergic transmission and may be adaptable to monitor chemical transmission from AWA (Donovan Ventimiglia, unpublished results).

We have not yet returned to the freely moving animal configuration with AWA imaging, in part because of difficulties to define AWA specific behaviors on the short length scale of the imaging arenas that seem to lend themselves more towards the analysis of AWC mediated behaviors during steeper changes in odor concentration. This question can now be revisited with a clearer picture of AWA specificity from our behavioral analysis in large devices and from AIA imaging. It will be important to measure how AWA represents diacetyl during ongoing navigation rather than enforced pulses of odor. Imaging AIA in this configuration will also open the possibility to address the question of sources of variability in the behavioral response. One might hypothesize that AIA activation predicts if an animal will suppress turns in response to a diacetyl pulse and that AIA would integrate diacetyl responses with inputs from other sensory neurons. In early experiments, we have extensively studied choice behavior between adjacent microfluidic stripes of diacetyl and isoamyl alcohol odor, presumably causing a behavioral dilemma to respond to AWA or AWC stimulation. Our results indicated that while the two sensory inputs were intact in the sensory neurons under these conditions, they canceled each other at the behavioral level. AIA might be the site of integration of

the two signals. In a stripe choice configuration, AIA activity might predict if an animal chooses the AWA or the AWC stripe.

At the molecular level, we have yet to understand how AWA adapts to sustained stimulation and maintains sensitivity over many orders of magnitude in odor concentration. To guide genetic analysis of the signal transduction cascade, we have started a collaboration with Jamal Rahi aiming to infer the network topology of the adaptation circuit in AWA from calcium responses to systematic stimulation with diacetyl. We have generated a set of data that points towards a negative feedback loop mediating adaptation in AWA and we can now test if mutants in molecules thought to mediate feedback, such as Calmodulin, or disruption of calcium signaling using nemadipineA, change this topology.

The ease of experimental access to AWA and the behavioral framework suggest that it may be possible to move the analysis of *C. elegans* chemotaxis towards the level of understanding achieved in *E. coli*. It may be possible to link molecular events underlying sensory signal transduction and the detection of dC/dt to behavioral output to provide an example of a complete circuit analysis spanning the levels of computation, algorithm and implementation.

Experimental Procedures

Chapter 2: High Throughput Imaging

Automated imaging and stimulation.

We built the automated microscope on a Zeiss AxioObserver.A1 inverted body with Zeiss Fluar objective lenses (2.5x/0.12 NA, or 5x/0.25 NA) and an Andor iXon3 DU-897 EM-CCD camera mounted with a 0.63x or 1.0x c-Mount adapter. A custom-built digital timing circuit synchronized image capture with illumination pulses of adjustable duration and delay from a Lumencor SOLA-LE solid-state lamp. Metamorph 7.7.6 software controlled both image streaming (typically 10–30 frames s−1 for 30–60 s) and stimulus delivery via digital signals (from National Instruments NI-DAQmx to an Automate Valvebank 8 II actuator and Lee Corporation solenoid valves) and via serial commands to a Hamilton MVP 8-way distribution valve. Custom journal scripts selected from various pre-programmed recording parameters (exposure, binning, stream length, trial interval) and stimulation parameters (stimulation valve timing and odor selection valves). Fully-automated experiments (tested up to 12 hrs) required no further user intervention once a session was initiated.

Microfluidic device designs.

Odor pulses were delivered using a microfluidic device designed with a shifting-flow strategy that prevent pressure or flowrate discontinuities detectable by the animal (Chronis et al., 2007) (Figure 2-2A). One of two stimulus streams was directed into the arena using a computer-controlled three-way valve that switched the flow position of a

“control” fluid stream, while the other stimulus stream bypassed the arena directly to the outflow (Figure 2-2E).

Stripe and gradient devices were based on our previous designs (Albrecht and Bargmann, 2011). In the stripe device, three separate fluidic inlets provided the top, middle, and bottom fluid streams (Figure 2-2B). In the linear gradient device, two fluid streams entered a three-stage ‘mixing tree’ composed of converging and diverging channels that divide the flow into nine streams with linearly-varying concentration (Figure 2-2C). All spatial odor profiles were verified using dye solutions before each experiment.

For direct comparison of neural responses in two populations (e.g. mutant vs. WT), we used a two-arena pulse device (Figure 2-2D), modified from the standard pulse device by adding a second animal loading port and a physical barrier parallel to fluid flow. Chemical switch timing was comparable in both arenas in this design, and the chemical screen in *odr-10* mutants was performed in parallel with WT controls using this device (Figure 2-9B-E).

Microfluidic device fabrication.

We prepared monolayer microfluidic devices (Figure 2-2) using soft lithography (Albrecht and Bargmann, 2011). Briefly, we fabricated silicon mold masters using conventional photolithographic techniques to pattern a 70 µm layer of SU8 2050 photoresist (Microchem) on 4-inch wafers (Silicon Quest). Photomasks were printed at 5,080 dpi (Pageworks). We cast ~5-mm-thick PDMS devices (Sylgard 184 A and B, 1:10 by weight; Dow Corning) and cored inlet and outlet holes with a 1-mm dermal punch (Accuderm). We cleaned devices in 95% EtOH at least overnight to remove residual PDMS monomers, rinsed them in water and baked them for at least 30 min at 55 °C to

evaporate any absorbed EtOH. Devices were reversibly sealed against a hydrophobic 25 x 50 mm glass slide, prepared by exposure to (tridecafluoro-1,1,2,2-tetrahydrooctyl)-1-trichlorosilane (United Chemical Technologies) vapor for 1 h under vacuum. We placed a support glass slide containing inlet and outlet holes drilled with a diamond-coated bit above the PDMS device and clamped it in a stage adapter (Warner Instruments, P-2) modified with longer screws and rubber washers.

We regulated flow velocities in the arena from 0.1–2 mm s−1 by gravity proportional to the height differential, Δ*h*, between stimulus and outflow reservoir surfaces, from 5–150 cm. Fluidic connections were made with microbore tubing (Tygon S-54-HL, 0.020”ID) containing a metal tube (New England Small Tubing, NE-1027-12) on one end for insertion into the microfluidic device, and a Luer stub needle on the other for connection to a valve, reservoir, or syringe. We used high-purity Teflon PFA tubing (IDEX) to prevent cross-contamination when presenting multiple stimuli within an experiment. Stimuli were delivered from 30-mL syringe reservoirs (Figure 2-2F). Alternatively, up to eight stimuli were directed through an electrically-actuated distribution valve, e.g. for a dose response curve (Figure 2-2G). For chemical screening, stimulus streams were fed from a 96-well plate (Figure 2-2H).

Strains.

C. elegans were maintained under standard conditions and fed OP50 bacteria(Brenner, 1974). Wild-type worms were Bristol strain (N2). The following strains expressed GCaMP variants in different neurons:

AWA: CX14887, kyIs598 [*gpa-6*::GCaMP2.2b 50ng/µl]

CX15127, *odr-10(ky32)*; kyIs598

AWC: CX14215, kyEx4467 [*str-2*::GCaMP5 D380Y 50ng/µl]

ASH: CX10979, kyEx2865 [*sra-6*::GCaMP3 100 ng/µl]

AVA: CX15380, kyEx5170 [*rig-3*::GCaMP5.0 30ng/ul]

AIA: CX14034, kyEx4345 [*gcy-28d*::GCaMP2.2b 50ng/ul]

AIY: CX14780, *lite-1(ce314)*; kyEx4857 [*mod-1*::GCaMP5 25ng/µl]

The GCaMP cDNAs were kindly provided by Loren Looger and subcloned into the pSM vector using NotI restriction sites. Neuron-selective promoters were exchanged using FseI and AscI sites flanking the promoter sequence in this vector. Transgenic animals were generated by injecting DNA clones and a fluorescent co-injection marker (*ofm-1::dsRED*) into gonads of young adult hermaphrodites. We performed multi-copy integration of the *gpa-6::GCaMP2.2b* extrachromosomal array using UV irradiation, and the resulting strain CX14887 was back-crossed six times to wild-type *C. elegans*.

To provide age-synchronized young adults for each experiment, we picked L4 larval stage animals onto agar plates 15–20 h earlier. Immediately before each experiment, we gently transferred 1 to 25 worms onto a fresh, unseeded agar plate with a small amount of bacteria. After removing excess bacteria, we flooded the plate with ~5 ml S-basal

buffer (100 mM NaCl and 50 mM potassium phosphate; pH 6.0). Swimming animals were then drawn into “worm loading” tubing using a 1-mL syringe.

Stimulus preparation.

Odor dilutions were prepared fresh on the day of the experiment from pure stock solutions (isoamyl alcohol, diacetyl, glycerol) or from 1:100 dilutions in ethanol for odor screening. Dilutions were made in S-basal buffer. Where mentioned, 1 mM (-)-tetramisole hydrochloride (Sigma) was added to S-basal to paralyze body wall muscles and keep animals stationary.

Experimental setup.

We assembled the microfluidic arenas and degassed them in a vacuum desiccator for at least 10 min before loading S-basal buffer through the outlet port. This step ensures that any air bubbles absorb quickly into the PDMS. We connected tubing from the stimulus and control reservoirs to the arena and flushed the device with S-basal buffer. Next, we attached the loading tubing and gently injected 1–25 worms via syringe into the arena. Typically, 10-20 animals were loaded when animals were paralyzed during imaging, and 1-2 animals were loaded for freely moving animals, to facilitate tracking. Buffer flow continuously washed the animals, removing any residual bacteria. Experiments in freely-moving worms began typically after 15–20 min in the device and 30 min after removal from bacterial food, once local search behaviors subsided. For experiments in tetramisole-paralyzed worms, we allowed 60 minutes of buffer flow for maximal paralysis. For repeated stimulation, we preconditioned animals with 5–10 trials to stabilize responses, except for the dose response experiment in Figure 2 where we report responses of naïve animals.

After each experiment, we flushed arenas with water and soaked them in ethanol for 24 h to remove any residual odor. Next, we rinsed devices in water, dried them in an air stream and baked them at 55 °C for at least 30 min. After this cleaning procedure, buffer-buffer controls showed no response, and devices could be reused over 30 times.

Data analysis and statistics.

We analyzed video for neural fluorescence and locomotory behavior using the NeuroTracker software suite, a set of custom ImageJ macros and MATLAB scripts described in the Supplementary Note. Typically, 70-90% of animals in the device could be tracked. Background-corrected integrated neural fluorescence traces *F(t)* were divided by baseline fluorescence *F*0 (mean for the first 5 s) to obtain the normalized calcium response (Δ*F*/*F*0), for each animal and stimulation trial. Normalized traces were then averaged across repeated trials for each animal. Population-average responses report the mean and variance of individual animal responses. Statistical comparisons were made by ANOVA using Bonferroni's correction for multiple comparisons, or the Benjamini-Hochberg correction where indicated. Data are presented from one experiment unless otherwise stated.

Neuronal calcium response dynamics were quantified as the peak fluorescence and peak delay time determined for each animal and trial from normalized fluorescence traces smoothed with a 0.3-s window. Unless otherwise stated, we averaged calculated response parameters from repeated trials for each animal and reported statistics on the variance between animals. Peak fluorescence was calculated as maximum fluorescence during the stimulus pulse (stim) minus maximum fluorescence during the 2-s (20 frames)

period prior to stimulation (prestim): $\max(\Delta F/F_0)_{stim} - \max(\Delta F/F_0)_{prestim}$. Peak delay time was determined as the time after stimulus onset when maximum fluorescence occurred.

Variance across repeated trials and across animals (Figure 2-7D) was calculated using the MATLAB "var" function on peak calcium fluorescence per neural trace. Dose-response curves were fit using the MATLAB curve-fitting toolbox and function "cfit" to a four-parameter sigmoidal curve defined by $F' = F'_{min} + (F'_{max} - F'_{min})/[1 + (EC50/C)^{ß}]$ where $F' = \Delta F/F_0$ for each trace and C is odor concentration. EC50 represents the odor concentration eliciting a 50% maximal peak response and the parameter $ß$ represents the dynamic range of the response.

Gradient quantification

For experiments involving changes in the stimulus gradient *dC/dt* (Figure 2-7G,J), we measured *dC/dt* and stimulus timing in the imaging arena at different flow rates in separate dye experiments. *dC/dt* in the imaging arena was calculated by imaging fluorescein dye switched against buffer. We used the Matlab function “polyfit” to calculate the slope of increase in normalized dye fluorescence during four frames surrounding half maximal fluorescence.

NeuroTracker software suite.

Neural fluorescence was extracted from raw video data using a tracking macro ("NeuronTracking") written in the ImageJ (NIH, version 1.45q). Neuron positions were tracked frame-to-frame for moving or stationary animals. The user first selects an intensity threshold and initial positions for each neuron and/or animal. The script automatically analyzes all animals using a particle tracking algorithm to identify the

brightest pixel within a local search region. The software tracks stationary animals throughout consecutive recordings based on position without further user intervention. When moving animals collide or rapidly change direction, the tracking software may halt (if no acceptable neuron location can be found) and await user input to reselect the neuron centroid.

Raw fluorescence intensity F_R was recorded as the mean intensity from a 4x4 pixel region centered on the center of mass of the object identified by the tracker (Figure 2-5) for all neurons except AIA where a 6x6 pixel region was used to include more of the signal contributed by the neurite. Background intensity F_{bg} was calculated as median intensity from a ring shaped region surrounding the tracked neuron at a distance to include mostly background pixels. Raw parameters saved to a text file for each neuron tracked include: frame number, x-y center of mass, integrated and maximum neuron intensity, and median background intensity, threshold value, and threshold area.

Subsequent data analysis and display was performed in Matlab 2011b. Background subtracted fluorescence F was calculated as $F = F_R - F_{bg}$. Unless otherwise stated, we report change in fluorescence ($\Delta F/F_0$) as $(F - F_0)/ F_0$ where F_0 is mean F during the first 5s of each trial.

Behavioral analysis

We analyzed locomotory behavior from the raw video data with the "BehaviorMontage" ImageJ macro, which combines all trials of an experiment into a single montaged video, downsampled to ~40 pixels mm^{-1} resolution and 2 frames s^{-1}. Adjusted videos were then compatible with the MATLAB script “SmallArenaTracker.m”, a modified version of the existing MATLAB ArenaWormTracker suite that segments each worm for centroid

and shape information and classifies its instantaneous behavioral state. Modifications were made to deconvolve the original video number and centroid position from a single montaged video per multi-trial experiment. Behavioral data were visualized for each trial and animal to verify correct classification and were manually corrected if necessary.

Chapter 3

Paired Pulse imaging

Pairs of two one second pulses of diacetyl at 1 uM were delivered at intervals of 0 – 20 s within each pair and 60 s between pulse pairs. We analyzed odor responses after fast habituation of AWA had subsided and responses entered the consistent regime.

Mapping of *che-3* in CB450

CB450 animals did not show desensitization of AWA responses to 10 s pulses of 1 uM diacetyl. To separate the *unc-13(e450)* allele from the mutation underlying the lack of desensitization, we back-crossed CB450 animals to wild type. The resulting F1 progeny were allowed to self-fertilize yielding F2 progeny of which ¼ had the uncoordinated phenotype caused by *unc-13(e450)*. 80 uncoordinated F2 animals were screened for intact desensitization. An uncoordinated animal with intact desensitization would indicate that recombination had occurred between the two loci.

80 animals were imaged in groups of 10-15 in a specialized device with four arenas that could be recorded sequentially, allowing us to paralyze and pre-adapt up to 50 animals at once for subsequent testing. Each arena was then recorded once and rudimentary analysis of raw fluorescence from individual animal AWA neurons identified one animal

with normal desensitization that could be recovered from the microfluidic device by carefully opening the device and using a platinum wire. This animal was propagated and homozygosed by identifying F3 progeny that only threw normally desensitizing F4 progeny.

We prepared genomic DNA from the homozygous backcrossed *unc-13(e450)* and the original CB450 using standard kits for whole genome sequencing. Sequence reads were aligned using custom written software (McGrath et al., 2011). Comparison of single nucleotide polymorphisms (SNPs) that differed between the two strains and the reference genome revealed 6 coding changes to the right of *unc-13* on chromosome I in CB450 that were lost in the back-crossed strain. Rescue of AWA desensitization in CB450 using a fosmid containing wild type *che-3* and comparison with AWA responses in the canonical *che-3(e1124)* identified the SNP in *che-3* as the causal mutation in CB450 for defective desensitization.

Mapping of inpp5e

ky121 was described as having a defect in pyrazine chemotaxis, an odor detected by AWA. Genetic mapping had established linkage to the left of *unc-30* on chromosome IV (Roayaie, Bargmann, unpublished results). We used the *unc-30* marker to follow *ky121* during crosses with our imaging strain. F1 progeny was self-fertilized and the uncoordinated F2 progeny animals were tested for an AWA adaptation phenotype.

After two additional back-crosses with wild type animals, whole genome sequencing identified 12 coding changes within 4 mega base pairs to the left of *unc-30*. Fosmid recue identified a SNP in T25B9.10 as the causal mutation.

Crowd-sourcing of *inpp5e* mutant phenotyping

inpp5e(ky121) mutant animals had a tendency to exhibit patches of high ODR-10::GFP fluorescence in maximum intensity z-stack projections that were not present in wild type animals. Initial computational attempts using intensity histograms did not recover this difference. Instead, we generated a small internet page that displayed 5 representative images of each genotype labeled for reference. Below, we showed 50 additional, unlabeled images and visitors to the page were asked to label these images by paying attention to the fluorescent patches. All images had to be labeled as wild type or mutant. A $20 Amazon gift card was promised as a reward to the participant scoring the highest percentage of images correctly. 18 people (friends and family) participated.

Microfluidic gradient assay

We used microfluidic gradient chambers to create sigmoidal odor gradients of 32 mm width and a concentration profile that can be approximated by the logistic function ——— where -1<x<1; k=5 and which is approximately linear on the two flanks of the gradient, (Figure 3-12) (Albrecht and Bargmann, 2011).

For example, a gradient from 0.1 uM to 1 uM has a dC/dx of 0.11 uM/mm on the linear flanks and worms moving at .2 mm/sec experienced a rate of change in concentration (dC/dt) of up to .019 uM/sec. The device geometry constrains animals to paths at zero (parallel to the gradient) and sixty degree angles relative to the gradient. Animals crawling up the gradient experience a fold-change (% dC/dt) of approximately 1-5 %/sec, measured as the change in concentration over one second divided by the concentration at the beginning of that second.

We transferred groups of 20 animals into buffer-filled devices and allowed them to disperse and adapt to the novel environment for one hour. During the first 30-45 minutes, animals moved more slowly and display elevated rates of pausing and short reversals, likely reflecting a local search strategy upon removal from food (Gray et al., 2005) and after this period, animals entered a more consistent behavioral regime.

After one hour, we started the flow of two different odor concentrations into the device to establish a gradient. One stimulus (A) flows through the middle of the arena and the other stimulus (B) flows on both sides. A mixing tree upstream of the arena facilitates diffusion between the two stimuli thereby generating a smooth gradient of intermediate concentrations. Our setup allowed computer-controlled dynamic switching of the stimulus passing through the middle of the device.

Microfluidic Pulse Assay

In this experimental design, all animals in a microfluidic arena are subjected to the same stimulus when a computer controlled valve switches between alternative flows into the arena. This setup produces increases in odor concentration as an exponential decay function with a time constant k of about 20 seconds. The time constant k reflects diffusive mixing of successive stimuli in the delivery channels before they enter the arena and can be tuned by modulating the flow rate through the device to achieve the desired dC/dt. To increase time resolution of our post-hoc analysis of turning behavior in response to odor steps, the timing of odor encounter was corrected for each animal's location in the device based on dye measurements at the same flow rate (Albrecht and Bargmann, 2011).

The range of dC/dt during step pulses was chosen match the magnitude of dC/dt experienced during gradient crawling. During fold-changes in diacetyl concentration starting with a step from 0.1 to 0.158 uM and ending at 1.58 uM, dC/dt ranged from 0.003 - 0.04 uM/sec and each pulse had a maximum fold change of 4%/sec (Figure 3-14) (compared with 0.02 uM/sec in a gradient from .1 uM to 1 uM).

Chrimson stimulation during calcium imaging

To activate Chrimson during calcium imaging we mounted an external red LED above the microfluidic imaging chamber to illuminate animals with a wavelength band of 605/50 nm, observing negligible bleed-through from the red LED into the G-CaMP recording (<10% of signal to noise ratio).

The 470 nm light used to excite G-CaMP also triggered calcium transients in some animals when delivered at high intensities. We reduced this undesired activation by strobing the excitation light at a 10% duty cycle (10 ms ON, 90 ms OFF) at a reduced intensity of about 10 mW/cm^2 (10 % of light power normally used during wide field imaging).

Because of dimmer G-CaMP expression in AIA processes compared to AWA cell bodies, we used light intensities of 100 mW/cm^2 to maintain an acceptable signal to noise ratio for G-CaMP imaging and could not entirely eliminate cross-activation of Chrimson. As a concequence, we observed strong blue light induce calcium transients in AIA in dark adapted animals (data not shown). Conveniently though, these adapted efficiently such that subsequent recordings only showed calcium transients in response to red light activation.

Strains used in Chapter 3

Cilium morphology		
CX11826	kyEx3208	kyEx3208= *odr-7*::GFP + *ofm-1*::RFP 15ng/ul.
CX15804	*osm-6(p811)*; kyEx3208	
CX15805	*ky121*; kyEx3208	
CX15806	*osm-3(p802)*; kyEx3208; kyIs587	
Crowdsourcing		
CX3344	kyIs53	kyIs53= full length *odr-10::gfp*
CX15892	kyIs53;*ky121*	
AIA imaging		
CX15257	kyEx5128	kyEx5128= gcy28d::GCaMP D381Y, coel::dsRed
CX16169	*ceh-36(ky640)* X ,kyEx5128	
CX16170	*odr-10(ky32*) X ,kyEx5128	
CX16171	*odr-7(ky4)* X ,kyEx5128	
CX15951	*osm-6(p811)*,kyEx5128	
CX15953	*ky121*; kyEx5128	
CX16410	*eat-4(ky5)* ,kyEx5128	
CX16424	*osm-6(p811),odr-10(ky32)*; kyEx5128	
CX16338	*osm-6(p811)*, kyEx5128,kyEx5406	kyEx5406 = odr-7p::mCherry::osm-6 5ng/ul, *elt*-2::mCherry 2ng/ul, pSM 95ng/ul.
CX16340	*ky121*; kyEx5128; kyEx5405	kyEx5405 = *odr-7*p::mCherry::T25B9.10a 5ng/ul, *elt*-2::mCherry 2ng/ul, pSM 95ng/ul.
AIA hyperpolarization		
CX14597	kyEx4745	kyEx4745 = *gcy-28dp::unc-103(gof)*::SL2::*mCherry* 30ng/ul, *elt-2::mCherry* 2ng/ul, pSM 70ng/ul
AWA imaging		
CX14887 = CX14647	kyIs598 = kyIs587	kyIs598/kyIs587 = *gpa-6p*::*G-CaMP2.2b* 50ng/ul, *coel*::dsRed 15ng/ul, pSM 35ng/ul
AWA signal transduction mutants		
CX15510	*ocr-2(ak47);* kyIs587	
CX15909	*ocr-1(ak47), ocr-2(ok132)*; kyIs588	
CX15614	osm-9(ky10); kyIs587	
CX15127	*odr-10 (ky32)* X; kyIs587	
CX15217	*egl-19(n582)*; kyIs587	
CX15504	*tax4(p678)*; kyIs587	
CX15731	*tax-2 (p691)* I; kyIs587	
CX14881	*unc-13 (e450)* I *che-3(kyX)*; kyIs587	
CX15140	*unc-13 (e450) I; kyIs587*	
CX15128	*unc-13 (e51)* I; kyIs587	
CX15129	*unc-13 (s69)* I; kyIs587	
CX16012	*arr-1(ok401);* kyIs587	
AWA IFT mutants & rescue		
CX15505	*osm-6(p811)*; kyIs587	
CX15506	*osm-3(p802)*; kyIs587	
CX15509	*che-2(e1033)*; kyIs587	
CX15545	*che-3(e1124)*; kyIs587	

CX15959	kyIs587, *osm-6(p811),* kyEx5406	kyEx5406 = *odr-7p::mCherry::osm-6* 5ng/ul, *elt-2::mCherry* 2ng/ul, pSM 95ng/ul.
AWA *inpp5* mutants & rescue		
CX15615	*ky121*; kyIs587	
CX15793	*T25B9.10(gk850109*); kyIs587	VC40856 = Million Mutation Project strain
CX15831	*T25B9.10(gk3262)*; kyIs587	VC2109 = KO consortium strain
CX15763	*ky121*; kyEx5298; kyIs587	kyEx5298 = WRM061dE11 2ng/ul, elt-2::mCherry 2ng/ul, pSM 96ng/ul.
CX15765	*ky121*;kyEx5300; kyIs587	kyEx5300 = WRM0636cG02 2ng/ul, elt-2::mCherry 2ng/ul, pSM 96ng/ul.
CX15800	*ky121*;kyEx5325; kyIs587	kyEx5325 = *odr-7p::T25B9.10a::sl2::mCherry* 3ng/ul, *elt-2::mCherry 2ng/ul*, pSM 95ng/ul.
CX15801	*ky121*; kyEx5326; kyIs587	kyEx5326 = *odr-7p::T25B9.10b::sl2::mCherry* 3ng/ul, *elt-2::mCherry* 2ng/ul, pSM 95ng/ul.
CX15958	kyIs587, *ky121*, kyEx5405	kyEx5405 = *odr-7p::mCherry::T25B9.10a* 5ng/ul, elt-*2::mCherry* 2ng/ul, pSM 95ng/ul.
CX16082	kyEx4520; kyEx5405	kyEx4520 = T25B9.10::gfp TransgeneOmics construct 5ng/ul, *coel::dsRed* 15ng/ul, pSM 80ng/ul. kyEx5405 = *odr-7p::mCherry::T25B9.10a* 5ng/ul, elt-2::mCherry 2ng/ul, pSM 95ng/ul
CX15832	kyIs602, *ky121*	KyIs602= *p-sra-6:GCaMP3.0* injected at 75ng/uL and *coel:GFP* injected at 10ng/uL,
Chrimson		
CX16561	kyEx5128; kyEx5662	kyEx5128= *gcy28d::GCaMP D381Y*, coel::dsRed; KyEx5662 = *odr-7p::Chrimson::SL2::mCherry* 5ng/ul, *elt-2::mCherry 2 ng/ul*, pSM 93 ng/ul
CX16573	kyIs587; kyEx5662	KyEx5662 = *odr-7p::Chrimson::SL2::mCherry* 5ng/ul, *elt-2::mCherry* 2 ng/ul, pSM 93 ng/ul.

Appendix

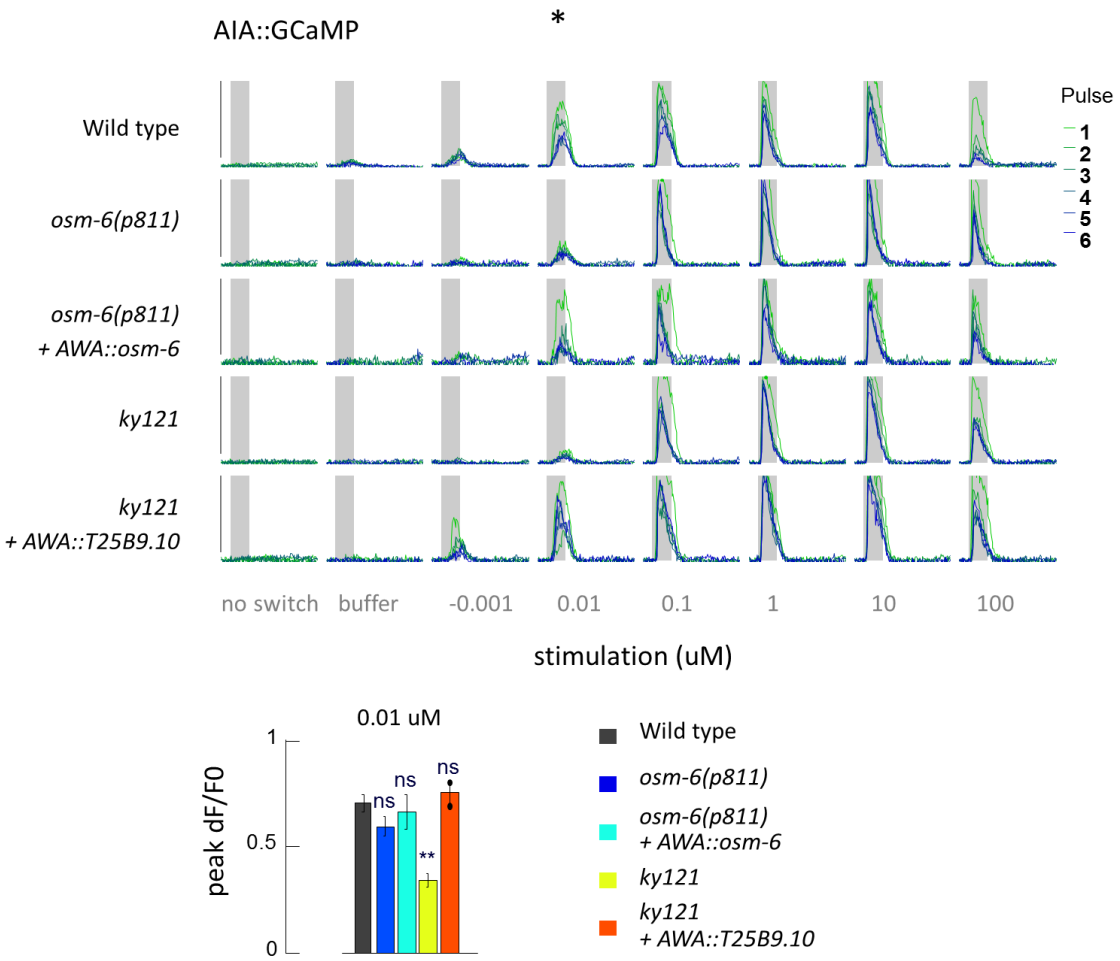

Figure A-0-1 **AWA specific rescue of AIA responses in *osm-6* and *inpp5e* mutants.** Weak AIA responses at 0.01 uM diacetyl concentration in *inpp5e(ky121)* mutants are rescued by expression of T25B9.10a in AWA (**P<.0001) n = 11-29 animals x six odor pulses.

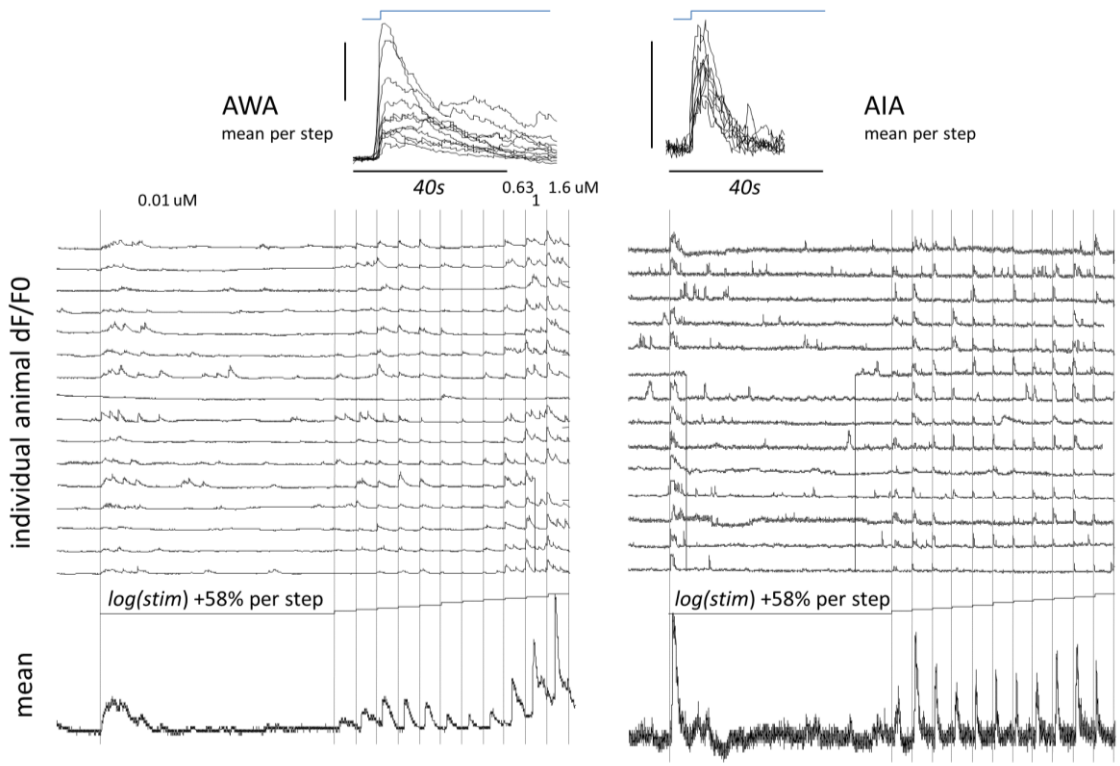

Figure A-0-2 **Individual animal neural responses to fold-change stimulation.**
AWA exhibits secondary calcium transients upon first stimulation at 0.01 uM and at concentrations above 0.63 uM.

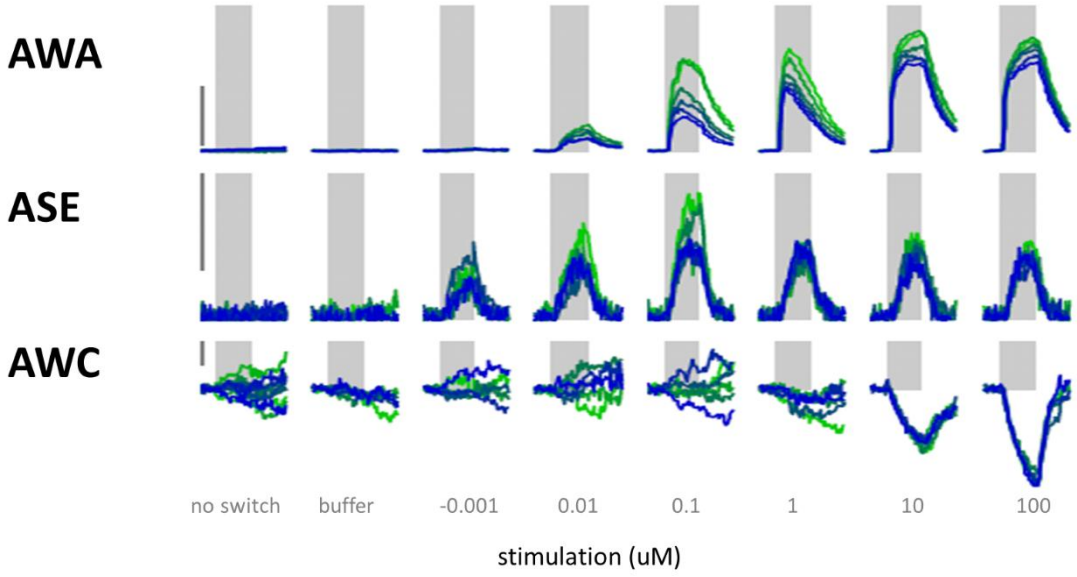

Figure A-0-3 **Diacetyl responses in ASE and AWC sensory neurons.**
Mean GCaMP fluorescence in ASE and AWC during diacetyl stimulation. AWC fluorescence is suppressed at diacetyl concentrations above 1 uM.

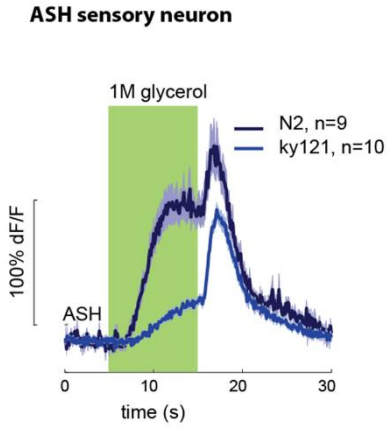

Figure A-0-4 ***inpp5e* also affects ASH sensory neuron responses to glycerol.**

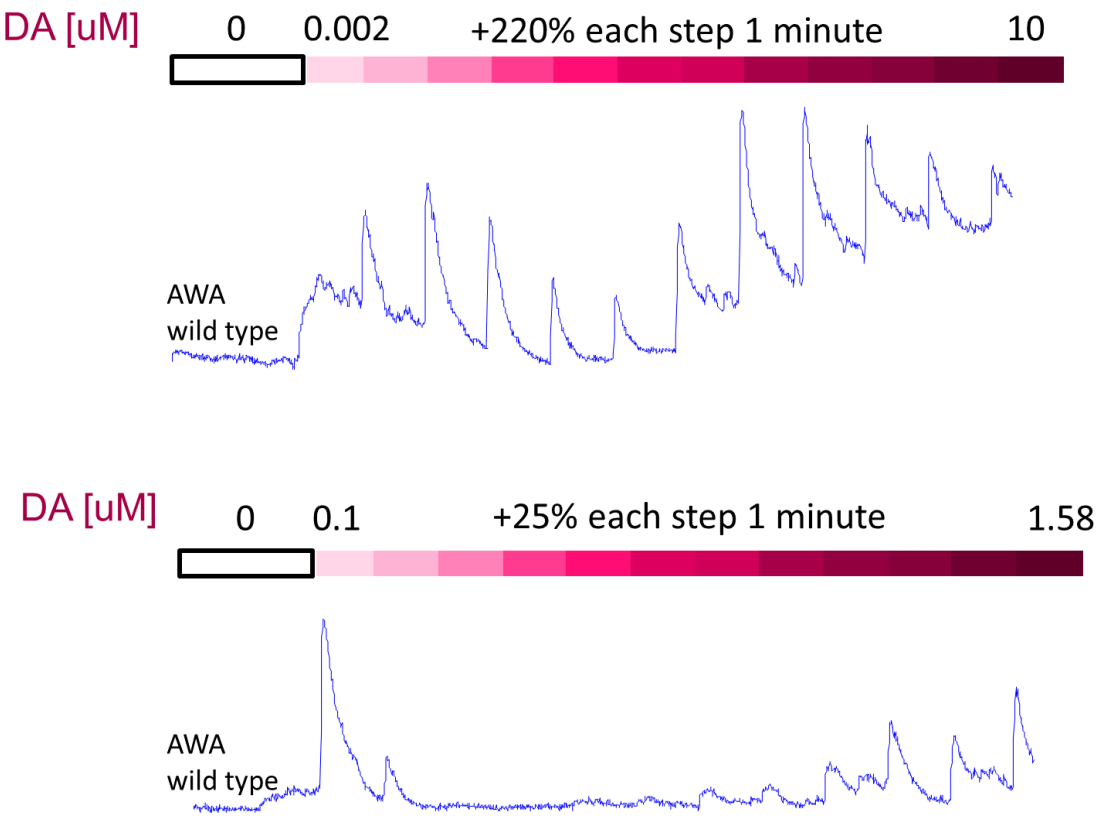

Figure A-0-5 **AWA responses to different diacetyl fold-changes.**

References

Ahrens, M.B., Li, J.M., Orger, M.B., Robson, D.N., Schier, A.F., Engert, F., and Portugues, R. (2012). Brain-wide neuronal dynamics during motor adaptation in zebrafish. Nature *485*, 471–477.

Albrecht, D.R., and Bargmann, C.I. (2011). High-content behavioral analysis of Caenorhabditis elegans in precise spatiotemporal chemical environments. Nat. Methods.

Appleby, P.A. (2013). The role of multiple chemotactic mechanisms in a model of chemotaxis in C. elegans: different mechanisms are specialised for different environments. J. Comput. Neurosci.

Ben Arous, J., Tanizawa, Y., Rabinowitch, I., Chatenay, D., and Schafer, W.R. (2010). Automated imaging of neuronal activity in freely behaving Caenorhabditis elegans. J. Neurosci. Methods *187*, 229–234.

Bae, Y.-K., Kim, E., L'Hernault, S.W., and Barr, M.M. (2009). The CIL-1 PI 5-Phosphatase Localizes TRP Polycystins to Cilia and Activates Sperm in C. elegans. Curr. Biol. *19*, 1599–1607.

Bargmann, C.I. (2006a). Chemosensation in C. elegans. WormBook 1–29.

Bargmann, C.I. (2006b). Comparative chemosensation from receptors to ecology. Nature *444*, 295–301.

Bargmann, C.I., and Horvitz, H.R. (1991a). Control of larval development by chemosensory neurons in Caenorhabditis elegans. Science *251*, 1243–1246.

Bargmann, C.I., and Horvitz, H.R. (1991b). Chemosensory neurons with overlapping functions direct chemotaxis to multiple chemicals in C. elegans. Neuron *7*, 729–742.

Bargmann, C.I., Hartwieg, E., and Horvitz, H.R. (1993). Odorant-selective genes and neurons mediate olfaction in C. elegans. Cell *74*, 515–527.

Barkai, N., and Leibler, S. (1997). Robustness in simple biochemical networks. Nature *387*, 913–917.

Benhamou, S., and Bovet, P. (1989). How animals use their environment: a new look at kinesis. Anim. Behav. *38*, 375–383.

Berg, H.C. (1993). Random walks in biology (Princeton, N.J: Princeton University Press).

Berg, H.C. (2004). E. coli in motion (New York: Springer).

Berg, H.C., and Brown, D.A. (1972). Chemotaxis in Escherichia coli analysed by Three-dimensional Tracking. Nature *239*, 500–504.

Bielas, S.L., Silhavy, J.L., Brancati, F., Kisseleva, M.V., Al-Gazali, L., Sztriha, L., Bayoumi, R.A., Zaki, M.S., Abdel-Aleem, A., Rosti, R.O., et al. (2009). Mutations in INPP5E, encoding inositol polyphosphate-5-phosphatase E, link phosphatidyl inositol signaling to the ciliopathies. Nat. Genet. *41*, 1032–1036.

Bono, M. de, and Villu Maricq, A. (2005). Neuronal substrates of complex behaviors in C. elegans. Annu Rev Neurosci *28*, 451–501.

Braitenberg, V. (1986). Vehicles : experiments in synthetic psychology (Cambridge Mass.: MIT Press).

Brear, A.G., Yoon, J., Wojtyniak, M., and Sengupta, P. (2014). Diverse Cell Type-Specific Mechanisms Localize G Protein-Coupled Receptors to Caenorhabditis elegans Sensory Cilia. Genetics *197*, 667–684.

Brenner, S. (1974). The genetics of Caenorhabditis elegans. Genetics *77*, 71–94.

Bretscher, A.J., Kodama-Namba, E., Busch, K.E., Murphy, R.J., Soltesz, Z., Laurent, P., and de Bono, M. (2011). Temperature, Oxygen, and Salt-Sensing Neurons in C. elegans Are Carbon Dioxide Sensors that Control Avoidance Behavior. Neuron *69*, 1099–1113.

Busch, K.E., Laurent, P., Soltesz, Z., Murphy, R.J., Faivre, O., Hedwig, B., Thomas, M., Smith, H.L., and de Bono, M. (2012). Tonic signaling from O2 sensors sets neural circuit activity and behavioral state. Nat. Neurosci. *15*, 581–591.

Chalasani, S.H., Chronis, N., Tsunozaki, M., Gray, J.M., Ramot, D., Goodman, M.B., and Bargmann, C.I. (2007). Dissecting a circuit for olfactory behaviour in Caenorhabditis elegans. Nature *450*, 63–70.

Chalasani, S.H., Kato, S., Albrecht, D.R., Nakagawa, T., Abbott, L.F., and Bargmann, C.I. (2010). Neuropeptide feedback modifies odor-evoked dynamics in Caenorhabditis elegans olfactory neurons. Nat. Neurosci. *13*, 615–621.

Chalfie, M., Sulston, J.E., White, J.G., Southgate, E., Thomson, J.N., and Brenner, S. (1985). The neural circuit for touch sensitivity in Caenorhabditis elegans. J. Neurosci. *5*, 956–964.

Chou, J.H., Bargmann, C.I., and Sengupta, P. (2001). The Caenorhabditis elegans odr-2 gene encodes a novel Ly-6-related protein required for olfaction. Genetics *157*, 211–224.

Chronis, N., Zimmer, M., and Bargmann, C.I. (2007). Microfluidics for in vivo imaging of neuronal and behavioral activity in Caenorhabditis elegans. Nat. Methods *4*, 727–731.

Clark, D.A., Biron, D., Sengupta, P., and Samuel, A.D.. (2006). The AFD sensory neurons encode multiple functions underlying thermotactic behavior in Caenorhabditis elegans. J. Neurosci. *26*, 7444.

Clokey, G.V., and Jacobson, L.A. (1986). The autofluorescent “lipofuscin granules” in the intestinal cells of Caenorhabditis elegans are secondary lysosomes. Mech. Ageing Dev. *35*, 79–94.

Cluzel, P. (2000). An Ultrasensitive Bacterial Motor Revealed by Monitoring Signaling Proteins in Single Cells. Science *287*, 1652–1655.

Coburn, C., Allman, E., Mahanti, P., Benedetto, A., Cabreiro, F., Pincus, Z., Matthijssens, F., Araiz, C., Mandel, A., Vlachos, M., et al. (2013). Anthranilate Fluorescence Marks a Calcium-Propagated Necrotic Wave That Promotes Organismal Death in C. elegans. PLoS Biol. *11*, e1001613.

Codling, E.A., Plank, M.J., and Benhamou, S. (2008). Random walk models in biology. J. R. Soc. Interface *5*, 813–834.

Cohen-Saidon, C., Cohen, A.A., Sigal, A., Liron, Y., and Alon, U. (2009). Dynamics and Variability of ERK2 Response to EGF in Individual Living Cells. Mol. Cell *36*, 885–893.

Colbert, H.A., and Bargmann, C.I. (1995). Odorant-specific adaptation pathways generate olfactory plasticity in C. elegans. Neuron *14*, 803–812.

Collet, J., Spike, C.A., Lundquist, E.A., Shaw, J.E., and Herman, R.K. (1998). Analysis of osm-6, a gene that affects sensory cilium structure and sensory neuron function in Caenorhabditis elegans. Genetics *148*, 187–200.

Conduit, S.E., Dyson, J.M., and Mitchell, C.A. (2012). Inositol polyphosphate 5-phosphatases; new players in the regulation of cilia and ciliopathies. FEBS Lett. *586*, 2846–2857.

Dombeck, D.A., Khabbaz, A.N., Collman, F., Adelman, T.L., and Tank, D.W. (2007). Imaging Large-Scale Neural Activity with Cellular Resolution in Awake, Mobile Mice. Neuron *56*, 43–57.

Doroquez, D.B., Berciu, C., Anderson, J.R., Sengupta, P., and Nicastro, D. (2014). A high-resolution morphological and ultrastructural map of anterior sensory cilia and glia in Caenorhabditis elegans. eLife *3*, e01948.

Dusenbery, D. (1980). Responses of the nematodeCaenorhabditis elegans to controlled chemical stimulation. J. Comp. Physiol. *136*, 327–331.

Fang-Yen, C., Gabel, C.V., Samuel, A.D.T., Bargmann, C.I., and Avery, L. (2012). Laser Microsurgery in Caenorhabditis elegans. In Methods in Cell Biology, (Elsevier), pp. 177–206.

Faumont, S., and Lockery, S.R. (2006). The Awake Behaving Worm: Simultaneous Imaging of Neuronal Activity and Behavior in Intact Animals at Millimeter Scale. J. Neurophysiol. *95*, 1976–1981.

Faumont, S., Rondeau, G., Thiele, T.R., Lawton, K.J., McCormick, K.E., Sottile, M., Griesbeck, O., Heckscher, E.S., Roberts, W.M., Doe, C.Q., et al. (2011). An Image-Free Opto-Mechanical System for Creating Virtual Environments and Imaging Neuronal Activity in Freely Moving Caenorhabditis elegans. PLoS ONE *6*, e24666.

Firestone, A.J., Weinger, J.S., Maldonado, M., Barlan, K., Langston, L.D., O'Donnell, M., Gelfand, V.I., Kapoor, T.M., and Chen, J.K. (2012). Small-molecule inhibitors of the AAA+ ATPase motor cytoplasmic dynein. Nature *484*, 125–129.

Flavell, S.W., Pokala, N., Macosko, E.Z., Albrecht, D.R., Larsch, J., and Bargmann, C.I. (2013). Serotonin and the Neuropeptide PDF Initiate and Extend Opposing Behavioral States in C. elegans. Cell *154*, 1023–1035.

Fraenkel, G.S., Gunn, Donald Livingston., (1961). The orientation of animals : kineses, taxes and compass reactions (New York: Dover publications).

Franz, M.O., and Mallot, H.A. (2000). Biomimetic robot navigation. Robot. Auton. Syst. *30*, 133–153.

Fujiwara, M., Ishihara, T., and Katsura, I. (1999). A novel WD40 protein, CHE-2, acts cell-autonomously in the formation of C. elegans sensory cilia. Development *126*, 4839–4848.

Fukuto, H.S., Ferkey, D.M., Apicella, A.J., Lans, H., Sharmeen, T., Chen, W., Lefkowitz, R.J., Jansen, G., Schafer, W.R., and Hart, A.C. (2004). G Protein-Coupled Receptor Kinase Function Is Essential for Chemosensation in< i> C. elegans</i>. Neuron *42*, 581–593.

Gerdes, J.M., Davis, E.E., and Katsanis, N. (2009). The Vertebrate Primary Cilium in Development, Homeostasis, and Disease. Cell *137*, 32–45.

Ghosh, K.K., Burns, L.D., Cocker, E.D., Nimmerjahn, A., Ziv, Y., Gamal, A.E., and Schnitzer, M.J. (2011). Miniaturized integration of a fluorescence microscope. Nat. Methods *8*, 871–878.

Goentoro, L., and Kirschner, M.W. (2009). Evidence that Fold-Change, and Not Absolute Level, of β-Catenin Dictates Wnt Signaling. Mol. Cell *36*, 872–884.

Goentoro, L., Shoval, O., Kirschner, M.W., and Alon, U. (2009). The Incoherent Feedforward Loop Can Provide Fold-Change Detection in Gene Regulation. Mol. Cell *36*, 894–899.

Gomez-Marin, A., and Louis, M. (2011). Active sensation during orientation behavior in the Drosophila larva: more sense than luck. Curr. Opin. Neurobiol.

Gray, J.M., Karow, D.S., Lu, H., Chang, A.J., Chang, J.S., Ellis, R.E., Marletta, M.A., and Bargmann, C.I. (2004). Oxygen sensation and social feeding mediated by a C. elegans guanylate cyclase homologue. Nature *430*, 317–322.

Gray, J.M., Hill, J.J., and Bargmann, C.I. (2005). A circuit for navigation in Caenorhabditis elegans. Proc. Natl. Acad. Sci. *102*, 3184.

Hendricks, M., Ha, H., Maffey, N., and Zhang, Y. (2012). Compartmentalized calcium dynamics in a C. elegans interneuron encode head movement. Nature.

Hilliard, M.A., Apicella, A.J., Kerr, R., Suzuki, H., Bazzicalupo, P., and Schafer, W.R. (2004). In vivo imaging of C. elegans ASH neurons: cellular response and adaptation to chemical repellents. EMBO J. *24*, 63–72.

Hilliard, M.A., Apicella, A.J., Kerr, R., Suzuki, H., Bazzicalupo, P., and Schafer, W.R. (2005). In vivo imaging of C. elegans ASH neurons: cellular response and adaptation to chemical repellents. EMBO J. *24*, 63–72.

Iino, Y., and Yoshida, K. (2009). Parallel Use of Two Behavioral Mechanisms for Chemotaxis in Caenorhabditis elegans. J. Neurosci. *29*, 5370.

Jacoby, M., Cox, J.J., Gayral, S., Hampshire, D.J., Ayub, M., Blockmans, M., Pernot, E., Kisseleva, M.V., Compère, P., Schiffmann, S.N., et al. (2009). INPP5E mutations cause primary cilium signaling defects, ciliary instability and ciliopathies in human and mouse. Nat. Genet. *41*, 1027–1031.

Jang, H., Kim, K., Neal, S.J., Macosko, E., Kim, D., Butcher, R.A., Zeiger, D.M., Bargmann, C.I., and Sengupta, P. (2012). Neuromodulatory State and Sex Specify Alternative Behaviors through Antagonistic Synaptic Pathways in C. elegans. Neuron *75*, 585–592.

Joesch, M., Schnell, B., Raghu, S.V., Reiff, D.F., and Borst, A. (2010). ON and OFF pathways in Drosophila motion vision. Nature *468*, 300–304.

Kahn-Kirby, A.H., Dantzker, J.L., Apicella, A.J., Schafer, W.R., Browse, J., Bargmann, C.I., and Watts, J.L. (2004). Specific polyunsaturated fatty acids drive TRPV-dependent sensory signaling in vivo. Cell *119*, 889–900.

Kandel, E.R. (2013). Principles of neural science (New York: McGraw-Hill).

Kato, S., Xu, Y., Cho, C.E., Abbott, L.F., and Bargmann, C.I. (2014). Temporal Responses of C. elegans Chemosensory Neurons Are Preserved in Behavioral Dynamics. Neuron *81*, 616–628.

Klapoetke, N.C., Murata, Y., Kim, S.S., Pulver, S.R., Birdsey-Benson, A., Cho, Y.K., Morimoto, T.K., Chuong, A.S., Carpenter, E.J., Tian, Z., et al. (2014). Independent optical excitation of distinct neural populations. Nat. Methods *11*, 338–346.

Koga, M., and Ohshima, Y. (2004). The C. elegans ceh-36 gene encodes a putative homemodomain transcription factor involved in chemosensory functions of ASE and AWC neurons. J. Mol. Biol. *336*, 579–587.

Komuniecki, R., Hapiak, V., Harris, G., and Bamber, B. (2014). Context-dependent modulation reconfigures interactive sensory-mediated microcircuits in Caenorhabditis elegans. Curr. Opin. Neurobiol. *29*, 17–24.

Koshland, D.E., Goldbeter, A., and Stock, J.B. (1982). Amplification and adaptation in regulatory and sensory systems. Science *217*, 220–225.

Kuhara, A., Inada, H., Katsura, I., and Mori, I. (2002). Negative Regulation and Gain Control of Sensory Neurons by the C. elegans Calcineurin TAX-6. Neuron *33*, 751–763.

Kurahashi, T., and Menini, A. (1997). Mechanism of odorant adaptation in the olfactory receptor cell. Nature *385*, 725–729.

Kwok, T.C.Y., Ricker, N., Fraser, R., Chan, A.W., Burns, A., Stanley, E.F., McCourt, P., Cutler, S.R., and Roy, P.J. (2006). A small-molecule screen in C. elegans yields a new calcium channel antagonist. Nature *441*, 91–95.

Larsch, J., Ventimiglia, D., Bargmann, C.I., and Albrecht, D.R. (2013). High-throughput imaging of neuronal activity in Caenorhabditis elegans. Proc. Natl. Acad. Sci. *110*, E4266–E4273.

Lewis, J.A., Wu, C.H., Levine, J.H., and Berg, H. (1980). Levamisole-resistant mutants of the nematode Caenorhabditis elegans appear to lack pharmacological acetylcholine receptors. Neuroscience *5*, 967–989.

Lockery, S.R., Hulme, S.E., Roberts, W.M., Robinson, K.J., Laromaine, A., Lindsay, T.H., Whitesides, G.M., and Weeks, J.C. (2012). A microfluidic device for whole-animal drug screening using electrophysiological measures in the nematode C. elegans. Lab. Chip *12*, 2211.

Luo, L., Wen, Q., Ren, J., Hendricks, M., Gershow, M., Qin, Y., Greenwood, J., Soucy, E.R., Klein, M., Smith-Parker, H.K., et al. (2014). Dynamic Encoding of Perception, Memory, and Movement in a C. elegans Chemotaxis Circuit. Neuron *82*, 1115–1128.

Ma, W., Trusina, A., El-Samad, H., Lim, W.A., and Tang, C. (2009). Defining Network Topologies that Can Achieve Biochemical Adaptation. Cell *138*, 760–773.

Macosko, E.Z., Pokala, N., Feinberg, E.H., Chalasani, S.H., Butcher, R.A., Clardy, J., and Bargmann, C.I. (2009). A hub-and-spoke circuit drives pheromone attraction and social behaviour in C. elegans. Nature *458*, 1171–1175.

Maimon, G., Straw, A.D., and Dickinson, M.H. (2010). Active flight increases the gain of visual motion processing in Drosophila. Nat. Neurosci. *13*, 393–399.

Marr, D., and Poggio, T. (1976). From Understanding Computation to Understanding Neural Circuitry. Camb. MA Mass. Inst. Technol. Artif. Intell. Lab.

McCormick, K.E., Gaertner, B.E., Sottile, M., Phillips, P.C., and Lockery, S.R. (2011). Microfluidic Devices for Analysis of Spatial Orientation Behaviors in Semi-Restrained Caenorhabditis elegans. PLoS ONE *6*, e25710.

McGrath, P.T., Xu, Y., Ailion, M., Garrison, J.L., Butcher, R.A., and Bargmann, C.I. (2011). Parallel evolution of domesticated Caenorhabditis species targets pheromone receptor genes. Nature *477*, 321–325.

Montell, C. (2012). Drosophila visual transduction. Trends Neurosci. *35*, 356–363.

Mori, I., and Ohshima, Y. (1995). Neural regulation of thermotaxis in Caenorhabditis elegans. Nature *376*, 344–348.

Mukhopadhyay, S., Lu, Y., Shaham, S., and Sengupta, P. (2008). Sensory Signaling-Dependent Remodeling of Olfactory Cilia Architecture in C. elegans. Dev. Cell *14*, 762–774.

Munger, S.D. (2001). Central Role of the CNGA4 Channel Subunit in Ca2+-Calmodulin-Dependent Odor Adaptation. Science *294*, 2172–2175.

Nam, S.-W., Qian, C., Kim, S.H., van Noort, D., Chiam, K.-H., and Park, S. (2013). C. elegans sensing of and entrainment along obstacles require different neurons at different body locations. Sci. Rep. *3*.

Ohno, H., Kato, S., Naito, Y., Kunitomo, H., Tomioka, M., and Iino, Y. (2014). Role of synaptic phosphatidylinositol 3-kinase in a behavioral learning response in C. elegans. Science *345*, 313–317.

Perkins, L.A., Hedgecock, E.M., Thomson, J.N., and Culotti, J.G. (1986). Mutant sensory cilia in the nematode Caenorhabditis elegans. Dev. Biol. *117*, 456–487.

Petrascheck, M., Ye, X., and Buck, L.B. (2007). An antidepressant that extends lifespan in adult Caenorhabditis elegans. Nature *450*, 553–556.

Pierce-Shimomura, J.T., Morse, T.M., and Lockery, S.R. (1999). The fundamental role of pirouettes in Caenorhabditis elegans chemotaxis. J. Neurosci. *19*, 9557.

Piggott, B.J., Liu, J., Feng, Z., Wescott, S.A., and Xu, X.Z.S. (2011). The Neural Circuits and Synaptic Mechanisms Underlying Motor Initiation in C. elegans. Cell *147*, 922–933.

Qin, Y., Zhang, X., and Zhang, Y. (2013). A Neuronal Signaling Pathway of CaMKII and Gq Regulates Experience-Dependent Transcription of tph-1. J. Neurosci. *33*, 925–935.

Reisert, J., and Zhao, H. (2011). Perspectives on: Information and coding in mammalian sensory physiology: Response kinetics of olfactory receptor neurons and the implications in olfactory coding. J. Gen. Physiol. *138*, 303–310.

Richmond, J.E., Davis, W.S., and Jorgensen, E.M. (1999). UNC-13 is required for synaptic vesicle fusion in C. elegans. Nat. Neurosci. *2*, 959–964.

Richter, S.H., Garner, J.P., and Würbel, H. (2009). Environmental standardization: cure or cause of poor reproducibility in animal experiments? Nat. Methods *6*, 257–261.

Rieke, F., and Rudd, M.E. (2009). The Challenges Natural Images Pose for Visual Adaptation. Neuron *64*, 605–616.

Saeki, S., Yamamoto, M., and Iino, Y. (2001). Plasticity of chemotaxis revealed by paired presentation of a chemoattractant and starvation in the nematode Caenorhabditis elegans. J. Exp. Biol. *204*, 1757–1764.

Schöne, H., Strausfeld, Camilla., (1984). Spatial orientation : the spatial control of behavior in animals and man (Princeton, NJ: Princeton university press).

Sengupta, P., Chou, J.H., and Bargmann, C.I. (1996). odr-10 Encodes a Seven Transmembrane Domain Olfactory Receptor Required for Responses to the Odorant Diacetyl. Cell *84*, 875–887.

Shinkai, Y., Yamamoto, Y., Fujiwara, M., Tabata, T., Murayama, T., Hirotsu, T., Ikeda, D.D., Tsunozaki, M., Iino, Y., Bargmann, C.I., et al. (2011). Behavioral Choice between Conflicting Alternatives Is Regulated by a Receptor Guanylyl Cyclase, GCY-28, and a Receptor Tyrosine Kinase, SCD-2, in AIA Interneurons of Caenorhabditis elegans. J. Neurosci. *31*, 3007–3015.

Shoval, O., Goentoro, L., Hart, Y., Mayo, A., Sontag, E., and Alon, U. (2010). Fold-change detection and scalar symmetry of sensory input fields. Proc. Natl. Acad. Sci. *107*, 15995–16000.

Shtonda, B.B., and Avery, L. (2006). Dietary choice behavior in Caenorhabditis elegans. J. Exp. Biol. *209*, 89.

Sourjik, V. (2004). Receptor clustering and signal processing in E. coli chemotaxis. Trends Microbiol. *12*, 569–576.

Suzuki, H., Kerr, R., Bianchi, L., Frøkjær-Jensen, C., Slone, D., Xue, J., Gerstbrein, B., Driscoll, M., and Schafer, W.R. (2003). In Vivo Imaging of C. elegans Mechanosensory Neurons Demonstrates a Specific Role for the MEC-4 Channel in the Process of Gentle Touch Sensation. Neuron *39*, 1005–1017.

Suzuki, H., Thiele, T.R., Faumont, S., Ezcurra, M., Lockery, S.R., and Schafer, W.R. (2008). Functional asymmetry in Caenorhabditis elegans taste neurons and its computational role in chemotaxis. Nature *454*, 114–117.

Taniguchi, G., Uozumi, T., Kiriyama, K., Kamizaki, T., and Hirotsu, T. (2014). Screening of Odor-Receptor Pairs in Caenorhabditis elegans Reveals Different Receptors for High and Low Odor Concentrations. Sci. Signal. *7*, ra39.

Tobin, D.M., Madsen, D.M., Kahn-Kirby, A., Peckol, E.L., Moulder, G., Barstead, R., Maricq, A.V., and Bargmann, C.I. (2002). Combinatorial Expression of TRPV Channel Proteins Defines Their Sensory Functions and Subcellular Localization in< i> C. elegans</i> Neurons. Neuron *35*, 307–318.

Torayama, I., Ishihara, T., and Katsura, I. (2007). Caenorhabditis elegans Integrates the Signals of Butanone and Food to Enhance Chemotaxis to Butanone. J. Neurosci. *27*, 741–750.

Toth, D.J., Toth, J., Gulyas, G., Balla, A., Balla, T., Hunyady, L., and Varnai, P. (2012). Acute depletion of plasma membrane phosphatidylinositol 4,5-bisphosphate impairs specific steps in endocytosis of the G-protein-coupled receptor. J. Cell Sci. *125*, 3013–3013.

Troemel, E.R., Kimmel, B.E., and Bargmann, C.I. (1997). Reprogramming chemotaxis responses: sensory neurons define olfactory preferences in C. elegans. Cell *91*, 161–169.

Tsalik, E.L., and Hobert, O. (2003). Functional mapping of neurons that control locomotory behavior inCaenorhabditis elegans. J. Neurobiol. *56*, 178–197.

Tsunozaki, M., Chalasani, S.H., and Bargmann, C.I. (2008). A Behavioral Switch: cGMP and PKC Signaling in Olfactory Neurons Reverses Odor Preference in C. elegans. Neuron *59*, 959–971.

Varshney, L.R., Chen, B.L., Paniagua, E., Hall, D.H., and Chklovskii, D.B. (2011). Structural properties of the Caenorhabditis elegans neuronal network. PLoS Comput. Biol. *7*, e1001066.

Wahlsten, D., Metten, P., Phillips, T.J., Boehm, S.L., Burkhart-Kasch, S., Dorow, J., Doerksen, S., Downing, C., Fogarty, J., Rodd-Henricks, K., et al. (2003). Different data from different labs: Lessons from studies of gene-environment interaction. J. Neurobiol. *54*, 283–311.

Wallace, H.R. (1968). The dynamics of nematode movement. Annu. Rev. Phytopathol. *6*, 91–114.

Ward, S. (1973). Chemotaxis by the nematode Caenorhabditis elegans: identification of attractants and analysis of the response by use of mutants. Proc. Natl. Acad. Sci. *70*, 817–821.

Ward, A., Liu, J., Feng, Z., and Xu, X.Z.S. (2008). Light-sensitive neurons and channels mediate phototaxis in C. elegans. Nat. Neurosci. *11*, 916–922.

Ward, S., Thomson, N., White, J.G., and Brenner, S. (1975). Electron microscopical reconstruction of the anterior sensory anatomy of the nematode Caenorhabditis elegans.?2UU. J. Comp. Neurol. *160*, 313–337.

Wark, B., Lundstrom, B.N., and Fairhall, A. (2007). Sensory adaptation. Curr. Opin. Neurobiol. *17*, 423–429.

Weber, E.H., , Hering, Ewald,, (1905). Tastsinn und Gemeingefühl, (Leipzig: W. Engelmann).

Weimer, R.M., Richmond, J.E., Davis, W.S., Hadwiger, G., Nonet, M.L., and Jorgensen, E.M. (2003). Defects in synaptic vesicle docking in unc-18 mutants. Nat. Neurosci. *6*, 1023–1030.

Wen, Q., Po, M.D., Hulme, E., Chen, S., Liu, X., Kwok, S.W., Gershow, M., Leifer, A.M., Butler, V., Fang-Yen, C., et al. (2012). Proprioceptive Coupling within Motor Neurons Drives C. elegans Forward Locomotion. Neuron *76*, 750–761.

Wes, P.D., and Bargmann, C.I. (2001). C. elegans odour discrimination requires asymmetric diversity in olfactory neurons. Nature *410*, 698–701.

White, J.G., Southgate, E., Thomson, J.N., and Brenner, S. (1986). The structure of the nervous system of the nematode Caenorhabditis elegans. Philos. Trans. R. Soc. Lond. B. Biol. Sci. *314*, 1–340.

Wicks, S.R., de Vries, C.J., van Luenen, H.G.A.M., and Plasterk, R.H.A. (2000). CHE-3, a Cytosolic Dynein Heavy Chain, Is Required for Sensory Cilia Structure and Function in Caenorhabditis elegans. Dev. Biol. *221*, 295–307.

Wilensky, U. (1999). NetLogo. http://ccl.northwestern.edu/netlogo/. Center for Connected Learning and Computer-Based Modeling, Northwestern University. Evanston, IL.

Wilson, R.I. (2013). Early Olfactory Processing in Drosophila : Mechanisms and Principles. Annu. Rev. Neurosci. *36*, 217–241.

Wilson, M.A., and McNaughton, B.L. (1993). Dynamics of the hippocampal ensemble code for space. Science *261*, 1055–1058.

Yoshida, K., Hirotsu, T., Tagawa, T., Oda, S., Wakabayashi, T., Iino, Y., and Ishihara, T. (2012). Odour concentration-dependent olfactory preference change in C. elegans. Nat. Commun. *3*, 739.

Zhang, Y. (2008). Neuronal mechanisms of Caenorhabditis elegans and pathogenic bacteria interactions. Curr. Opin. Microbiol. *11*, 257–261.

Zheng, M., Cao, P., Yang, J., Xu, X.Z.S., and Feng, Z. (2012). Calcium imaging of multiple neurons in freely behaving C. elegans. J. Neurosci. Methods *206*, 78–82.

Zimmer, M., Gray, J.M., Pokala, N., Chang, A.J., Karow, D.S., Marletta, M.A., Hudson, M.L., Morton, D.B., Chronis, N., and Bargmann, C.I. (2009). Neurons Detect Increases and Decreases in Oxygen Levels Using Distinct Guanylate Cyclases. Neuron *61*, 865–879.